



**HYDROTHERMAL CRYSTAL GROWTH OF LITHIUM TETRABORATE
AND LITHIUM γ -METABORATE**

THESIS

Jeffrey J. Graham, Captain, USAF
AFIT-ENP-14-M-12

**DEPARTMENT OF THE AIR FORCE
AIR UNIVERSITY**

AIR FORCE INSTITUTE OF TECHNOLOGY

Wright-Patterson Air Force Base, Ohio

DISTRIBUTION A: APPROVED FOR PUBLIC RELEASE; DISTRIBUTION IS
UNLIMITED.

The views expressed in this document are those of the author and do not reflect the official policy or position of the United States Air Force, the United States Department of Defense or the United States Government. This material is declared a work of the U.S. Government and is not subject to copyright protection in the United States.

AFIT-ENP-14-M-12

HYDROTHERMAL CRYSTAL GROWTH OF LITHIUM TETRABORATE AND
LITHIUM γ -METABORATE

THESIS

Presented to the Faculty
Department of Engineering Physics
Graduate School of Engineering and Management
Air Force Institute of Technology
Air University
Air Education and Training Command
in Partial Fulfillment of the Requirements for the
Degree of Master of Science

Jeffrey J. Graham, BS
Captain, USAF

27 March 2014

DISTRIBUTION A: APPROVED FOR PUBLIC RELEASE; DISTRIBUTION IS
UNLIMITED.

AFIT-ENP-14-M-12

HYDROTHERMAL CRYSTAL GROWTH OF LITHIUM TETRABORATE AND
LITHIUM γ -METABORATE

Jeffrey J. Graham, BS
Captain, USAF

Approved:

//signed//

7 March 2014

Capt Timothy W. C. Zens, PhD
(Chairman)

Date

//signed//

28 February 2014

J. Matthew Mann, PhD (Member)

Date

//signed//

28 February 2014

James C. Petrosky, PhD (Member)

Date

Abstract

This work attempted to grow lithium tetraborate ($\text{Li}_2\text{B}_4\text{O}_7$) crystals using the hydrothermal growth technique. If sufficient mastery over lithium tetraborate growth can be achieved, the crystals hold promise for use as solid-state neutron detectors.

The initial experiment, a spontaneous nucleation reaction, utilized dissolution and precipitation region temperatures of 565°C and 490°C , respectively, for ten days, with 10^{-6} M LiOH as the mineralizer solution. This successfully transformed 4.03 g of fine $\text{Li}_2\text{B}_4\text{O}_7$ powder into small (1-3mm) lithium tetraborate crystals, as validated using Single Crystal X-Ray Diffraction (SXRD). Transport growth was conducted with Czochralski-grown $\text{Li}_2\text{B}_4\text{O}_7$ as a seed crystal and attempted a transport growth reaction with dissolution and precipitation zones at 535°C and 495°C , held for eight days, and in 10^{-6} M LiOH. All of the $\text{Li}_2\text{B}_4\text{O}_7$, including the seed crystal, dissolved and produced two $\gamma\text{-LiBO}_2$ crystals, spontaneously nucleated, toward the middle of the tube. Solved crystal parameters were $a = b = 4.1961\text{\AA}$, $c = 6.5112\text{\AA}$, in the tetragonal space group $I\bar{4}2d$. They were of good local optical clarity. Both had major dimensions on the order of 10 mm.

A phase study was conducted, in which $\text{Li}_2\text{B}_4\text{O}_7$ powder and LiOH mineralizer were left to reach thermodynamic equilibrium over the course of three days, with a 25°C gradient to allow the material to dissolve and reform. It was discovered that $\gamma\text{-LiBO}_2$ is the stable phase of the boron-lithium-oxygen system at temperatures between 350°C and 550°C , and furthermore that it is necessary to quench the reaction, lest the material re-dissolve and precipitate as a hydrated phase, $\text{Li}_3\text{B}_5\text{O}_8(\text{OH})_2$.

Solubility experiments performed on a Czochralski-grown tetraborate crystal, and conducted at 450°C and 500°C, showed that the $\text{Li}_2\text{B}_4\text{O}_7$ was converting spontaneously to $\gamma\text{-LiBO}_2$ without the presence of a temperature gradient. In a 24 hour period at 450°C, 15% of the $\text{Li}_2\text{B}_4\text{O}_7$ dissolved; this compares to about 2% for $\gamma\text{-LiBO}_2$ under similar conditions. Subsequent experiments showed that $\text{Li}_2\text{B}_4\text{O}_7$ formed under kinetic growth conditions, whilst $\gamma\text{-LiBO}_2$ was to be found under thermodynamic conditions. This work indicates that high-quality $\text{Li}_2\text{B}_4\text{O}_7$ is not suitable for hydrothermal growth.

A transport $\gamma\text{-LiBO}_2$ growth reaction using one of the spontaneously nucleated $\gamma\text{-LiBO}_2$ crystals from the first attempted transport reaction, and crystalline feedstock. Unfortunately, the feedstock did not dissolve as rapidly as expected, and the seed crystal dissolved. The only products were crystals smaller than those of the original feedstock. Consideration of the possible differences between the cases pointed to the feedstock as the key difference. The structures of $\text{Li}_2\text{B}_4\text{O}_7$ and $\gamma\text{-LiBO}_2$ support the theory that the tetraborate dissolves much more quickly than the metaborate, so that in the reactions with the $\text{Li}_2\text{B}_4\text{O}_7$ feedstock the solution was brought to supersaturation much more quickly. The author speculates that $\gamma\text{-LiBO}_2$ could be created effectively by the incorporation of $\text{Li}_2\text{B}_4\text{O}_7$ into the $\gamma\text{-LiBO}_2$ feedstock, in order to provide an early saturation to protect the seed crystal, but further experimental confirmation is still sought.

AFIT-ENP-14-M-12

For my parents.

Acknowledgements

Foremost, I'd like to thank Dr. J. Matthew Mann, for his saintly patience and support as I worked in his laboratory. He also solved the crystal structures, when necessary, and helped make the crystal structure diagrams in the results section of the work. He is followed shortly by Major Timothy Zens, my research advisor. Dr. John McClory deserves mention for obtaining the Czochralski-grown lithium tetraborate samples so helpful to this work. Dr. James Petrosky deserves credit for establishing the initial relationship with AFRL that allowed this work to come to fruition, and for providing necessary motivation to the over-all process.

Jeffrey J. Graham

Table of Contents

	Page
Abstract	iv
Acknowledgements	vii
List of Figures	x
1. Introduction	1
1.1 Motivation	1
1.2 Research Problem	5
1.3 Research Scope	8
1.4 Thesis Summary	9
2. Theory	10
2.1 Crystallography	10
2.1.1 The Origin of Symmetry	12
2.1.2 Crystal Structures and Band-Gaps	24
2.2 The Hydrothermal Growth Technique	37
2.3 Prior Work	42
3. Experimental Technique	49
3.1 Growth Apparatus	49
3.2 Hydrothermal Growth Experiments	52
3.2.1 Phase Studies	52
3.2.2 Spontaneous Nucleation	53
3.2.3 Solubility Studies	54
3.2.4 Transport Growth	54
3.3 Characterization	55
4. Results and Analysis	57
4.1 Spontaneous Nucleation	57
4.2 The First Transport Growth Experiment	58
4.3 Second Spontaneous Nucleation	61
4.4 A Proposed Explanation	62
4.5 Phase Study Results	63
4.6 Solubility Study Results	65
4.7 Kinetic Growth	67
4.8 Lithium Metaborate Growth	68

	Page
5. Conclusions	77
5.1 Future Work	78
6. Appendix A	84
6.1 The Problem	84
6.2 Computational Approximation	88
6.3 Initial Technical Approach	94
6.4 An Attempt at Refinement	95
Bibliography	102

List of Figures

Figure		Page
1.	Various neutron reaction cross-sections for nuclei of interest.	4
2.	Possible choices of unit cell for a given lattice.	11
3.	C_3 axes in a tetrahedron.	13
4.	An illustrative snowflake.	15
5.	A schematic of Euler's angle construction.	16
6.	The Fourteen Bravais Lattices.	19
7.	X-ray reflection in a lattice.	21
8.	A periodic potential simplification for a lattice.	25
9.	Directions in a crystal associated to periodic potentials.	25
10.	An illustrated solution to the Kronig-Penney model.	27
11.	Band-filling schematic.	29
12.	Dopants within the bandgap	31
13.	Electrons excited as a function of temperature	31
14.	The NaCl lattice	33
15.	The Diamond lattice	33
16.	Hydrothermal Growth Apparatus: a notional depiction	38
17.	A section view of a Tuttle cold-cone seal.	50
18.	The Bridgman Seal in Cross-Section.	51
19.	Spontaneously nucleated $\text{Li}_2\text{B}_4\text{O}_7$ crystals.	58
20.	Crystals spontaneously nucleated during transport growth	59
21.	A figure indicating potential nucleation zones.	60

Figure		Page
22.	A graph comparing the solubilities of $\text{Li}_2\text{B}_4\text{O}_7$ and $\gamma\text{-LiBO}_2$	65
23.	$\text{Li}_2\text{B}_4\text{O}_7$ after a 24 hr dissolution	67
24.	Rates of dissolution of lithium-borate glasses in 30°C water	70
25.	a-axis view of $\text{Li}_2\text{B}_4\text{O}_7$	71
26.	A view down the a-axis of $\gamma\text{-LiBO}_2$	72
27.	A view down the c-axis of $\gamma\text{-LiBO}_2$	72
28.	Arrangement of tetrahedral and trigonal planar coordinated boron in $\text{Li}_2\text{B}_4\text{O}_7$	73
29.	Arrangement of tetrahedrally coordinated boron in LiBO_2	73
30.	Comparison of sizes between phosphate dopant and proposed substitutional site	79
31.	A cartoon depicting the straining of the metaborate lattice as a result of phosphate incorporation	81
32.	A two-dimensional depiction of the boron-oxygen network in lithium tetraborate.	81
33.	A two-dimensional depiction of the boron-oxygen network in lithium tetraborate, strained by PO_4	82
34.	Initial autoclave temperature profile	86
35.	One hour elapsed autoclave temperature profile	87
36.	A very simple physical model.	92
37.	A convergence plot for the simple model	93
38.	Geometry used in the COMSOL modeling	96

HYDROTHERMAL CRYSTAL GROWTH OF LITHIUM TETRABORATE AND LITHIUM γ -METABORATE

1. Introduction

1.1 Motivation

Efficient and reliable neutron detection provides a number of valuable capabilities for basic science and practical application. Foremost, neutron emissions are a diagnostic signature for the presence of Special Nuclear Material (SNM). Tracking, and particularly detecting surreptitious supplies of, SNM is obviously of great interest to national—indeed global security. Such technology also has applications beyond national defense: efficient neutron detection has potential for use in laboratory settings—neutron imaging, neutron tomography, emission characterization, and so forth. Furthermore, the more efficient a neutron detector becomes, the smaller the flux of neutrons required to achieve a given effect, in the same way that 800 speed film needs less light to take a clear photograph than 400 [1]. Common knowledge—and As Low As Reasonably Achievable dose practice— indicates that reducing the neutron flux involved in a given process will have substantial benefits for safety, power requirements, and portability.

Detecting neutrons is unfortunately quite difficult. As neutral particles, they are restricted to interactions with the atomic nucleus, which occupies significantly less volume than an entire atom. Indeed, to order of magnitude, a nucleus has 10^{-10} the cross-sectional area of an atom, or about 10^{-1} barns. This can be compensated for, somewhat, by the use of nuclei with very large neutron capture cross-sections for

thermal neutrons, in particular ^{10}B at 3.5×10^3 barns, ^6Li at 9.4×10^2 barns, and ^3He at 5.6×10^3 barns [2].

Once a nucleus captures a neutron, the resulting agglomeration will likely have excess energy it wants to shed, as a γ -ray, a β -particle, an Auger electron, a heavy charged particle (proton, triton, α), or, in rare cases, fission fragments. These reaction products, as ionizing radiation, are much easier to detect than neutrons, and are known as secondary radiation. The challenge is for the secondary radiation travel without significant attenuation to a suitable detector, which is known as the secondary detector.

It is not impossible that the primary and secondary detector be one and the same; BF_3 gas, for instance, can serve both as the neutron reaction chemical and working medium for some types of gaseous detectors [1]. This is not necessarily ideal, however. For any radiation detection, the macroscopic cross-section Σ of the detector material is a key performance parameter, calculated as

$$\Sigma = \sigma\rho, \tag{1}$$

where σ is the microscopic cross-section ($\propto [\text{length}]^2$) and ρ the number density of nuclei. It follows that the more numerically dense a detector material can be made, for a given stoichiometry and enrichment, the more likely it is to detect neutrons. Thus gaseous detectors, such as the BF_3 gas tube noted above, are not optimal from a reaction density standpoint.

It is also worth remarking that current neutron detection capabilities often suffer from certain practical difficulties. BF_3 and ^3He gas detectors are restricted in size by electric characteristics, must be kept sealed, require pure gasses, and must also be driven at several hundred volt potentials [1]. Nor is it particularly desirable to use BF_3 , if it can be avoided: it is corrosive to flesh and very poisonous by

inhalation; the US DoT forbids it on air transport; handling of the compressed gas cylinders must be done with great care; the gas supply should neither be heated nor allowed to chill below 29°C. In sum, a dangerous and logistically difficult substance to have to use [3,4]. ^3He is much safer, but is tremendously expensive—upwards of \$2000/liter in 2010 and rising [5], particularly because the global supply of ^3He is waning [6]. Furthermore, though its cross-section is superior to that of either ^6Li or ^{10}B , the latter two have greater scope of chemistry with which to form solids and liquids—that is to say, they have some. Helium’s extreme inertness restricts it to use as a much lower density gas, impacting the macroscopic cross-section. Some correspondents ([7]) have observed that the ^3He and BF_3 detectors have an advantage in being conceptually similar in the data analysis; the author grants this, but asserts that this is completely overshadowed by their logistical costs. As for pure lithium, its chemistry generally restricts it to use in scintillator crystals and liquids [1]. Both of these technologies require photo-multiplier tubes driven at kilovolt potentials. Such difficulties are, of course, surmountable, but inconvenient. This work intends to take a step in bypassing these difficulties altogether.

The radiation detected also presents difficulties from a discrimination standpoint. The most energetic reaction products are heavy charged particles—alpha particles, tritium nuclei, and protons. Each reaction releases energy according to the original nucleus; ^6Li is the most energetic of these neutron capture reactions, liberating 4.78 MeV in the form of ^4He and ^3H kinetic energy [1], but even this could be swamped by the absorption of a sufficient number of gamma-rays. ^{60}Co , for example, produces two gammas (1.1732 MeV and 1.3325 MeV) [8], ergo four of these arriving within one integration time could easily be confused for a neutron peak [9,10]. Naturally, this is progressively more likely to occur as the gamma intensity increases, but a practical detection model—particularly a model

focused on surveillance—cannot assume the absence of a powerful gamma ray source, particularly if neutron producing reactions are involved, or if an adversary has sought to incorporate materials to mask the target signature. Therefore, the larger the signal produced by a neutron interaction, and the less produced by gamma rays, the more effectively the detector can discriminate.

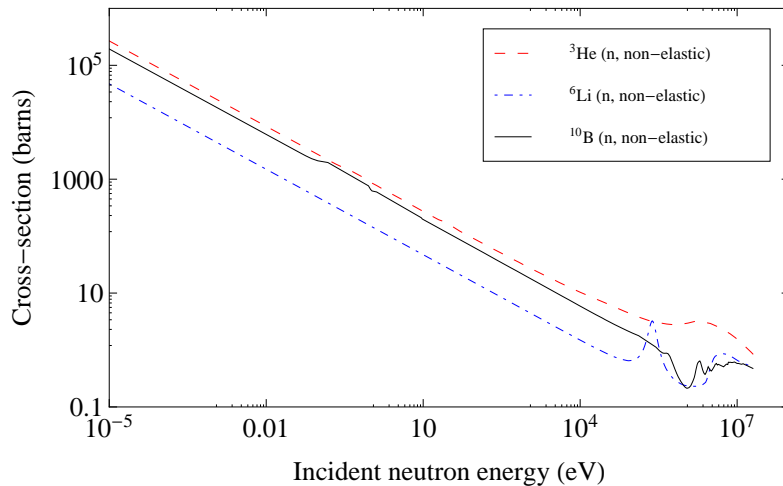


Figure 1. Various neutron reaction cross-sections for isotopes commonly used in detector apparatus [2]. ^3He has a strong advantage in terms of its microscopic cross-section at thermal energies, but is difficult to compress and of limited availability; the lithium and boron are much cheaper, and have vastly more chemistry with which to form solids and liquids.

Lithium tetraborate ($\text{Li}_2\text{B}_4\text{O}_7$) holds promise as a nuclear detection material. Though it is still reliant on the nuclear reactions of boron and lithium discussed above, its solid form brings advantages not seen in gaseous or liquid detectors. These include a greatly increased density of target nuclei; ease of handling and storage; and potential advantages for signal emission. As regards this last point, there are indications that $\text{Li}_2\text{B}_4\text{O}_7$ may be suitable for neutron detection both as a thermoluminescent substance, passively recording neutron interactions as thermally-released potentials within its structure [11–16], and as an active agent, in which nuclear reactions change the electronic properties of the material and allow

for immediate neutron detection [17]. Insofar as it is comprised of low-Z elements, it should be relatively gamma-insensitive [18]. However, to thoroughly exploit both of these potentials—and especially the second—it will be necessary to have abundant, relatively inexpensive semiconductor-quality $\text{Li}_2\text{B}_4\text{O}_7$ crystals.

1.2 Research Problem

Large scale growth of $\text{Li}_2\text{B}_4\text{O}_7$ has occurred by the Czochralski [19–21] and Bridgman [22, 23] methods. Unfortunately, these are not always optimal for growing lithium borates. Various species have shown to melt incongruently, and therefore unsuited to melt techniques [24], while flux growth methods can lead to undesirable inclusions as the flux cools and precipitates [25]. Borate melts may also have high viscosity, thereby forming glasses [24], which is detrimental to applications requiring long-range order. A further concern, particularly relevant to thermoluminescence and conductivity, is the incorporation of dopants within the system. Unfortunately, at least in the case of Bridgman growth, attempts to dope the crystal in bulk resulted in inhomogeneous dopant concentrations [26]. This is because the viscosity of the borate melts noted above acts as a barrier to homogeneous mixing of dopants into the melt for both Czochralski and other techniques reliant upon diffusion to achieve homogeneity. Finally, Brant and Swinney both note that [13, 27] the Czochralski method tends to form lithium and oxygen vacancies in the $\text{Li}_2\text{B}_4\text{O}_7$ lattice, though both are silent on the underlying cause. Lithium vacancies are naturally contradictory to the goal of forming an efficient neutron detector, as they represent a decrease in the number of possible neutron interactions. Furthermore, vacancies in general are not desirable if one is to create a single-stage semiconductor neutron detector, as they impede current flow and therefore reduce both the measurable signal and resolution [7, 28, 29].

Hydrothermal growth offers a promising method of overcoming the difficulties presented by other growth techniques, while providing high-quality crystals. The technique has been shown, in some cases, to avoid incongruent melting by dissolving the feedstock in an aqueous mineralizer solution. This enables it to grow large crystals not otherwise accessible, though it is by no means a panacea. Moreover, the technique does not require the high temperatures involved in melt processes, so that thermal strain and defect formation is reduced [29–31]. Additional advantages could arise if dopants can be adequately dissolved and subsequently incorporated into the lattice. Their complete mixing within the solution should give rise to a uniform distribution within the crystal, and consequently create a uniformly doped crystal [32]. This is in contrast to the flux and melt growth methods, in which lithium borates demonstrate high viscosities [24]. This increased resistance to fluid motion decreases turbulent mixing, as could be predicted heuristically by taking the derivative of the Reynold’s number with respect to viscosity, and likewise decreases atomic diffusion, in accordance with the Stokes-Einstein equation [33].

It is also worth observing that the hydrothermal technique can also purify the feedstock, isolating impurities from the feedstock in the solution. The astute reader may observe that purification is the reverse of the doping process lauded in the preceding paragraph; what actually occurs is dependent upon the specific reaction conditions, both thermal and chemical. Purification is more likely with small temperature differentials, in a thermodynamic growth regime—that is to say, the regime where the change in surface energy as the crystal grows dominates over the motion of the dissolved particles [34]. By definition, the crystal structure has no energetically favorable location for impurities, and these foreign materials are more stable in the surrounding plenum [28]. Therefore, if an impurity does crystalize on to the surface, it is very likely to redissolve before the bulk crystal can precipitate

around and trap it. By contrast, if the reaction conditions are tilted toward the kinetic side—for instance by increasing the temperature gradient—then an impurity molecule may be surrounded by stable crystal before it can escape. Likewise, the purity of the mineralizer solution is of tremendous importance; starting with a greater purity than that of the original crystal should prevent the formation of a solution saturated in impurities, preventing their precipitation, and contrariwise saturating the mineralizer with a dopant material will make it more likely to precipitate out. In either case, given a thermodynamic growth process, impurities can be expelled. And, insofar as the inclusion of impurities are energetically costly, the lower temperatures of the hydrothermal growth process will prove advantageous in this regard, just as it was for the formation of other defects. Though it is still axiomatic that the greater the purity of the starting material, the greater the purity of the finishing material, such an advantage cannot be ignored when endeavoring to create crystals sufficiently electronically perfect to serve in a single-stage detector.

Some progress has already been made toward the hydrothermal growth of lithium borate crystals. Byrappa made a limited exploration of hydrothermal $\text{Li}_2\text{B}_4\text{O}_7$ growth, with some success under subcritical conditions in dilute formic acid. Unfortunately, his product size was limited by the internal volume of his apparatus, and bulk growth was not demonstrated [35]. More recently, McMillen demonstrated the viability of growing $\gamma\text{-LiBO}_2$ hydrothermally, and evinced solubility and growth rates at and above the supercritical point of water that approached those of quartz [36]. This is extremely important from a practical, economic standpoint. Consider that a bulk growth autoclave is a considerable expense, and to be an economical proposition must produce a volume of crystal at least worth the cost of its acquisition and operation, plus a modest profit. The faster a profitable crystal can be grown, all other factors (heating energy expenses,

facilities maintenance, wages, management overhead, etc.) the smaller the operating cost per run, and the faster that the autoclave can pay itself off. It follows directly that the faster a high-quality crystal may be grown, the more likely it is to transition from the laboratory to industry.

1.3 Research Scope

A great deal of work remains to be done before $\text{Li}_2\text{B}_4\text{O}_7$ can be made into a practical neutron detector, including: establishing growth parameters, growing sufficiently pure crystals, successfully and repeatedly doping the crystals, performing neutron characterization, the creation of suitable electrical contacts, and the electrical characterization of the crystals. This is enough work to keep a great many researchers occupied for years. Therefore, in order to appropriately demarcate the bounds of inquiry, this work is specifically focused upon optimizing the growth of lithium metaborate crystals in hydrothermal solution. The following aspects are planned:

- Spontaneous nucleation: create viable crystalline feedstock and solubility study samples.
- A phase study: identify what species are thermodynamically favored in the chosen mineralizer solution.
- Solubility studies: determine the degree to which $\text{Li}_2\text{B}_4\text{O}_7$ saturates the mineralizer solution as a function of temperature.
- Transport growth: demonstrate the practicality of growing $\text{Li}_2\text{B}_4\text{O}_7$ by the hydrothermal method, and get preliminary measurements of the crystalline growth rate.

1.4 Thesis Summary

The remaining chapters of this work address topics as outlined below:

- **Theory** provides pedagogy in crystallography, crystallographic terminology, X-ray diffraction theory, solid-state physics, thermodynamics, and hydrothermal crystal growth as each applies to the work at hand. A section on the prior work in the field and the state-of-the-art is also provided.
- **Experimental Technique** covers the methods used in the research in a manner appropriate to the reader who desires to replicate the work in question, or who is unfamiliar with the particular operations.
- **Results and Analysis** contains the specific experimental data collected for this work and the reasoning about the implications.
- **Conclusions** contains a summary of the most salient inferences supported in the Results and Analysis section.

2. Theory

This is a pedagogical chapter. The section on crystallography addresses the basics of crystals and the emergence of some of their properties that make them valuable materials. It can be skipped by experienced crystallographers or solid-state physicists. The second section addresses hydrothermal growth, its principle of operation, advantages, and disadvantages. The final section covers prior work in the field and is intended to bring the reader to a general knowledge of the state of the field at the time of writing.

2.1 Crystallography

Having asserted the goal of growing lithium tetraborate crystals, it is germane to address what is meant by a crystal in a very precise sense, and to explore how the exactitude of their nature gives rise to a number of very useful properties not found in other states of matter.

Crystals are any arrangement of atoms, known as a basis, that repeat themselves in three dimensions. This basis may be as simple as a single atom, or it may be constructed of substantial molecules. The description of position of each instance of the basis throughout three-space is known as the lattice. Furthermore, all crystals are translationally invariant—which is to say, If one were to start at any point within a perfect crystal and travel in any straight line, one would periodically come to a point indistinguishable from the starting point. This countably infinite collection of loci within the crystal comprise a set of lattice points—each of which being only one of uncountably infinitely many possible sets to choose from. Furthermore, by performing the walk in three different directions—ideally chosen according to criteria discussed later in the work—it is possible to designate a

volume that repeats itself throughout the crystal. This volume makes a unit cell.

The simplest (primitive) unit cell provides the basic reference frame for describing a theoretical perfect crystal. After defining the positions and relations of atoms within one unit cell, those relations will repeat without variation, making the description of one unit cell sufficient to define the entire bulk of the crystal. An astute observer will further note that, as space is continuous and the crystal under consideration of infinite extent, there must be an infinite choice of points at which to begin, and likewise directions in which to walk; there is some call for a judicious choice of unit cell if crystallography is to make sense of its material. An example of this may be found, for two dimensions, in Figure 2. The blue circles are lattice

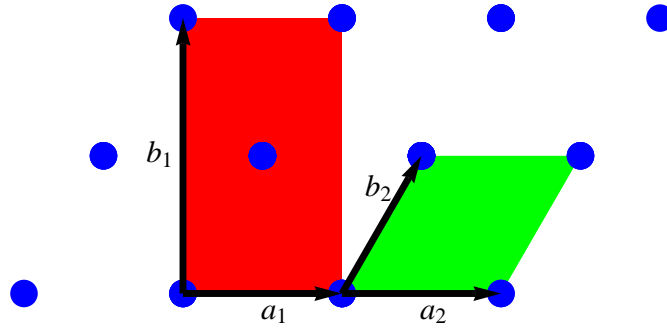


Figure 2. The circles are individual lattice points within the crystal. They could be atomic nuclei, the center of mass of some complex—those details are immaterial. Both the rectangle and lozenge form potential cross-sections for a unit cell, in that they will generate the same lattice by infinite repetition. That said, the lozenge is superior as it represents the symmetry of the system.

points; the rectangle and parallelogram are possible unit cells based on the choice of direction one might walk. Both will, if repeated, generate the same lattice, but some choice must be made to use one or the other. On the one hand, the rectangle has orthogonal basis vectors in this plane, which would make some calculations more efficient, but at the cost of imposing new ones for the lattice point at its center. Moreover, the lattice clearly has a rotational symmetry—a six-fold rotation about the axis perpendicular to the plane, passing through the center of any of the lattice

points—and the rectangle does not. The parallelogram’s case is better: though the lack of orthogonal basis vectors a_1 and b_1 makes other aspects of the mathematics more tedious, in practice the advantages of basis vectors a_2 and b_2 already matched to lattice points provide the greatest utility [37]. More importantly, the parallelogram can be matched with two more parallelograms create a space-filling hexagonal tessellation which does capture the rotational symmetry, and is on that account alone preferable to the rectangle.

But if the second choice of vectors is preferable to the first for reasons of symmetry, then the best basis vectors would be those which maximize symmetry. Furthermore, it is in fact the case that crystals can be classified based on their symmetries—and for this reason, the subject deserves a fuller treatment.

2.1.1 The Origin of Symmetry

Symmetry itself is defined by the existence of an operation which leaves the final state of a system invariant. The greater the number of operations which perform in this fashion, the more symmetric the system is. For example, given a gear with twelve identical teeth, a rotation of $\frac{2\pi n}{12}$, $n \in \mathbb{Z}$ cannot be deduced from observing only the starting and finishing states. Moreover, a gear with 36 teeth will be indistinguishable for any rotation $\frac{2\pi n}{36}$, $n \in \mathbb{Z}$, and is clearly more symmetric than the twelve-tooth gear. Considering that a crystal is an object defined by an eternal recurrence, symmetry is the primary method of classifying various crystal systems. By doing so, material properties that depend on orientation and periodicity are the same in symmetric directions, as one would expect, and the complexity of describing a system is reduced by the natural repetition [37, 38].

To begin, there are a finite number of symmetry operators appropriate to crystallography [37]:

1. Identity: the “do nothing” operator, this simply leaves the system as it came. Its inclusion is for mathematical completeness rather than its own interesting properties. It is denoted E .
2. Rotation: there exists an axis about which an object might be rotated by some angle $\frac{2\pi}{n}$, denoted either by n (Hermann-Maguin notation) or C_n (Schoenflies notation). Note that an object may have several different rotation axes at various orientations; Figure 3 shows various C_3 axes within a tetrahedron.

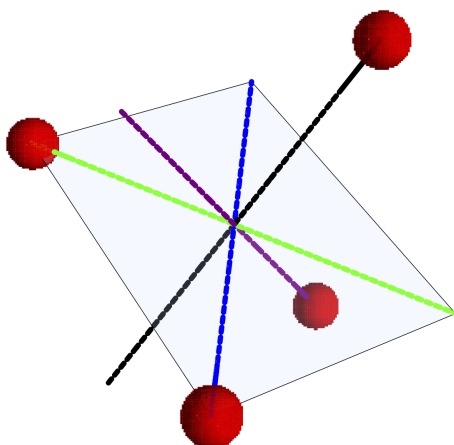


Figure 3. The dashed lines depict various, though not all, C_3 axes found within a tetrahedron. The square shows one of the mirror planes within the tetrahedron, parallel to the blue axis.

3. Mirror planes: these planes bisect space such that for every point on the plane, the same matter will be found at the same displacement. An example may be seen in Figure 3 as the plane cutting through two of the spheres. Note that a single mirror plane does not necessarily imply the existence of other symmetry elements.

4. Center of symmetry: this operation could be described as every point moving along a line defined by its initial position A and the origin O , to a final position B such that $\overline{AO} \cong \overline{OB}$.
5. Improper rotation: this is a combination of rotation with another transform. In the Schoenflies system, a $\frac{2\pi}{n}$ rotation is matched with a mirror plane perpendicular to the axis of rotation, and is denoted S_n . In the Hermann-Maguin system, the rotation is matched with an inversion symmetry, and denoted \bar{n} . Fundamentally, both systems cover the same physical situations, and are equivalent; their choice of n , however, usually differs. It is also important to remember that the presence of an improper rotation, though comprised of a rotation axis and another operation, does not imply that any of those operations belong to the system on their own. The improper rotation is its own operation, and not decomposable.

Any single entity with symmetry has a point group associated with it—which is a good pedagogical starting point from which to develop the use of the operators listed above. One such entity is the snowflake, shown in Figure 4. It clearly has a six-fold axis C_6 of rotation at its center, perpendicular to the the page. Assuming that, were the snowflake flipped over, it would be the same, there is also a mirror plane perpendicular to C_6 , increasing the number of symmetries. These two in combination lead to the suspicion of a number of rotation axes in the plane of the snowflake, e.g. a C_2 axis running from the top of the page to the bottom, in the plane of the paper would flip it over and reveal the same image. By inspection, there are six such C_2 axes. [37] observes that these conditions are all met by D_{6h} . Alternatively, in Hermann-Maguin notation, one notes the presence of the primary axis and that there are two 2-fold axes perpendicular. (The reason for including a third axis will become apparent later.) Furthermore, each one of these has a mirror

plane perpendicular to it, by inspection, so one should write out $\frac{6}{m} \frac{2}{m} \frac{2}{m}$ for its group (or 6/mmm, in shorthand). In either notation, the symmetries are the same.



Figure 4. The snowflake is a classic example of D_{6h} point group symmetry in nature. That is to say, it has can be rotated about an axis perpendicular to the page and at its center $\frac{1}{6}$ of the way around and return to an identical position; assuming that the reverse of the image is the same as the obverse, there are six C_2 axes within the plane of the page, and of course the mirror symmetry half-way through the snow flake. No matter the operation, however, the very center of the snowflake remains cold and unmoved. (The image is from Wikimedia Commons, <http://commons.wikimedia.org/wiki/File:Snowflake3.png>, and was taken by Wilson Bentley (1865-1931); it is in the public domain.)

The astute reader will notice immediately that, for instance, a Frisbee has an infinite number of rotational symmetries (C_∞), and that this surfeit of possibility does not seem to apply to crystals. And indeed, only certain instances of these operators are allowable, owing to the requirements of the crystalline lattice. For example, in the case of rotations, only 1-, 2-, 3, 4-, and 6- fold rotations are permissible. Proof: given an n -fold rotation axis at some point x_0 within a crystal, there must be another, identical rotation axis at some position \vec{d} away, called x_1 . Let there be two points between the two axes, denoted p_0 and p_1 , each located a distance a from its respective axis, with the restriction that $d = ma$, $m \in \mathbb{Z}$. Because of the rotational symmetry imposed by each n axis, there will be two points

p'_0 and p'_1 located such that their displacement from p_0 and p_1 , respectively, parallel to \vec{d} is $a \cos(2\pi/n)$. These, points, too, must be separated by la , $l \in \mathbb{Z}$, otherwise two parallel directions in the crystal would be of different periodicities, and violate the fundamental assumption of crystalline regularity. Therefore it follows that

$$la = ma - 2a \cos \frac{2\pi}{n} \quad (2)$$

$$\frac{2\pi}{n} = \frac{m-l}{2} \quad (m, l, n \in \mathbb{Z}), \quad (3)$$

which only has solutions for $n = 1, 2, 3, 4$, and 6 [37]. A similar sort of argument restricts the number of possible mirror combinations appropriate to plane lattices, with commensurate restrictions on the shape of the mesh describing the lattice. As it happens, there are only five, and they match up to specific sets of rotational symmetry within the plane as well [38].

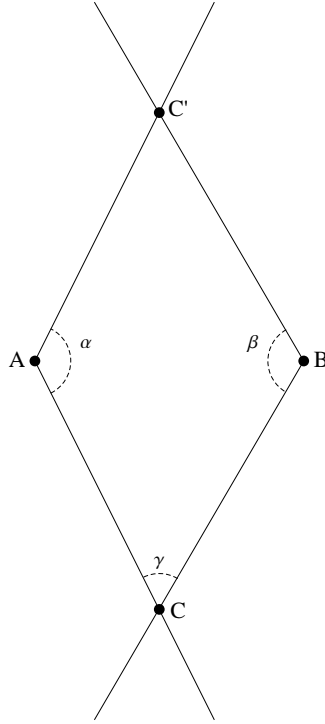


Figure 5. A and B are rotation axes that move a third point, C, to its primed position and back, yielding a motion that is equivalent to a single rotation about C.

After noting some of the restrictions on how operators may be placed in a plane, it should not be terribly surprising that there are restrictions on how they may be combined. Rotation operators provide an excellent example of this, with a construction due to Euler [38]: consider a sphere with two independent rotation axes running from the center, O , to points A and B on the surface, as depicted in projection in Figure 5. Each axis rotates the sphere about itself by an angle α or β , in the right-handed convention of positive rotations. By construction, it follows that the surface at point C is displaced to C' by A and returned to its original position by B . It follows that the displacement of any other points on the surface are equivalent to a rotation about C in the negative direction. (Remember, this is representative of convex geometry and $\alpha/2 + \beta/2 + \gamma \neq \pi$!) As these axes are entirely arbitrary, it follows that any two axes imply a third, which satisfy the relationship

$$A_\alpha B_\beta C_{-\gamma} = E. \quad (4)$$

It now becomes entirely to the point to outline the derivation of all the crystallographic space groups. Between the requirements of equations (3) and (4), it is immediately apparent that there are at most 5^3 possible combinations of rotation axes appropriate to crystallography. However, there's nothing particularly unique separating, e.g., 322, 232, or 223 from one another. Furthermore, considering (4) in greater depth, it follows that not all combinations of rotations are mathematically sound. In the end, there are only 32 crystallographic crystal classes borne of rotations [38].

Each group also gives rise to a particular class of geometry in space. For example, symmetry group 4, which has one C_4 axis and no other symmetries, speaks to a geometry from the tetragonal class, which is a parallelepiped with two dimensions equal and all angles right. Thus, all 32 of the crystal classes can be

classified amongst seven different shapes of unit cell, or seven types of primitive cell.¹ There are also some variations upon this theme—face, body, and base centering—which yield the 14 Bravais lattices [37,38]. These are the only ways in which point groups can be arranged in space, and so are the fundamental unit cells for crystallography. A complete listing, with their geometric requirements, may be found in Figure 6.

A crystal is much larger than a single point group, however. Point group symmetry operations are fundamentally local; they cannot generate system of greater dimensions than those with which they started. It has been observed, however, that a crystal can be modeled as a lattice of infinite extent, and that this approximation is actually quite good on the atomic scale, far from the surface. Two further operations become permissible: screw dislocations and glide planes. Both are compound motions, much like the improper rotation of the point groups, and their properties are as follows [37]:

1. Glide plane: in this operation the points are reflected across a plane and then moved along that plane for half of the unit cell’s magnitude in that direction. That is to say, if the glide plane is parallel to the a dimension of the lattice, then the glide plane will translate $a/2$.
2. Screw axis: a rotation, similar to a C_n axis, followed by a motion parallel to said axis for a distance p/n , where $p \leq n$ and $p \in \mathbb{N}$. Units are given in the characteristic dimension to which the axis is parallel.

Given these two, additional options, each space group and Bravais lattice pairing can be combined with these operations. The full derivation of all of these groups, however, is a much longer procedure than is warranted in this text, and the reader is referred to Buerger’s *Elementary Crystallography* [38] for a very thorough and

¹Some authors combine the trigonal and hexagonal groups, and some do not.

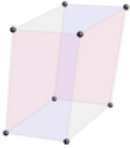
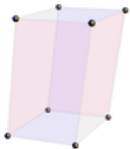
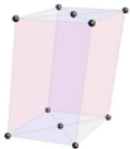
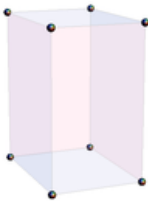
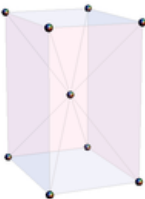
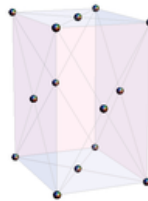
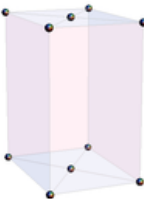
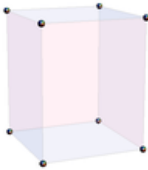
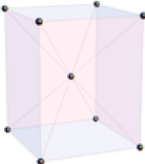
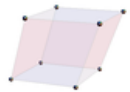
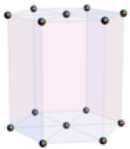
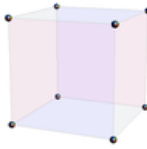
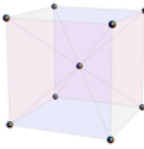
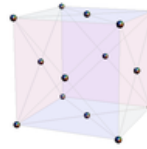
Crystal System	Requirements	Primitive	Body Centered	Face Centered	Base Centered
Triclinic	$\alpha \neq \beta \neq \gamma$ $a \neq b \neq c$				
Monoclinic	$\alpha = \gamma = 90^\circ$ $a \neq b \neq c$				
Orthorhombic	$\alpha = \beta = \gamma = 90^\circ$ $a \neq b \neq c$				
Tetragonal	$\alpha = \beta = \gamma = 90^\circ$ $a = b$				
Trigonal	$\alpha = \beta = \gamma$ $a = b = c$				
Hexagonal	$\alpha = \beta = 90^\circ$ $\gamma = 120^\circ$ $a = b$				
Cubic	$\alpha = \beta = \gamma = 90^\circ$ $a = b = c$				

Figure 6. Each of the possible Bravais lattices, arranged according to crystal system and variations. Original work, with help from *Mathematica*.

surprisingly engaging treatment of the subject. For now, let it stand that one finds that there are 230 unique space groups to which a crystal can belong, and which are useful for assessing the various properties of a crystal [37, 38].

2.1.1.1 The Utility of Space Group Classification

Though in its own way interesting, knowledge of these symmetries and characterizations is rather beside the point if they do not produce a useful tool for dealing with crystals. The most basic perspective is that the concepts and lattices brought about by these symmetries are fundamental to the subject of crystallography. They represent a basic literacy in the field and any attempt at basic pedagogy would be sorely lacking to not touch upon it.

Beyond communication, however, symmetries are indicative of the physical properties of crystals. At a very fundamental level, solid-state physics has Neumann’s Principle, which reads “the symmetry elements of any physical property of a crystal must include the symmetry elements of the point group of the crystal.” [39] Note that this does not read only the symmetry elements of the point group. For instance, face-centered cubic crystals of metal, while notably symmetric in their own right, give rise to isotropic, or spherically symmetric, conductivity. Other aspects directly related to the symmetry (or lack thereof) in the crystal include the shear modulus tensor, the thermal coefficient of expansion, and even various thermodynamic behaviors including piezoelectricity [39]. Perhaps the most interesting examples, however, arise when a system does not have a center of symmetry—pyroelectricity [39], and non-linear optical phenomena [28]. In these cases, the absence of symmetry corresponds to an absence of balancing forces within the system, which yield the phenomena noted. Both are a clear demonstration of

how the knowledge of the symmetry of a crystal directly informs what studies ought to be made and to which uses it might be put.

Another, quite immediate use of such information is the identification of various crystals based on their x-ray diffraction patterns. In fact, Single-Crystal X-Ray Diffraction has proven singularly useful in this research, and so deserves a further exposition of its theoretical basis.

2.1.1.2 X-Ray Diffraction Theory

The principle of the technique lies in the interaction of a monochromatic x-ray plane wave with the atoms in a crystal lattice. As the wave comes in to a plane of atoms, it will reflect off of them with the same angle as it was incident, as shown in Figure 7. Crystals being eternally periodic, however, there will be an equivalent plane of atoms at some displacement d normal to the initial plane, and every integer multiple thereof. The inbound planewave of the x-rays are therefore reflected, and being waves, will interfere with one another. The majority of texts leave it at this point (e.g. [40]); this seems insufficiently rigorous. A more comprehensive treatment follows.

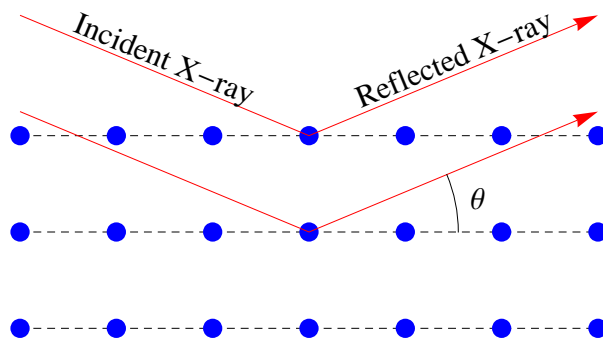


Figure 7. Waves incident, and waves reflected, at θ . In order to create a reflected wave, however, waves reflected from each plane must be in phase.

Working the algebra, one can see that the phase difference between two adjacent planes will be $2d \sin(\theta)$, and between planes m intervals apart, $2md \sin(\theta)$.

Therefore the reflected intensity will be

$$\sum_{m=-\infty}^{\infty} \sin(m\phi + \lambda x). \quad (5)$$

However, if one assumes that the offset ϕ is small or that the various $m\phi \bmod 2\pi$ values are numerous enough,² one can justify taking the following approximation:

$$\frac{1}{\phi} \sum_{m=-\infty}^{\infty} \sin(m\phi + \lambda x) \phi \approx \frac{1}{\phi} \int_0^{2\pi} \sin(\phi + \lambda x) d\phi = \frac{0}{\phi} = 0. \quad (6)$$

Therefore the crystal produces reflections only when the waves are truly in phase, which has the requirement

$$n\lambda = 2d \sin(\theta). \quad (7)$$

Equation (7) is known as Bragg's law [40]. As the wavelength λ of the system can well-known, an angle at which a spot occurs defines a relationship between n and d . In modern, computerized systems it is also practical to use a white X-ray spectrum so as to access all possible angles, and automate the processing of the very large number of points thus collected [28].

It also happens that the symmetries of a crystal can cause different sets of planes to interfere with one another. One extreme of these interferences is the limiting condition—any of those requirements which must be satisfied for a reflection to occur. At the other extreme, there are systematic absences—the conditions under which reflection will not occur [41]. (For a thorough theoretical development of this point, the reader is advised to consult [41].) The body-centered (BCC) and face-centered (FCC) cubic system provides a good example of this. In BCC, reflections are restricted to those planes with Miller indices that sum to an even

²Addition is commutative; the additions can be ordered according to $m\phi \bmod 2\pi$ just as easily as to m .

number, while those that sum to an odd number are systematically absent. In FCC, reflections will occur for planes that can be described by either all odd or all even Miller indices [28, 41]. Thus BCC lattices will have more reflections, and some of a different character from those generated by an FCC lattice, allowing for prompt discrimination between the two. As it happens, different limiting conditions and systematic absences are associated with different space groups [41], with the observation that greater degrees of symmetry within the crystal correspond to more restricted sets of reflections [34]. In any case, the combination particular spots that occur and those that fail to occur is most useful in identifying the space group of a particular crystal.

The last part of utilizing SXRD is an exercise in patience and data correlation. In many cases a crystal will not have an obvious orientation, or even clear faces, which makes associating a particular spot with a plane inside the crystal difficult. Nonetheless, by gathering enough spots correlated to enough angles, it is possible to determine which spots correspond to which reflections, what the planes must be, how they are spaced, and how they are oriented with respect to one another—in short, the entire crystal structure. If the dimensions and group belong to a previously characterized crystal, with plausible chemical composition according to the reactants, then one may be confident that the sample in question is that system. In ages past, it was necessary to measure spot positions on photographic plates and run the math by hand, but computers have reduced this drudgery significantly, and indeed bench-top SXRD machines, combined with robust analytical software, now make what was once the work of an entire doctoral thesis the work of an afternoon.

2.1.2 Crystal Structures and Band-Gaps

2.1.2.1 Mathematical Justifications

The presence of a periodic structure within a crystal gives rise to behaviors that are not seen in amorphous materials. For the work in question, the most important of these are formation of continuous regions within energy space that electrons may move about freely within, or are forbidden from. These are known, respectively, as bands and band gaps.

Beginning with a crystal lattice, then, one may simulate the electric potential seen by an electron as it moves past the assembled atoms in a straight line. Though in principle one can create an extremely detailed model of the potentials using basic electrostatic theory, with some assumptions about charge shielding from inner-shell electrons, such a detailed model introduces commensurate complexity into subsequent calculations. For tractability's sake, lower fidelity models are frequently invoked. The simplest—and easiest to use—is depicted in Figure 8; it will come up again later. Of course, the direction an electron travels through the lattice is important; it will have an impact on the potentials and periodicity of the lattice, as illustrated in Figure 9. Differences of direction in the lattice have very real consequences, particularly in semiconductors [28, 42], but fortunately, the mathematical origin of the band structure can be derived from a one-dimensional mode. So the electron sees a periodic potential $V(x)$ as it travels in this one-dimensional lattice model, and a direct consequence of this periodic potential—it does not hold for an aperiodic system—is the Bloch theorem. This states that an electron moves through a periodic lattice nearly as free-space plane-wave, save that it picks up a complex phase e^{ikan} as it moves, where a is the periodicity of the lattice, k is the wavenumber, and $n \in \mathbb{Z}$ [43].

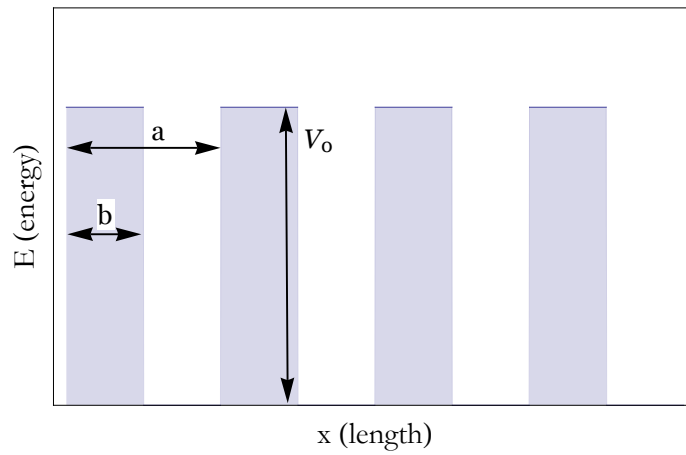


Figure 8. This is the schematic of a highly simplified, but easily tractable model of the potential seen by an electron as it traverses a one-dimensional lattice.

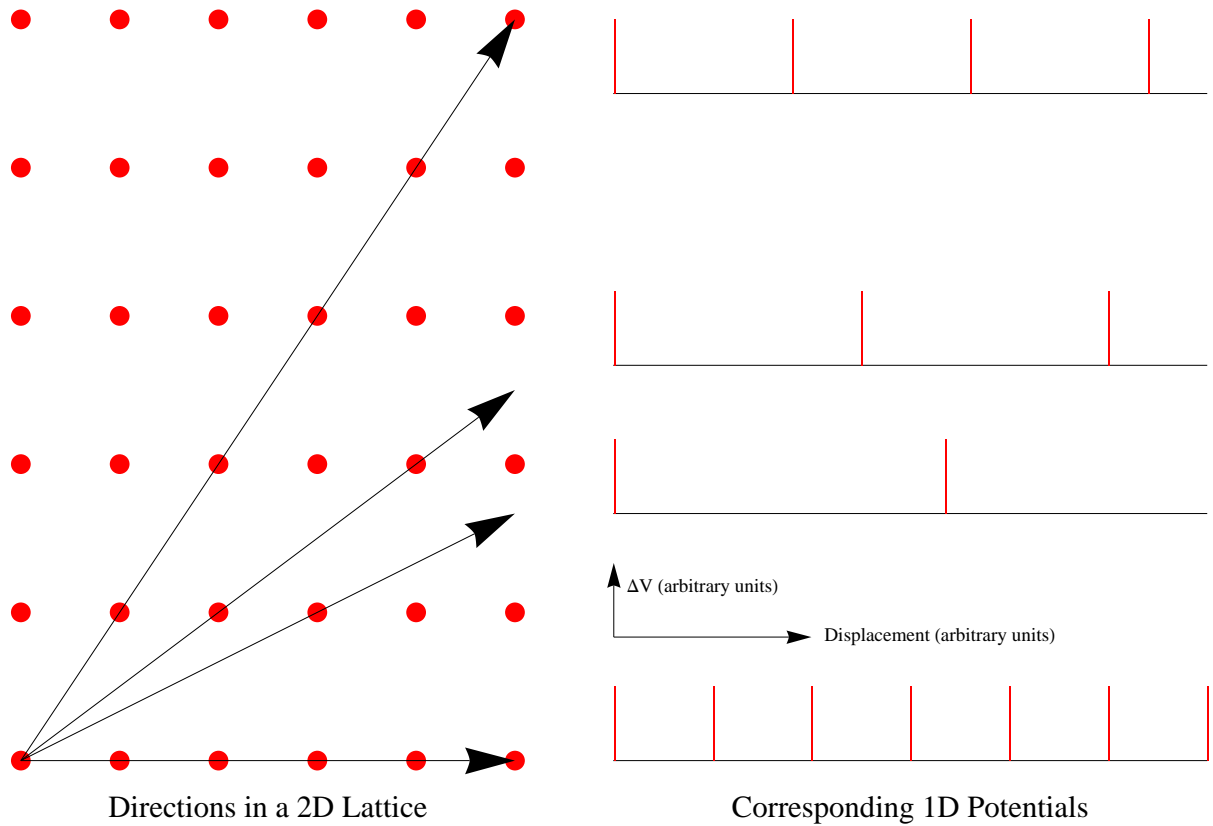


Figure 9. Directions in a 2-D lattice give rise to different potentials, with corresponding changes in behavior.

In 1931, the researchers R. Kronig and W. Penney devised an approximation to a crystal lattice that is, at least, pedagogically useful. By assuming that the real potential $V(x)$ could be approximated in a periodic top-hat function of the form (c.f. Figure 8)

$$V(x) = \begin{cases} V_0 & na \leq x < na + b & \text{Region I} \\ 0 & na + b \leq x < (n+1)a & \text{Region II.} \end{cases} \quad (8)$$

The solution to the Schrödinger equation in both regions is well-known, and at the boundary their values and first derivatives must be equal [44]. Furthermore, the Bloch theorem places requirements on the nature of the solution at every boundary in the potential, thus changing the problem from a problem in infinite space, to a finite-space, Dirichlet-boundary problem. Its solution is the transcendental equation [43]

$$\frac{mV_0ba}{\hbar^2} \frac{\sin(a\sqrt{\frac{2mE}{\hbar^2}})}{a\sqrt{\frac{2mE}{\hbar^2}}} + \cos(a\sqrt{\frac{2mE}{\hbar^2}}) = \cos ka. \quad (9)$$

Given the range of the cosine function, this is only tractable when $-1 \leq \text{LHS} \leq 1$, and so gives rise to a band-structure of the sort depicted in Figure 10.

In particular, this curve is usually subsumed into a linear schematic, much like that shown in Figure 10, assuming $k = 0$. This is entirely justified in that an electron (or hole) will explore the entire phase space [43], and therefore the local minimum transition energy is the most important part in determining the characteristics of the transition from one band to another. It is also worth noting that though mathematical tools for working with three-dimensional lattices of more realistic potentials have been developed, they are neither necessary nor particularly helpful for the further development of this work. Far more useful at this point is to understand conceptually what the various implications of band structure are.

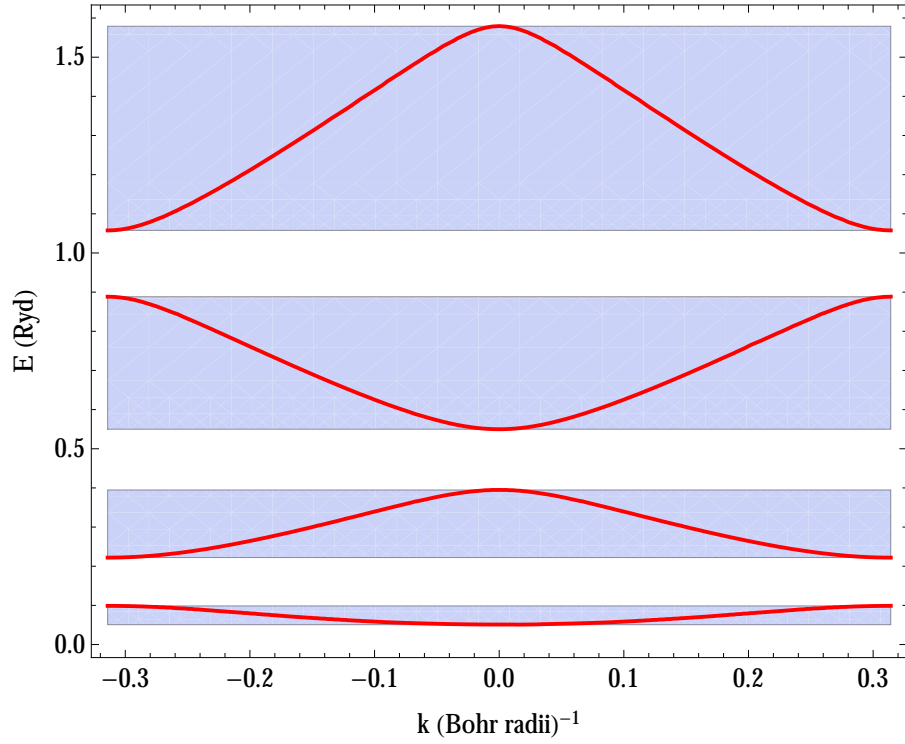


Figure 10. The red lines are the various contours of solution of 9, using $a = 10$ Bohr radii and the mass of coefficients on the LHS forced to $3\pi/2$, after [43]. The blue regions themselves are the regions in which the LHS of 9 lies within $[-1, 1]$, thus allowing a solution to exist—that is to say, the bands of allowed energy.

2.1.2.2 Electron Band Structure

Thus far the lattice has been an external object through which a lone electron might move. This is not really the case; every electron in the crystal, from the tightly-bound 1s-orbitals to those just about to escape, has an associated energy that must lie within a band. Each band reflects certain properties as well: the valence band is so named because it contains those states which participate in chemical bonding and hold the crystal together. The conduction band pertains to those states in which electrons are free to move around the lattice and thereby conduct electricity [45]. Furthermore, each band has a finite density of states for electrons to occupy. The Pauli Exclusion Principle demands that each state hold at most one electron. In the very coldest of conditions, at or near absolute zero, all of the electrons in the lattice will be in the lowest energy states available. Then the energy possessed by the most energetic electron in the lattice is the Fermi energy, E_f [29, 46], above which there are no electrons. In most cases, though, there will always be some thermal energy, and some of the electrons in the system will be excited to higher energies.

What occurs with the heating of the system depends significantly on the position of the Fermi energy with respect to the bands. If the conduction band is partially filled, as on the left side of Figure 11, or contiguous with the valence band, as it is in metals, then there exist, effectively, a continuum of energy states for the electrons to move in to smoothly. It is not so simple for semiconductors, in which the full valence band and empty conduction band are separated by a gulf. Only if an electron should receive enough energy to move it to the conduction band will it leave the valence band. This is, of course, the band-gap energy E_g . Then the Boltzmann distribution,

$$n_e = N_e \exp\left(-\frac{E - E_f}{kT}\right) \quad (10)$$

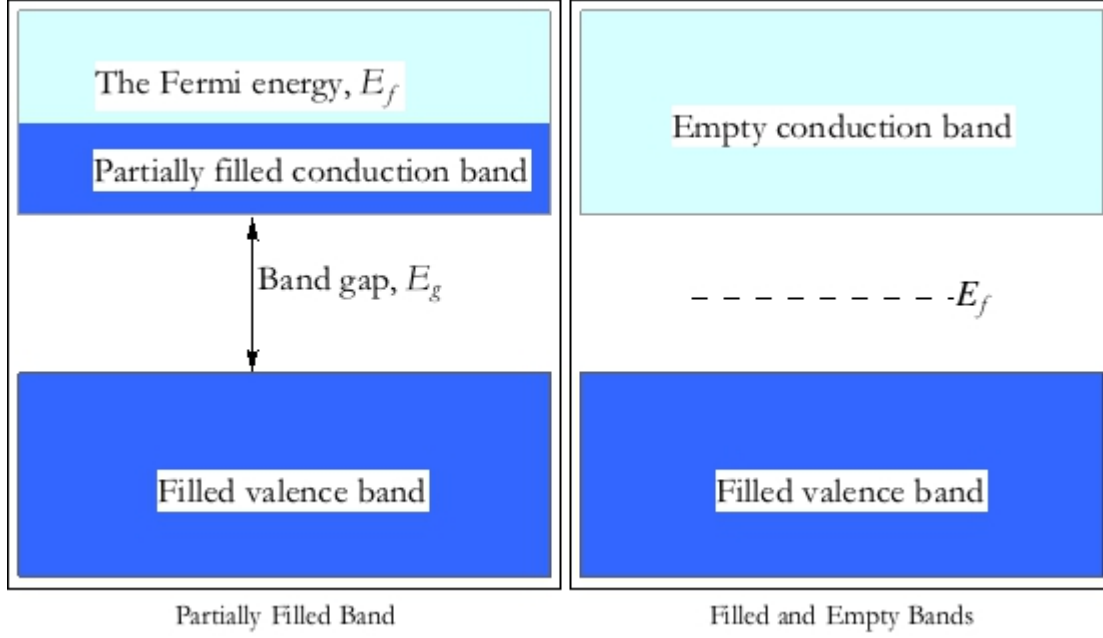


Figure 11. These images depict the possibilities of the electrons in a crystal either not completely occupying the states available in a band, as on the left, or reaching the top of a band before continuing, as shown on the right.

describes the density of electrons to be found at energy E , where N_e is the effective density of electron states in the system. Note, also that E_f is, in this case, the Fermi level and not energy as discussed before. This energy is that which describes, in the Fermi-Dirac distribution, the energy at which it is just as likely to find a state filled as empty—and is a fiction, insofar as it usually resides in the band gap. Also regarding useful fictions, the depiction of Figure 11 is also idealized, in that there are no impurities or defects in the crystal that would give rise to possible energy states within the forbidden zone—an intrinsic semiconductor. In such a system, electrons are excited to the conduction band only with the generation of holes in the valence band, and the reverse. In this case, the Fermi level may be interpreted as $E_f = E_g/2$ [46].

2.1.2.3 Doping

As it happens, intrinsic materials are uncommon. Unavoidable defects and impurities within the structure can form hole or electron traps within the band structure, and change the character of the material. Frequently, however, these defects are deliberately engineered, creating the class of doped materials. In these, additional dopant atoms have been added to alter the electrical properties of the system by providing additional electrons, or removing them. (It is, however, common-place to refer to the absence of an electron in the valence band as a hole, and treat it as an entity in its own right.) A good dopant will possess a chemical potential near the edge of the band-gap, to within fractions of an electron-volt; various potential dopants and their potentials within the Ge system are depicted in Figure 12 [47]. Those that are close to the valence band generate a hole by allowing an electron to jump up to their state and holding it there, and are known as acceptors. Similarly, those that are close to the conduction band have electrons that easily jump to the conduction band, and are known as donors [28]. The very small energy gap between the dopant and its neighboring band also makes the transition very easy, so that they provide charge carriers at all but the coldest temperatures, as depicted in Figure 13. This dominates the number of charge carriers in the system for all practical temperatures, and allows for some control over the conductivity of the system [28].

Dopants introduce their own difficulties, of course. By definition, they do not have a place marked out for them in the highly-ordered unit cell making up the crystal; they inherently disorder the system. Their density tends to be orders of magnitude less than the plenum surrounding them, however, and their advantages are great, so one asks where they shall fit in the system. There are two options: replace one of the atoms in the lattice, or fit into a space within the lattice. These

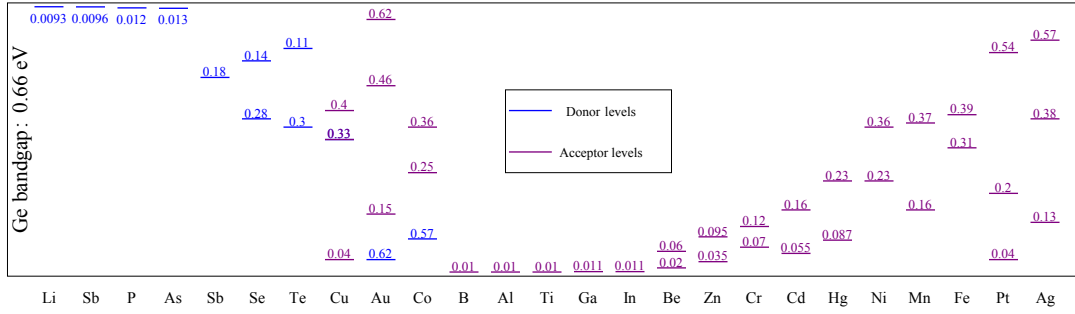


Figure 12. The lines within the band-gap depict where the dopant energy states are with respect to the conduction and valence bands. Those below the gap center accept electrons and provide holes to the conduction band. Likewise, those above the gap center donate electrons to the conduction band. The dopants very near the gap center are deep-level dopants and are commonly avoided. Figure is original; data comes from Sze [47].

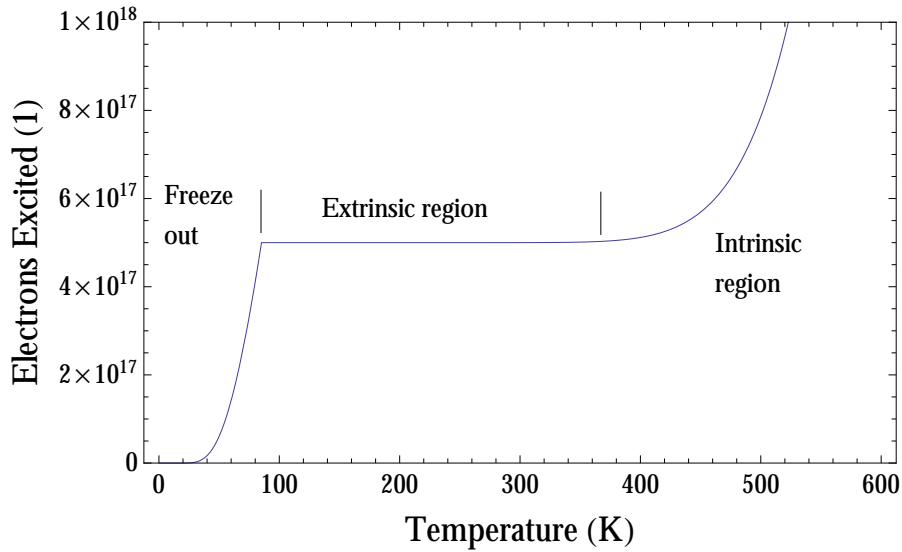


Figure 13. The plot shows a crystal of 10^{23} atoms doped with 5×10^{17} donors. The band gap is 1.1 eV and the donor level 0.044 eV below the conduction band. As shown, when the system is at cryogenic temperatures, there are very few electrons excited into the conduction band because even the very small gap from the donors is relatively improbable. In the extrinsic region, including room temperature, the system plateaus because almost all of the dopants have donated their electrons to the conduction band and become limiting. Finally, in the intrinsic region, the temperature is enough that the much larger excitation of the band-gap becomes favorable, and it outstrips the extrinsic level simply as a matter of available electrons.

are known, respectively, as substitutional and interstitial dopants. Which happens depends on charge balance, chemistry, and of course the sizes of the dopant and host atoms. A 10 mm ball-bearing will not adequately replace a racket-ball in a lattice made of the latter, but it might squeeze in between them quite satisfactorily; similarly, a racket-ball will not fit into the space leftover in a tennis-ball lattice, but could take one of the tennis-ball positions.

As discussed in the section on symmetry, all the various atoms in a crystal will arrange themselves into one of the Bravais lattices. The volume that they occupy, and the particular choice, however, depends on the charge and volume of the various constituents. NaCl, for instance (Figure 14), has chlorine on a face-centered cubic (FCC) lattice, with the sodium in the octahedral spaces between them. FCC is as closely packed as identical spheres can get; after the inclusion of the sodium, there is very little space left-over in the lattice to place an additional atom, so any dopant in this lattice would likely be a substitution. Silicon, on the other hand, forms a very open lattice, as shown in Figure 15. Interstitial doping becomes more likely in this case, as space is more available in which to fit an additional atom—though not guaranteed. In practice, the usual silicon dopants, phosphorous and boron, bond covalently with the silicon and become substitutional.

As $\text{Li}_2\text{B}_4\text{O}_7$ has a very large band-gap [48], it is appropriate to consider doping the crystals in order to modify the conductivity. Other authors have certainly made inroads to this subject, particularly with alkali metal, transition metal and even rare earth dopants, though the transition metals were the most common choice [11, 12, 14, 26, 49–51]. Many of these works were solely concerned with the thermoluminescent response of the $\text{Li}_2\text{B}_4\text{O}_7$, and prepared their bulk samples via sintering. Czochralski growth also proved capable of incorporating Cu into the lattice [13, 16, 50], apparently increasing the conductivity of the material [13, 50]. To

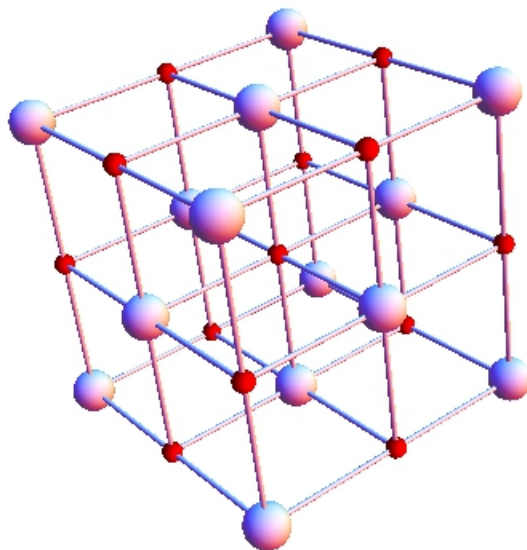


Figure 14. NaCl has the Face-Centered Cubic lattice. The larger magenta spheres are Cl^- and the smaller red spheres are Na^+ .

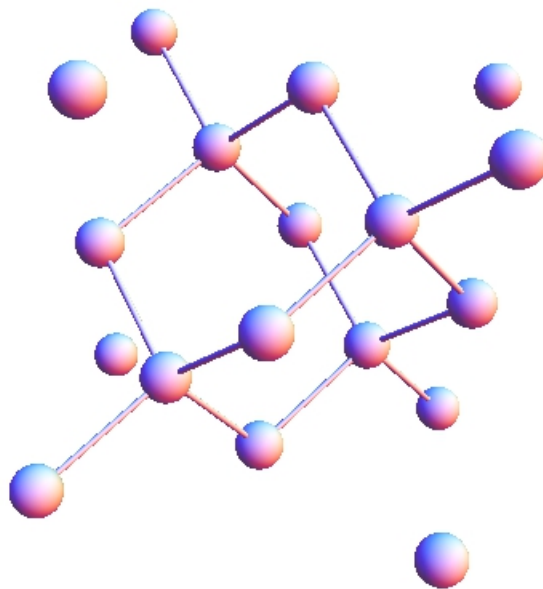


Figure 15. Diamond's lattice is essentially two interpenetrating FCC structures, leading to the large open frame depicted. All the spheres are carbon, with the pipes indicating the positions of the covalent bonds holding the structure together. This must not be underestimated: the preferential directions adapted by covalent bonding give rise to the very open structure seen, as opposed to the very dense structure of the ionically bonded NaCl shown in Figure 14.

the author’s knowledge, no efforts have been made to dope $\text{Li}_2\text{B}_4\text{O}_7$ while applying the hydrothermal growth method. Prior research has shown that copper substitutes on to the lithium sites [26, 27, 50, 52, 53]. As further speculation, it also appears that cobalt remains untried; Co^{2+} could substitute for lithium, as their ionic radii match reasonably well [29]. In any case, in order to effectively dope the material, it would be helpful to introduce a large number of dopant ions into the mineralizer solution, of sufficient concentration that it is favorable for them to displace the lithium. It would also be appropriate for this to be a material incorporated with the feedstock, with a similar rate of dissolution so that the proportion of copper ions in solution remains as consistent as possible throughout the growth run.

The author also speculates that one other method of doping $\text{Li}_2\text{B}_4\text{O}_7$ may be practical, though it seems to have not yet arisen in the literature. From [54], the bonding of the borons and oxygens are covalent and form negatively charged complexes; these are balanced by the lithium ions within the lattice. At the same time, electrons tend to have a greater mobility than holes: in order for a hole to move, all the electrons around it must shift, which takes longer than a single free electron moving [28]. Therefore a modification to the boron seems advantageous. From the periodic table, two plausible electron donors are carbon and phosphorous. Lithium tetraborate contains both trigonal planar and tetrahedrally coordinated boron-oxygen groups; phosphorous forms the common and stable group PO_4^{3-} , phosphate. This work therefore proposes that donor doping could be achieved by the simple admixture of some lithium phosphate salt in the initial charge, improving the utility of $\text{Li}_2\text{B}_4\text{O}_7$ for direct detection.

2.1.2.4 Crystalline Imperfections

The crystals so far discussed have all been perfect examples of their kind. From the discussion of crystalline nature and symmetry, it is obvious that there exists exactly one way to form a perfect crystal. The crystal will still hold together if a few atoms are missing. Then one mole of crystal with n atoms missing has

$$\frac{(6.022 \times 10^{23})!}{n!(6.022 \times 10^{23} - n)!} \quad (11)$$

possible ways of forming. The odds are not in favor of a perfect crystal.

In point of fact, the whole of defect formation derives from statistical mechanics. It is true that the crystalline form is the most enthalpically favorable: by arranging themselves in a crystalline pattern, the atoms minimize the amount of electrical attraction and repulsion that they each experience, as allowed by their various sizes. However, in constant-temperature and constant-pressure conditions—in short, under idealized hydrothermal crystal-growth conditions—the quantity to minimize is not the lattice enthalpy alone, but the Gibbs free energy

$$G = E - PV - TS, \quad (12)$$

where E is the enthalpy of the lattice, PV is the pressure work done on the system, and S is the entropy [29, 55]. As a quick review, entropy is defined as

$$S = k_B \log \Omega \quad (13)$$

$$\Omega = \frac{N!}{n!(N - n)!}, \quad (14)$$

where k_B is Boltzmann's constant and Ω is the statistical weight of the system, borne of the combinatorics of the number of deviances from the ideal, n , and the

number of places that they could be located, N (c.f. equation 11). It must also be borne in mind that $E = E(\text{defect concentration})$, for each defect takes the system away from its ideal minimum entropy, so that an arbitrary increase in entropy does not necessarily minimize G . If it did, then crystals would not form.

That said, the total derivative of G with pressure, volume, and temperature constant, is $dG = dE - T dS$. Starting with the definition of entropy above and using Stirling's approximation to make the factorials tractable, some algebra shows that

$$\frac{\partial S}{\partial n} = k_b \log \frac{N - n}{n} \approx k_b \log N \quad (15)$$

for $n \ll N$, which is true in proportion to the degree of perfection of the crystal. Indeed, as $n \rightarrow 0$, $\frac{\partial S}{\partial n} \rightarrow \infty$. It follows that a perfect crystal will never form.

It follows immediately from these considerations that the lower the temperature of formation, the smaller the impact of entropy, the more the crystal will minimize E at the expense of S . Therefore, the lower the temperature that the crystal can be grown at, the better—and this is an aspect in which hydrothermal growth excels. The ThO_2 and UO_2 systems here considered have melting points of $3377 \pm 17^\circ\text{C}$ [56] and 3120°C [57], respectively; Mann's work in hydrothermal growth thorium compound synthesis rarely, if ever, surpassed 750°C [58]. (Consult the section Prior Work for more details.) The advantage is clear, but can be emphasized to an even greater degree because the functions S is not a linear function of temperature. Many defects—point defects, in particular—form according to

$$\frac{n}{N} \propto \exp\left(-\frac{H}{kT}\right), \quad (16)$$

where H is the total energy for forming a defect [29]. It follows that the defect concentration increases exponentially with temperature, and every new defect has a

profound effect resulting from the combinatorics of states. Decreasing the temperature of the growth is therefore highly desirable.

2.2 The Hydrothermal Growth Technique

Hydrothermal crystal synthesis refers to any growth process that relies upon a working fluid at pressures and temperatures above standard to dissolve feedstock, transport it, and deposit it upon a suitable seed [59]. A key advantage of this process is that materials nominally insoluble in water under standard temperature and pressure conditions become soluble with the change in conditions. Solubility can be further increased by the use of a mineralizer—some chemical added to the working fluid. In such cases, the technique is occasionally referred to as solvothermal growth, depending on the composition of the solution and pedantry of the author [60, 61].

Hydrothermal growth, by necessity of the elevated pressures encountered, occurs within a closed vessel, referred to as an autoclave [59–61]. Depending upon the reaction conditions, pyrex or other glass may be mechanically strong enough and sufficiently inert enough to contain the pressurized liquid [59], while other growth experiments may require nickel super-alloy autoclaves with precious-metal internal containers [58]. Similarly, the sealing and heating mechanisms may vary according to the work undertaken, the ingenuity of the user, and of course the availability of different types of equipment. Nonetheless, a universal aspect of the autoclave is that its internal structure is columnar. The upper and lower regions are provided with independent heating mechanisms, so that the temperature in each may be set and a temperature gradient ΔT established between the two; a fluid baffle is provided to prevent the fluid mixing from occurring too rapidly and averaging the fluid temperature out entirely [58, 61]. (See Figure 16.)

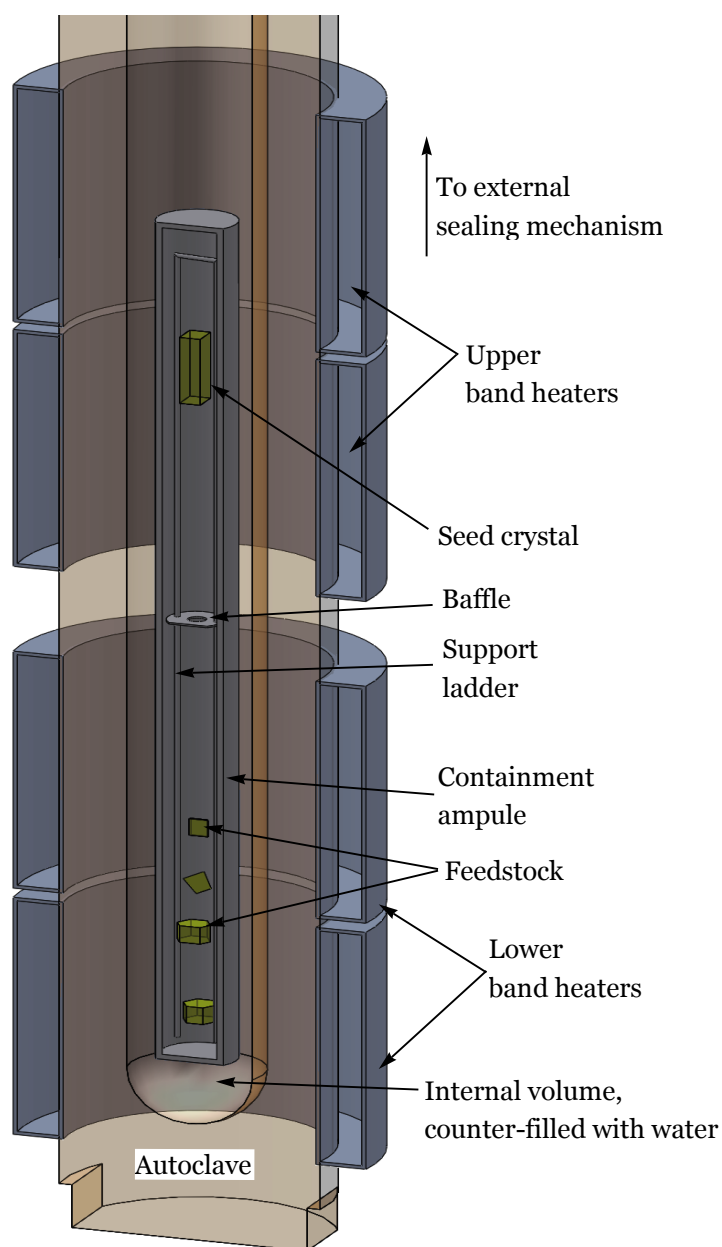


Figure 16. This is, generally, what one might expect in a metal hydrothermal autoclave. The aspect ratio, foremost, is quite elongated in order to provide separation between growth and dissolution zones. Both pairs of band heaters are generally linked together to provide one upper temperature and one lower temperature; they are controlled by thermocouples and a feedback loop to a suitable control circuit (not shown). The sealing mechanism is not shown as its particulars are immaterial so long as they contain the reaction. The seed crystal is, as shown, supported by a ladder made of the same material as the containment ampule, tied on with fine metal wire. The ampule itself is frequently welded shut, though in some cases it is an integral part of the autoclave itself.

The necessity of a temperature differential between the upper and lower regions of the system is a result of the thermodynamics driving the system. In the region containing the feed material—almost universally the lower part of the autoclave, as the reverse is much more difficult—the temperature is high enough that the solution is capable of dissolving the material. Convection carries this saturated fluid to the growth region, where it cools slightly. In a positive solubility system, this reduces the solubility of the material, but not its concentration; the fluid is thus supersaturated, and the dissolved feedstock then finds it more favorable to precipitate out. Nucleation can occur anywhere that the energy of forming a bulk material is more favorable than forming a surface potential [28], and is particularly favorable if an existing seed of the same material is present. The solution thus cooled and depleted of its mineral charge, sinks back to the feedstock region, ready to begin again.

Hydrothermal growth also requires that a number of considerations be met:

- The first, most obvious requirement is that a mineralizer solution suitable for growing the material must be found. A solubility of 1 to 5 weight % dissolved has been a range generally found to work for hydrothermal growth. Less than this, and the reaction does not proceed quickly; more than this, and the reaction may show excessive spontaneous nucleation away from the growth crystal [61]. A further problem is that an overly super-saturated solution will experience kinetic, rather than thermodynamic, growth, which is unsuitable for high-quality crystal formation; faster growth tends to lead to more flaws [34, 62, 63].
- The solubility of the material must have a sufficient temperature dependence so that it will become reasonably supersaturated between the two regions of the autoclave. Autoclaves are not uncommonly made of metal, and certainly

have mixing fluids inside; the degree of thermal gradient that a particular apparatus can support is restricted by the length of the autoclave itself [46,64]. Therefore, if $\frac{\partial S}{\partial T}$ is too small, where S is solubility, it will be difficult for ΔT to be large enough to support timely growth [61]. At the same time, should $\frac{\partial S}{\partial T}$ be large, then control becomes a problem. The change in solubility should be maintained within the range discussed, and constant if at all possible; call the allowable deviancy in solubility δS and the precision of the temperature controller δT . Then it follows that

$$[\delta S]_{T_1} = \delta T \left[\frac{\partial S}{\partial T} \right]_{T_1} \quad (17)$$

$$\begin{aligned} &= [\delta S]_{T_1} + [\delta S]_{T_2} \\ &= \delta T \left(\left[\frac{\partial S}{\partial T} \right]_{T_1} + \left[\frac{\partial S}{\partial T} \right]_{T_2} \right). \end{aligned} \quad (18)$$

Though the minimum δS attainable will depend on the particular equipment available, it still follows that for a given experimental set up, there will be some $\frac{\partial S}{\partial T}$ which it cannot reliably control.

- The working fluid must be sufficiently inviscid and susceptible to convection as to allow a timely growth process [60,61]. Beyond these basic requirements, it is also highly desirable that the mineralizer be inexpensive, readily available, cheaply contained (i.e. silver instead of platinum), and safe to handle [60,61].

Naturally, these stringent requirements will not always be met, such that not every system is suitable to hydrothermal growth—but the suitability is not always obvious at the outset.

It follows that a great deal of preparation must go into designing a hydrothermal growth experiment if there is to be a reasonable hope of success. In the beginning,

there are phase studies, which map out the stable products formed according to the mineralizer solution and starting chemistry. A detailed example of this lies in Mann’s work, in his early exploration of the $\text{BaO-TiO}_2\text{-Ta}_2\text{O}_5$ system within a 6.0 M CsF solution: the various starting ratios led to such products as BaTa_2O_6 , $\text{BaTi}_5\text{O}_{11}$, $\text{Cs}_2\text{TiOF}_4 \cdot \text{H}_2\text{O}$, the latter of which illustrates how the mineralizer may not be as inert with respect to the system as the experimenter may have originally hoped. The value of a phase study is further shown by Mann’s work, when one notes that a change in the starting ratios gave rise to two different, stable crystal products with the same stoichiometry [58, p. 140ff]. Pressure and temperature variations are also crucial to the phase study. Quartz, for example, experiences a phase transition at roughly 573°C [60]; α -quartz cannot be grown above this temperature. Which, incidentally, forces quartz to be grown hydrothermally, and is thus responsible for major developments in the technique [60].

Solubility studies are also vital—they map out $\frac{\partial S}{\partial T}$ for a particular material and mineralizer solution combination. Though experimental technique may vary, the essence is to establish a balance, for a given temperature, between the solid and solute phases of the feedstock [31]. Naturally, they follow after a determination of the phase diagram: solubility requires that the material be stable within the solution. If this were not the case, then the continuous dissolution and re-precipitation inherent to chemical equilibrium could not arise, undermining the basic premise of the solubility study [65]. Once accomplished, however, the solubility graph will indicate where regions of appropriate $\frac{\partial S}{\partial T}$ exist, if at all.

Once suitable solutions have been found and temperatures achieved, all that remains is to use the data to design a transport growth experiment. Relevant decisions include the temperatures, percentage of fluid fill, amount of feedstock, the run duration, and the seed. Regarding the last item—hydrothermal growth can

occasionally make use of templated growth. It is not an easy process, nor guaranteed success. At the very least, a seed crystal must be found with an satisfactory lattice match to the desired material phase, and it must be stable within the hydrothermal solution. Even assuming that a suitable material can be found, the thermodynamics of the growth are not in favor of uniform epitaxial growth on the substrate. Finding a perfect lattice match between two species cannot be counted upon, so the grown species will experience some strain in its own lattice as a result. As a small region grows out, it will be increasingly able to relax this strain. The equilibrium position is the most energetically stable point; it is generally easier for dissolved solute to affix itself to existing regions of growth, rather than fit to the rest of the exposed seed. This can, in some cases, be compensated by orienting the growth surface so that the faces of the substrate are perpendicular (or so) to the fastest-growing crystal surface [28, 34]. In any case, assuming that one has had the persistence, resources and luck to create a suitable template seed, all the reaction materials are placed in the apparatus as shown in Figure 16, and the run begun. Not that even a successful run means the end of the development—the heating profile in time, the growth rate, the fill, and similar, must all be optimized to produce high-quality crystals in a timely fashion. After sufficient experimentation, however, it may be that one finds an excellent set of parameters for growing the material and the process moves from the laboratory to the factory.

2.3 Prior Work

$\text{Li}_2\text{B}_4\text{O}_7$, lithium tetraborate, has been proposed for neutron detection. As noted, lithium and boron both have isotopes with large cross-sections, but moreover $\text{Li}_2\text{B}_4\text{O}_7$ is dense in both species—it has 1.71×10^{22} Li/cc and 3.42×10^{22} B/cc [66]. This improves the macroscopic neutron-interaction cross-section of the material (c.f.

Eqn 1 and surrounding discussion), and is superior to the density of a number of other lithium-borate species, e.g. lithium metaborate hydrate, $\text{LiBO}_2 \cdot 8\text{H}_2\text{O}$, which has only $4.29 \times 10^{21} \text{ cc}^{-1}$ of either species [66]. At the same time, all of the elements in the lattice are low-Z materials: this makes their inner-most electrons less tightly bound, and correspondingly their gamma-ray absorptivity is significantly below that of the transition metals or the actinides [9]. The lithium borate crystals are therefore a strong candidate for gamma-insensitive neutron detection [13].

Lithium and boron based detectors also offer a number of advantages over the actinide oxide based detectors:

- Availability: the lithium and boron neutron-sensitive isotopes are far more prevalent in nature than those of uranium. ^{10}B constitutes 19.9% of naturally-occurring boron, and ^6Li 7.59%. This compares quite favorably to ^{235}U , at 0.7204% [8]. Furthermore, both ^{10}B and ^6Li are available in enriched quantities [1]—something which is emphatically untrue for ^{235}U .
- Cross-sections: both ^{10}B and ^6Li have substantial neutron capture cross-sections in the thermal regime. For ^{10}B , $\sigma = 3840$ barns and for ^6Li $\sigma = 3840$ barns, [1], both of which are higher than that of ^{235}U $\sigma \approx 520$ barns [67].
- Lithium borates are significantly easier to work with than actinide systems. The mineralizers explored in the literature are less caustic, cheaper, and easier to work with than the CsF thus far utilized in the actinide literature.
- Neither lithium or boron have radioactive isotopes naturally found on earth [8]. This makes their handling much simpler than that for uranium and thorium, as radiation safety protocols are unnecessary.

When a neutron strikes either boron or lithium, the most likely outcome [2] that the excited nucleus will emit an α particle or a triton, according to the following reactions:



Given these reactions, an engineer can design either to detect the heavy charged particles themselves, the gamma occasionally released by the lithium reaction, or the persistent changes they bring about in their surroundings.

Detecting the α or triton particles directly requires one of two possible conditions: first, that the surrounding material is itself suitable for the detection of an α , or that the particles escape the reaction medium into a detector that is. A quick consideration of the linear energy transfer of heavy charged particles reveals that in order to have a reasonable proportion of α s to escape, the surface-to-volume ratio of the detector must be exceedingly large, at the expense of the detector volume [68]. This is inimical to capturing the neutrons in the first place. Alternatively, the heavy charged particles might dissipate their energy within the neutron-reactive medium. This occurs, for instance, in a BF_3 gas detector [1], or in a LiI scintillator liquid [1]. In the latter, the light released by the scintillator must itself be picked up by a photomultiplier tube for subsequent detection.

$\text{Li}_2\text{B}_4\text{O}_7$ can already be used as a neutron detector via thermoluminescence [7, 11, 12, 12–14, 27, 51]. In this process, neutron-reaction imposed damage to the crystal creates metastable potentials within the lattice which, when heated, have enough energy to transition down to their entirely stable

state and in so doing emit light [69]. Recent research suggests that this may be a result of hole mobility [14, 15]. $\text{Li}_2\text{B}_4\text{O}_7$ has a substantial band-gap [48], and damage in crystals can cause deep-level energy states within the gap [70], it may be that the radiation damage caused by the energetic dissociation of one of the lattice nuclei provides a trapped energetic site within the system. It has also been shown that copper impurities and lithium vacancies within the system trap holes, and release them upon heating [27]. In any case, the total amount of light released upon heating appears to be linear with respect to the number of neutrons to which the lithium tetraborate was exposed and insensitive to storage [11].

It is further worth noting that Pekpak *et al.* have shown that the thermoluminescent response of $\text{Li}_2\text{B}_4\text{O}_7$ powder depends upon the mode of synthesis [51]. Of course, powder synthesis is significantly easier than producing single crystals, and for this reason objections have been raised that the powder work obviates the present crystal growth efforts [34]. This is not the case: crystal systems have advantages over powders, and particularly in the transmission of light for thermoluminescence. A cubic crystal, for example, has only six interfaces at which refraction might occur; a powder has a surfeit of these positions to scatter light. As a commonplace example, consider the difference in transparency between calcite crystal and powdered CaCO_3 —it is far easier to get light through the bulk of the crystal than the powder, to say nothing of limestone. Similarly, the powder work does not apply to the creation of scintillators, and it would be entirely impossible to use them for solid-state fission-chambers in a single-stage neutron detector.

In any case, Pekpak’s team synthesized $\text{Li}_2\text{B}_4\text{O}_7$ both by reacting dry precursors at 750°C , with repeated grinding to increase surface area, and by reacting the precursors in water, before finishing with a dehydration reaction at 750°C . Their subsequent curves of luminescence as a function of temperature show several peaks,

separated by $\sim 150^\circ\text{C}$, for the dry-synthesized materials, with only one, relatively low-temperature peak for the solution-assisted synthesis [51]. Their own analysis does not discuss why this should be, nor did they perform EPR or other defect characterization, but an explanation corroborative to both the virtues of hydrothermal growth and the legitimacy of the defect hole trapping explanation presents itself: the elevated synthesis temperatures of the solid-state reaction, combined with the mechanical work done, would conspire to insert lattice defects in the microcrystalline powder. These defects could generate hole traps of varying depth, with the temperature to excite them out increasing monotonically with the depth. This would give rise to the several peaks observed. Contrariwise, the solution-assisted process, though not hydrothermal, still had less time at high temperatures and no grinding, both of which would improve microcrystalline quality. This is manifest in that there is only one peak, and it is at temperatures similar to the lowest of the solid-state temperature peaks.

Another possibility for neutron detection lies in changes in electrical properties [17]. Though $\text{Li}_2\text{B}_4\text{O}_7$ has a band-gap ranging from $8.9 \pm 0.5 \text{ eV}$ to 10.1 ± 0.5 [48], and is therefore considered an insulating material [71].³ This is not, however, a disadvantage. The presence of the neutron capture reaction products, in their deposition of energy, will excite electrons from the valence band to the conduction band [1]. This increase in charge carriers will in turn increase the conductivity of the material, in accordance with $\sigma = n\mu q$, where σ is the conductivity, n is the charge carrier density, μ the mobility of the carriers, and q the charge [72]. By placing a potential across the crystal, this change in conductivity can be measured either directly as a change in current, or indirectly using a Wheatstone bridge arrangement [73]. In the current-sensing configuration, the

³The exact boundaries between a semi-conductor, a wide-gap semi-conductor, and an insulator remains imprecisely defined, but [71] cites diamond, bandgap 5.2 eV, as an insulator.

insulating nature of the material will tend to reduce the background, or leakage, current, making it easier to detect the change [1]; in the other case, a higher conductivity would likely be desirable. Fortunately, $\text{Li}_2\text{B}_4\text{O}_7$ has taken well to doping when grown via the Czochralski method [49, 50, 74], potentially increasing conductivity [75]. This provides hope that $\text{Li}_2\text{B}_4\text{O}_7$ may be doped when grown by the hydrothermal method, but success is not at all guaranteed. As discussed previously, doping in the kinetic regime of Czochralski growth is quite different from the thermodynamic regime of hydrothermal growth: the adherence of a dopant to the growth surface of the crystal must be sufficiently stable to remain until more dissolved $\text{Li}_2\text{B}_4\text{O}_7$ arrives and permanently traps the dopant within the crystal. Finding a set of conditions which will be suitable both for growth and inclusion of specific impurities is likely to be a difficult process. That said, the projected benefits are worth the effort: once doped, the crystals should show improved conductivity and utility for single-stage detection [50].

$\text{Li}_2\text{B}_4\text{O}_7$ crystals have been grown by a number of methods, primarily the Czochralski [19–21, 76] and Bridgman melt [22, 26] methods. Rather less work has been done in the vein of its hydrothermal growth. Byrappa *et al.* have succeeded in synthesizing the system, with a variety of different morphologies, within an acidic growth solution [77]. McMillen *et al.* have likewise achieved hydrothermal synthesis of $\text{Li}_2\text{B}_4\text{O}_7$ in a deionized water solution, from either pure $\text{Li}_2\text{B}_4\text{O}_7$ or $\text{Li}_2\text{B}_4\text{O}_7$ with either B_2O_3 or LiOH added. It should be noted, however, that the LiOH solution produced $\gamma\text{-LiBO}_2$ and $\text{Li}_2\text{B}_4\text{O}_7$, rather than $\text{Li}_2\text{B}_4\text{O}_7$ exclusively [78]. Other hydrothermal work [78–80] has revealed hydrated phases formed under hydrothermal conditions, but, as discussed above, they are less dense in lithium and boron nuclei than the $\text{Li}_2\text{B}_4\text{O}_7$, making them less desirable for neutron detector materials. As such, they are not as relevant to the research in question, other than

to affirm that much work remains to be done in the the field of hydrothermal lithium borate crystal growth.

3. Experimental Technique

A broad outline of the the technique may be found in section 2.2; this explication will deal with the particulars. Section one, *Growth Apparatus*, acquaints the reader with the actual objects in question so that their application may be understood throughout the rest of the work. The following section, and subsections, are an elaboration of the methods used for each type of experiment carried out in this work.

3.1 Growth Apparatus

The experimental work used a variety of different autoclaves, all machined from Inconel 718 or Rene 41. Though significantly more expensive than comparable stainless steel autoclaves, these nickel superalloys retain their great strength at much higher working temperatures, making them the more versatile choice for a well-appointed laboratory. At the outset, there were two types of autoclave for the research: the smaller, whose interior cylindrical cavity was approximately 8.5" deep and 3/8" across; and the larger, which had an interior 14" deep and 1.25" across. The smaller possessed a Tuttle cold-cone seal, a cross-section of which is presented in Figure 17. The slightly sharper cone penetrates into the wider cone of the autoclave body, forming a line seal as the threaded cap pushes the two surfaces toward each other. Torque upon the cap is therefore extremely large—the author estimates that it is on the order of 1300 N-m. The larger autoclave style had a Bridgman seal, the cross-section of which is depicted in Figure 18. The latter is known as a self-energizing seal: rather than having a tremendous pressure applied at the outset, as in the cold-cone seal, the fluid in the autoclave acts against a piston and compresses a deformable metal gasket between itself and a hard metal anvil. As the pressure increases, so does the response of gasket, compensating and keeping the

seal intact. Both provided satisfactory pressure retention for, though at some cost: the sealing torque, though not measured, was on whatever a man could achieve with the help of a six-foot long, three-inch diameter steel pipe.

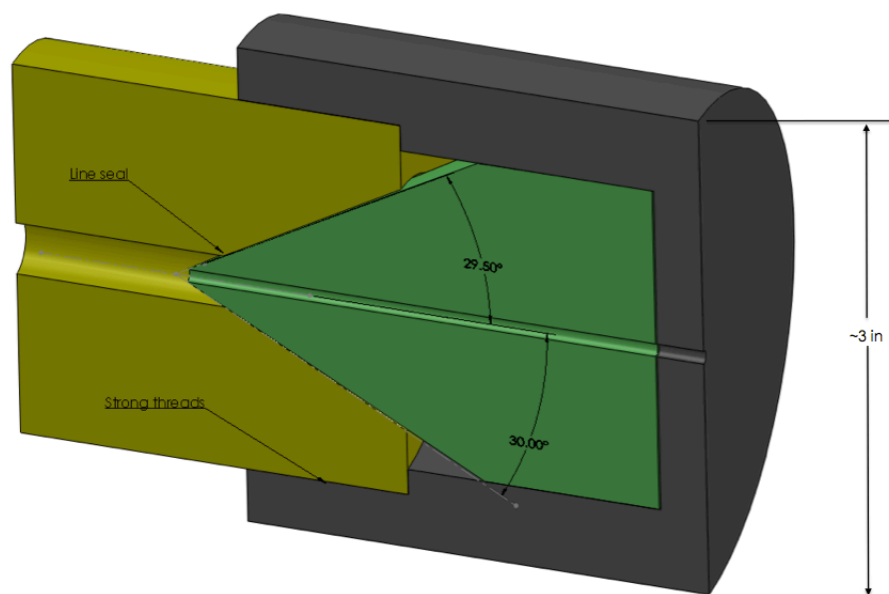


Figure 17. A section view depicting the form of the Tuttle cold-cone seal, in its three parts. In the middle is the cone itself, machined to a half-angle of 29.5° . The autoclave body—the left-most component—has a conical seat machined to a 30° half-angle, in to which the cone fits. Owing to the slight difference in angles, however, they only touch at a circular locus, forming a line seal. Assembly is clamped together by the retaining cap via the screw threads indicated. The channel leading through the cone and cap are provided for the addition of a pressure gage and burst disk assembly.

As the research progressed, the lab acquired a number of modified Bridgman (MB) seal autoclaves of interior dimensions 32 mm dia and ≈ 319 mm depth, for a working volume of 250 cm^3 [82]. Though the sealing principle is the same for the original and MB style, the latter benefits from material improvements. As a result, is a much easier type of seal to work with: the system can be assembled with small torsion bar and an Allen wrench.

The size and number of band heaters depended on the particular autoclave and the goals of the experiment. These were held at temperature using Omega CN-3251 temperature controllers that received their inputs from thermocouples clamped

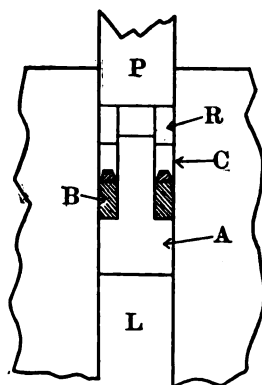


Figure 18. This is the Bridgman seal as Dr. Bridgman originally published it, in 1914. In operation, the pre-loaded piston P acts on the hardened steel ring R, which in turn presses against the cupped washer C, made of soft steel. This piece mates to the rubber gasket B. The plug, A, is in direct contact with the working medium contained in the cavity L, and has a stem the passes up and into R, but not all the way through: there is a gap between P and A. Therefore, as the pressure in L increases, the piston acts against the rubber gasket. As the force on the piston, in equilibrium, must balance, and the area in contact with B is less than that in contact with L, so must the pressure in B be greater than the pressure in L, forming a reliable seal. Setting the piston, in this model, was as difficult for Bridgman as for the author: “in my early work... the piston was driven by a screw. The screw had a pitch of 8 threads to the inch, and needed a six foot wrench to turn it.” [81]

between the band-heaters and the autoclave body.

The final sub-assembly were the ampules themselves. These began as precious metal tubing, either open at both ends, or with a flat bottom on one side affixed at the factory. In either case, to seal an open end, the author first clamped down the tube to bring the surfaces in contact. For 1/4” tubing, it was sufficient to use a standard machinist’s vise to compress the ends, and then fold over the edges to keep the maximum dimension small enough to enter the autoclave. For the larger tubes, the ends were bent into a quatrefoil pattern using a four-jaw chuck. TIG welding completed the hermetic seal. There were two subtleties of note when working the final seal, however. First, rather than adding the solution and then performing all the welds, ridges of the pattern were sealed, along with the center, before the mineralizer was added via syringe. Second, the mineralizer was frozen in the tube by the use of liquid nitrogen. If possible, the tube remained partially submerged in

the cryogen during the welding process. Both of these additions were instituted to reduce the amount of vapor pressure built up in the tube, and commensurate danger to the worker.

When assembling the system, the ampules were inserted into the autoclaves of matched diameter, followed by deionized water to provide counter-pressure. That the tubes should very nearly fill the system improved the thermal transfer from the autoclave body to the ampule, and left less room for the counter-fill water to circulate and average out the internal temperature. The presence of the water was necessary to prevent the tube from expanding and establishing a friction fit within the tube; in cases where this expansion occurred, extraction was effectively impossible without destroying the tube and samples contained within. As a practical matter, a volume of water corresponding to 65% to 85% of the volume unoccupied by the tube was generally sufficient to contain the tube without extreme deformation of the ampule.

3.2 Hydrothermal Growth Experiments

3.2.1 Phase Studies

In order to conduct phase studies, samples of the feed stock and mineralizer solution were added to small precious metal tubes of 0.25" outer diameter and 3" length. The reaction ampules contained between 97.0 mg and 103.0 mg of the $\text{Li}_2\text{B}_4\text{O}_7$ powder and 0.4 mL of the 10^{-6} M LiOH as the mineralizer. The bottom was held at 25°C hotter than the region in order to provide a precipitation region within the ampule. After three days, the autoclave was removed from the band heaters and insulation while at working temperature and cooled with flowing water, then opened. This procedure required significant preparation for efficiency and safety, but that done, was always accomplished in less than 15 minutes.

3.2.2 Spontaneous Nucleation

It remains an unfortunate conjunction that, first, crystal samples are necessary to characterize their thermodynamic properties, and second, the unavailability of these crystals is frequently what motivates the research in the first place. Fortunately, as crystals are a low-energy arrangement of their constituent chemistry, it can be favorable for them to form spontaneously out of solution, and subsequently grow (c.f. theory section).

The spontaneous nucleation growth of lithium borates utilized the work the work of McMillen *et al.* as a starting point [78]. $\text{Li}_2\text{B}_4\text{O}_7$ powder (99.995%, metals basis, Alfa Aesar) served as the feed material and 10^{-6} M LiOH as the mineralizer solution; the ampule was 6" long and of $\frac{3}{4}$ " outer diameter. The mineralizer was made immediately preceding its use by dissolving LiOH powder (high-purity, 99.998%, metals basis, Alfa Aesar) in deionized water to form a 0.1 M solution, and then successively diluted. The ampule was sealed in accordance with the procedure outlined in section 3.1 and placed in a 120 mL autoclave along with an appropriate counter-pressure water fill. Two temperature zones were maintained. Values of 565°C for the lower, dissolution zone and 495°C for the upper, precipitation zone were found to be productive. That is, it provided a sufficient temperature, and therefore solubility, gradient within the tube to generate spontaneous nucleation. Nor was it too large; it is desirable that once a few small crystals have formed that dissolved material preferentially deposits on them, and too large a gradient will cause the precipitation of a great many very small crystals. After the reaction had run for sufficient time and the system cooled, the ampule was removed, cut open, and the reaction products separated with deionized water and a vacuum filtration apparatus.

3.2.3 Solubility Studies

Solubility studies of the various crystal systems proved necessary for the reasons outlined in section 2.2. Their conduct followed the example set by Gelabert *et al.* [31]. Single $\text{Li}_2\text{B}_4\text{O}_7$ crystals were weighed using an Ohaus and loaded into 0.25" outer diameter, 3" long Ag ampules with 0.4 mL of 10^{-6} M LiOH solution. Upon being welded shut, the ampules were loaded into the small Tuttle cold-cone seal autoclaves. Two band heaters were clamped onto the autoclave and held at the same temperature; the size of the heaters would encompass the total length of the ampules to apply isothermal conditions to the samples. It is imperative that the system reach an equilibrium condition for the solubility data to be valid—that is to say, the solution reaches a point of saturation such that dissolved material is precipitating out on to the crystal at the same rate as the crystal is dissolving. At no time does either process stop; the ranges of the reactions are far too small for the average properties of the solution to directly impart themselves, but over the whole volume, the processes precisely compensate each other. Equilibrium, furthermore, is a stable point of the system: it will return to it after perturbation, and remain there. Therefore, in order to give the system sufficient time to achieve this equilibrium state, temperatures were held for 24 hours, after which time they were quenched. The crystals were then re-weighed and the solubility calculated as $\text{wt}\% = \Delta m / (m_{\text{Solution}} + \Delta m)$.

3.2.4 Transport Growth

A transport growth reaction is one application of the hydrothermal growth technique, and the major goal of this research. Each one may run for weeks or even months at a time, increasing their uniqueness and value. That said, they all follow the same basic format: the growth conditions to explore are chosen. Feedstock is

weighed out. A seed crystal is chosen, either of the same species or of one that will impart its crystal structure to the target stoichiometry, and with appropriate discretion as to which crystal plane is shown. This crystal is bored to admit a thin precious-metal wire, and it is mounted upon a support ladder made of the same material above the baffle. A tube is sealed at one end; the feedstock is added carefully, followed by the ladder, after which the top is mostly sealed. The mineralizer solution is made up with equal care, and then added to the tube via syringe, through a gap left for the purpose. The tube seal is completed, after which it goes into the autoclave—gently, to not jar the seed loose—with the counter-pressure fill water, and the autoclave, too, is sealed. Band heaters are attached; insulation is applied; the band heaters are set to increase. To prevent the dissolution of the seed crystal, one brings the bottom band heater up to temperature before the top band heater, to saturate the mineralizer. After remaining at temperature for a protracted period, the system is left to cool, the shells opened, and the growth on the seed crystal examined.

3.3 Characterization

Once the samples of any given procedure had been grown, it became necessary to characterize their crystal habit. As the majority of products were small, clear crystals of similar morphology, more advanced operations than ocular discrimination were at once necessary. By far the most useful characterization technique of this research was Single-Crystal X-ray diffraction (SXRD). (For an exposition of the theory pertaining to the technique, please consult section 2.1.1.2 of this work.) The sheer volume of literature pertaining to the subject, combined with the computerized analysis of the raw data, have turned what was once an exceptionally onerous and demanding procedure into one of nearly rote application.

It should not be surprising that the laboratory in which this work occurred was outfitted with just such an SXRD apparatus: a Rigaku XtaLAB Mini. This enabled what is known as fingerprint analysis, in which a previously identified species might be identified by the revelation of dimensions and angles of a unit cell, without having to solve for any finer structure. It is commensurately faster; generally, 12 scans were taken, with $\phi = 0.0$ and 2θ from -60° to 106° , with a 15° step size and 1° precision. In some cases, particularly when symmetry was reducing the number of observed spots, it was advantageous to take 18 scans with a 9° step. This did not significantly increase the burden for the fingerprint analysis. For more thorough analysis, datasets were taken with $\phi = 0^\circ, 120^\circ$, and 240° , with 2θ from -60° to 120° using a 1° interval. The x-rays were the $\text{MoK}\alpha$ line, providing a resolution of 0.6 \AA . For each reaction, three crystals out of every run were analyzed with SXRD; full crystal structures were solved as necessary.

4. Results and Analysis

This chapter provides details on each experiment performed. Some, particularly those in the phase and solubility studies, have been grouped in one heading due to the repetitious nature of the investigation. Analytical sections will be found both associated with particular experiments and independently in order to address larger syntheses of data. The reader is advised to read this chapter in its entirety, and in the order presented.

4.1 Spontaneous Nucleation

The first reaction attempted was a spontaneous nucleation synthesis, in which 4.03 g of $\text{Li}_2\text{B}_4\text{O}_7$ powder and 16.38mL of 10^{-6} M LiOH mineralizer solution were welded into a silver ampule 6.75" long and of $\frac{3}{4}$ " outer diameter, as discussed in the experimental procedures section. The lower band heater was held at 565°C and the upper at 490°C for 10 days, followed by an uncontrolled cool-down over the course of approximately one day. Once cool enough to handle, the ampule was removed, cut open, and the reaction products flushed from it with deionized water in combination with a vacuum filtration apparatus.

The reaction produced $\text{Li}_2\text{B}_4\text{O}_7$ crystals, as confirmed by repeated sampling and XRD analysis. A full data set was solved with lattice parameters of $a=9.4919(13)\text{\AA}$ and $c=10.3033(21)\text{\AA}$ for hydrothermally grown $\text{Li}_2\text{B}_4\text{O}_7$. These crystals were optically clear and 1-3 mm in their largest dimension, as depicted in Figure 19. Initial indications suggest a positive relationship between solubility and temperature, which was determined by the presence of substantial spontaneous nucleation in the upper colder portion of the silver ampule.

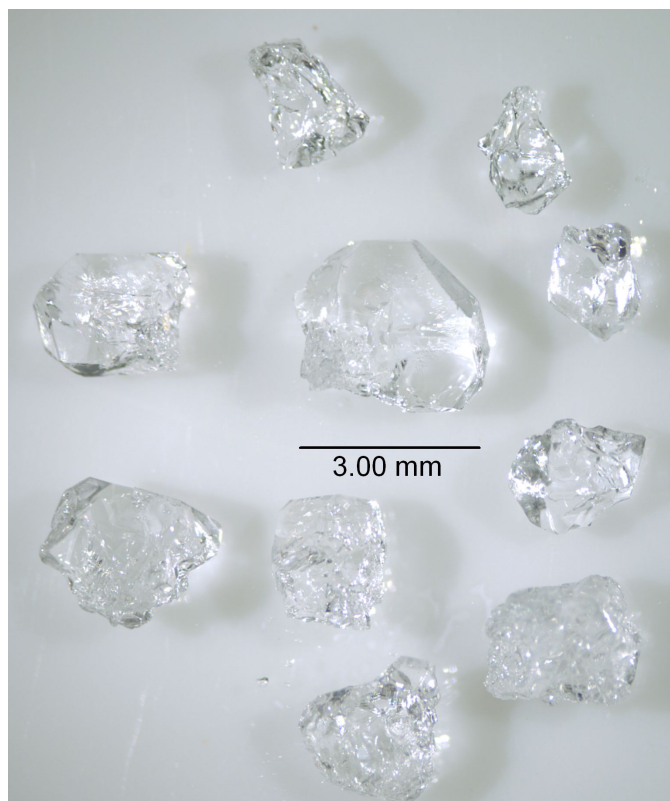


Figure 19. Hydrothermally grown $\text{Li}_2\text{B}_4\text{O}_7$ crystals from the first spontaneous nucleation reaction. These represent the larger end of the product distribution; most of the crystals so grown were significantly smaller than shown here. They are all apparently optically clear. Also noteworthy is the development of faceting on the middle crystal.

4.2 The First Transport Growth Experiment

Following the success of $\text{Li}_2\text{B}_4\text{O}_7$ synthesis in the first SN reaction, the author performed a transport growth reaction using a Czochralski-grown seed crystal and crystalline feedstock from the prior experiment—the latter because practice has shown that crystalline feedstock provides better mineralizer circulation than powdered feedstock and improved crystal growth [34]. The system held a 40°C gradient— 535°C on the lower band heaters and 495°C on the upper—for 8 days, followed by an uncontrolled cool-down. Upon opening the ampule, two crystals were found, one above the baffle and one below, as depicted in Figure 21. The crystals themselves are shown in Figure 20. To our surprise both samples, when

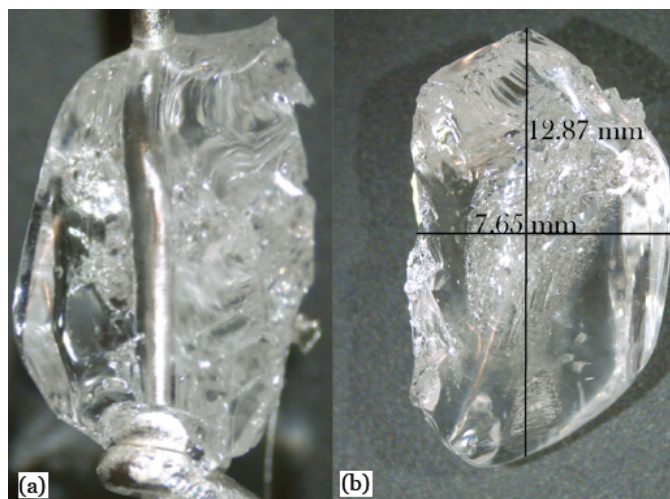


Figure 20. The spontaneously nucleated crystals formed in the first transport growth reaction. (a) Crystal formed above the baffle. (b) Crystal formed below the baffle. Both were γ -LiBO₂ despite having begun with Li₂B₄O₇ seed crystal and feedstock, both of which is presumed to have dissolved entirely early on in the reaction.

characterized by XRD, were determined to be the γ -LiBO₂ phase, not Li₂B₄O₇. The original seed crystal of Li₂B₄O₇ was no longer suspended in the original location, nor was it located in the feedstock. Therefore we assume that it was completely dissolved and served as feedstock for the γ -LiBO₂ crystals. Therefore both samples taken from the tube are assumed to be spontaneously nucleated products. Given the size and duration of the run, the lower bound of the growth rate may be estimated by dividing the major dimensions by the time of the run. This leads to values in the range of 0.95 — 1.6 mm/day, which is comparable that of hydrothermal quartz growth (1.0-1.25 mm/day [60]). Moreover, the fact that a large crystal nucleated below the baffle implies a tremendous change in solubility over a very short temperature range. Subsequent autoclave surface measurements indicate that the temperature difference between the bottom of the tube and the general region of the spontaneous nucleation (that is to say, in the middle of the tube, rather than the intended upper region) was approximately 26°C. As may be observed in the γ -LiBO₂ solubility data from [78], the change in solubility from

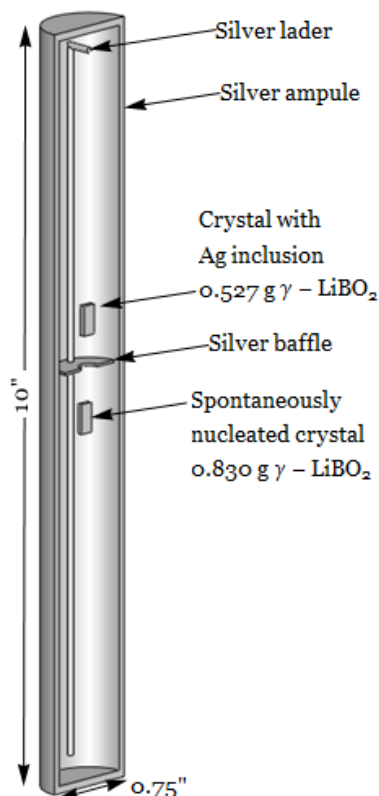


Figure 21. A cut-away of the silver ampule, indicating where the two large crystals retrieved are believed to have formed during the attempted transport growth reaction. The baffle nominally promotes the formation of two thermal zones within the ampule, rather than uninhibited fluid mixing averaging out all temperatures within. Near the baffle itself, where the crystals presumably formed, the temperatures have been estimated by surface measurements to be somewhere in the range of 509°C to 525°C, while the band-heaters themselves were fixed at 535°C and 495°C. Not shown are the counter-pressure water surrounding the ampule, the autoclave, or the band-heaters.

535°C to $\sim 510^\circ\text{C}$ is $\sim \frac{1}{2}\%$, which is sufficient to sustain crystal growth. The similarity in size suggests that the growth rates in the two locations were very similar. It may be that the upper crystal was mass transport limited as compared to the lower crystal, thus remaining slightly smaller. Presumably, had the reaction continued for a significantly greater amount of time, the lower crystal would have dissolved and re-formed on the upper crystal mass.

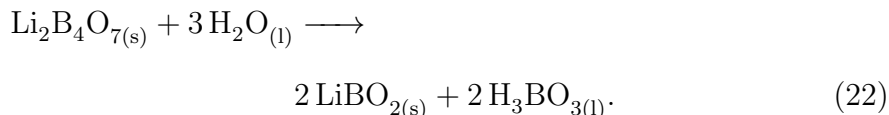
4.3 Second Spontaneous Nucleation

In order to develop more $\text{Li}_2\text{B}_4\text{O}_7$ seed material for further transport growth experiments, the author conducted a second SN reaction. The reaction was held at 565°C for the lower heater and 490°C for the upper, with an uncontrolled cooling rate, as was performed in the initial reaction.

Contrary to expectation, this reaction produced SN crystals of $\gamma\text{-LiBO}_2$ on the scale of 0.1-0.5 mm, as verified by lattice parameters taken from the XRD (c.f. fingerprint analysis, section 3.3). These were optically clear. A key difference between the reactions is that the reaction tube was not shaken after sealing. Upon further consideration, the differences in the two growth runs are explained by the speed at which the feedstock saturated the solution: in the first experiment, the tube, having been thoroughly shaken, provided a large surface area of $\text{Li}_2\text{B}_4\text{O}_7$ powder that would have been more apt to dissolve rapidly. In the second reaction, the author omitted the shaking step, so that the powdered feedstock is likely to have remained relatively compacted at the bottom of the tube, with the mineralizer resting atop it. This would have restricted the area over which dissolution could occur to approximately that of the tube's cross-section. This, we conjecture, would restrict the saturation of the fluid to near-equilibrium conditions, and crystal formation would have been thermodynamic. This would make it subject to different considerations than the kinetic growth (highly supersaturated) of the first reaction, specifically the much lower solubility of $\gamma\text{-LiBO}_2$ evinced in section 4.6. As the constituents of both materials were present, the less soluble phase would have been favored for precipitation.

4.4 A Proposed Explanation

The formation of γ -LiBO₂ in the transport growth reaction, using Li₂B₄O₇ feedstock and seed crystal, and in the second SN reaction, were both unexpected. The apparent difference between the experiments lay in the rate at which Li₂B₄O₇ had been dissolved in the system, which in turn altered the degree of supersaturation in the solution. The temperature gradients in the first SN reaction and the transport growth reaction were not significantly different, but in the former minute particles of Li₂B₄O₇ had been suspended by shaking in the mineralizer fluid, making it very likely to dissolve rapidly and create a solute concentration far greater than saturation from which to precipitate lithium borate species. The transport growth reaction had small (0.1 – 2 mm) pieces of Li₂B₄O₇, yielding a significantly smaller surface area to dissolve; the second SN reaction was similarly limited in the amount of Li₂B₄O₇ that the solution could take up at any given time. Furthermore, the differences in saturation clearly correlate to outcomes: highly supersaturated solution gave rise to Li₂B₄O₇, and the solution closer to equilibrium to γ -LiBO₂. The author therefore proposes that the Li₂B₄O₇ species forms hydrothermally as a kinetic growth process, while γ -LiBO₂ forms as a thermodynamic process, by:



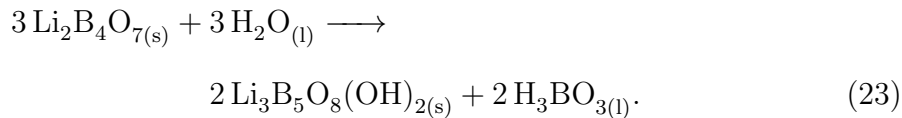
Equation (22) is based on the necessary stoichiometry to account for the initial and product crystals, and combined with the knowledge that H₃BO₃, or boric acid, is soluble and stable in water. Note, also, that this is a net reaction, and intermediate stages may exist, but without additional chemistry in the solution there is no evidence to support them.

Assuming that the hypothesis is true, of course, $\text{Li}_2\text{B}_4\text{O}_7$ would be unsuitable for hydrothermal growth—for reasons to be discussed later—and probably non-ideal for the formation of $\gamma\text{-LiBO}_2$. Equation (22) indicates that during the formation of $\gamma\text{-LiBO}_2$, the working fluid continuously changes its acidity. When operating a long-term growth process that aims for consistent product and quality throughout, this is undesirable [34]. In an attempt to grow $\gamma\text{-LiBO}_2$, should it be desirable, either preliminary feedstock would need to be grown by the conversion of $\text{Li}_2\text{B}_4\text{O}_7$, or stoichiometric quantities of LiOH and H_3BO_3 should be mixed, as done by McMillen *et al.* [78]

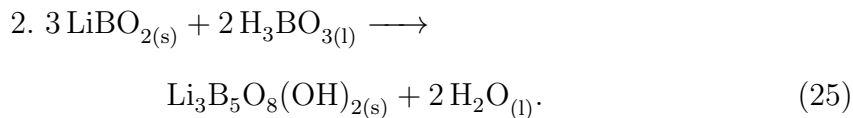
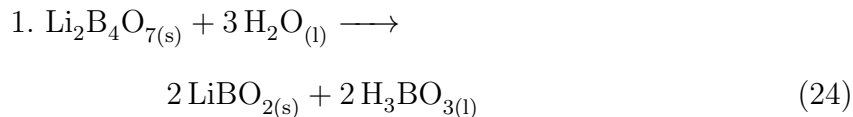
4.5 Phase Study Results

In order to understand the synthesis of $\gamma\text{-LiBO}_2$ as opposed to $\text{Li}_2\text{B}_4\text{O}_7$ under various growth conditions, the author conducted a phase study. Points were taken from 350°C to 550°C, as measured on the bottom band heater, at 50°C intervals. The procedure as laid out in the experimental section took some development, however. Initially, the system heated over the course of an hour and remained at temperature for 3 days, followed by a 24-hour controlled cool-down. These reactions produced $\text{Li}_3\text{B}_5\text{O}_8(\text{OH})_2$ at all temperatures, which did not correspond well to the previous results in which $\gamma\text{-LiBO}_2$ formed rapidly. A review of the literature indicates that $\text{Li}_3\text{B}_5\text{O}_8(\text{OH})_2$ forms hydrothermally at 180°C [79], and moreover that this is a common trend in hydrothermal synthesis of hydrated metal-borate-oxide crystals. $\text{Na}_2\text{B}_5\text{O}_8(\text{OH}) \cdot 2\text{H}_2\text{O}$, for example, grew at 180°C [83]; $\text{Na}_2\text{B}_4\text{O}_5(\text{OH})_4 \cdot 3\text{H}_2\text{O}$ can be grown from aqueous solution at 80°C [84]. It was suspected that, owing to the very high solubility of $\gamma\text{-LiBO}_2$ [36] that an extended cool-down was interfering with the reaction, and for this reason the procedure changed from a controlled cool-down to a quench as described in the experimental

section. The author surmise that the transition to the hydrated phase occurs somewhere in the realm of 200°C. In particular, the author propose two possible mechanisms. The first is direct, and probably occurs in the 180°C regime:



The second possiblity notes the regular formation of γ -LiBO₂ at the higher temperatures, and therefore requires two steps:



These reactions are based upon the species that are known to form within the system, and of course stoichiometric requirements. That said, these reactions occur well below the optimal working temperatures for γ -LiBO₂ or Li₂B₄O₇ growth.

All of the phase study reactions occurred under thermodynamic conditions, as evinced by the amount of Li₂B₄O₇ used as feedstock and the 25°C temperature difference between the band-heaters. Under such conditions, with the experimental procedures discussed, every reaction in the 350°C—550°C range produced γ -LiBO₂ exclusively.

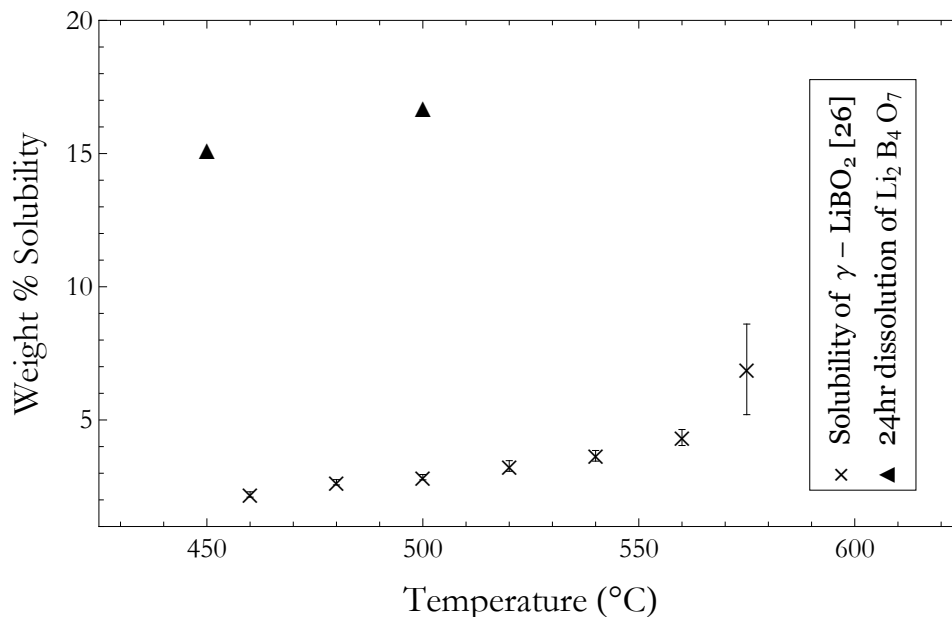


Figure 22. The solubility of γ -LiBO₂ from [78]. The two points depicting the weight percent of Li₂B₄O₇ removed from the two sample crystals by the end of 24 hours are not true solubility points, because the system had not reached equilibrium, and γ -LiBO₂ was spontaneously precipitating from the solution. The point are given only to provide a direct visual comparison between the proportion of Li₂B₄O₇ solvated at a given temperature, and the proportion of γ -LiBO₂ solvated under similar conditions. With this in mind, the figure indicates that Li₂B₄O₇ is significantly less stable under hydrothermal growth conditions than γ -LiBO₂ .

4.6 Solubility Study Results

Christ and Clark observe that boron-oxygen exists either as a triangular (1:3) or tetrahedral (1:4) configuration [54], leading to the conclusion that the building blocks of both crystals must be equally present in the solution created by the dissolution of Li₂B₄O₇—or, put differently, a solution made by dissolving γ -LiBO₂ will not differ significantly from one that started with Li₂B₄O₇. It follows that the lithium borate species which is least soluble under a particular set of thermodynamic growth conditions will be the one that forms. The author therefore undertook a solubility study of Li₂B₄O₇ within the 10⁻⁶ M LiOH mineralizer, according to the experimental procedures outlined previously. Comparative data for γ -LiBO₂ comes from [78], and is shown in Figure 22.

As a point of comparison, Byrappa showed 0.6% $\text{Li}_2\text{B}_4\text{O}_7$ solubility in 1.5 M LiOH at 400°C and 600 bar [35], which is substantially smaller than the values seen in this study. The author believes that this is a result of several orders of magnitude greater lithium concentration already extant in the solution, making the dissolution of $\text{Li}_2\text{B}_4\text{O}_7$ and release of more lithium ions into the fluid thermodynamically undesirable.

Owing to the small size of the SN-produced $\text{Li}_2\text{B}_4\text{O}_7$ crystals, the author used samples cut from a Czochralski-grown sample. Unfortunately, the experiments did not produce true solubility data simply because the system did not reach equilibrium for any reaction condition. At 500°C, the crystal sample began at 110.03 mg, and after 24 hours had shrunk to 30.04mg; the test at 450°C utilized a 71.23mg crystal sample which dissolved entirely. Using the formula from the procedures section, these would correspond to solubilities of 16.7% and 15.1%. That said, it is evident that the 500°C sample was still in the process of dissolving when the reaction stopped, as it retained signs of continued dissolution as depicted in Figure 23. Moreover, both reactions produced a fine crystalline cluster of the $\gamma\text{-LiBO}_2$ —a fact which would have dramatically increased the apparent solubility of $\text{Li}_2\text{B}_4\text{O}_7$ in the solution, and which undermines any assumption of achieving the equilibrium condition needed for a true solubility measurement. For this reason, no formal solubility points are presented. Nonetheless, $\gamma\text{-LiBO}_2$ appears to be distinctly less soluble in the weak LiOH solution used, and will be formed preferentially under thermodynamic conditions.

It follows immediately that $\text{Li}_2\text{B}_4\text{O}_7$ is a metastable state with respect to the hydrothermal growth system under consideration. In a thermodynamic growth condition, there is enough thermodynamic potential to release this metastable state, but not enough to reform it. Increasing said potential is contradictory to the growth

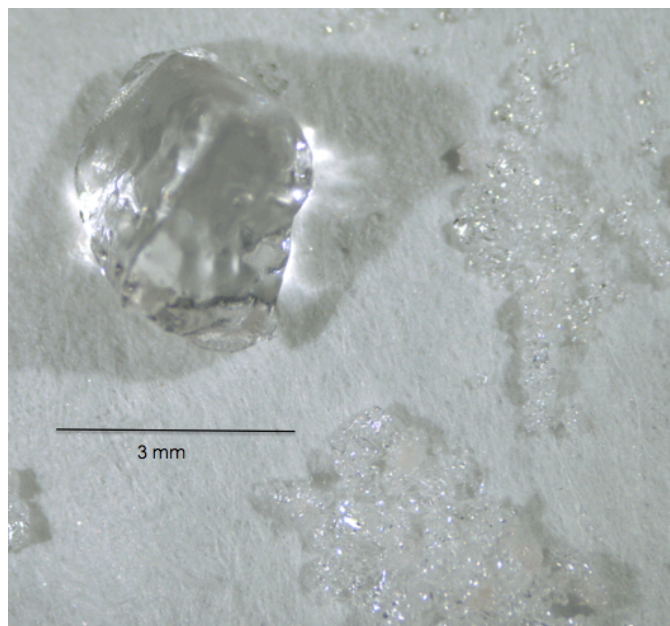


Figure 23. The material shown came from the 500°C experiment after 24 hours at temperature. The large, un-faceted mass in the upper left is what remains of the original $\text{Li}_2\text{B}_4\text{O}_7$ sample, having lost 79.99mg, or 72.7% of its original weight. The small, spontaneously nucleated crystals surrounding it in the rest of the picture has been confirmed as $\gamma\text{-LiBO}_2$ via XRD, having apparently formed even without a thermal gradient.

of good crystals—as discussed in the section on theory, minimization of the working enthalpy is a key advantage of the hydrothermal growth technique, and to increase it is to increase the number of thermally-induced defects within the system. It follows that $\text{Li}_2\text{B}_4\text{O}_7$ is not a suitable material for hydrothermal growth.

4.7 Kinetic Growth

The remaining aspect of research was to confirm that $\text{Li}_2\text{B}_4\text{O}_7$ does form when the growth conditions are kinetic. Therefore, the author conducted a third SN reaction that was deliberately driven to kinetic crystal growth conditions by means of a 100°C temperature gradient. 10.89 g of $\text{Li}_2\text{B}_4\text{O}_7$ and 44.47 mL of the LiOH mineralizer solution were sealed in a 12" long, $\frac{7}{8}$ " outer diameter silver tube. As in the first spontaneous nucleation reaction, the tube was shaken to ensure

pervasive commingling of mineralizer with the feedstock and to provide thereby ample surface area for dissolution. This was placed in a modified-Bridgman seal autoclave of 250 mL inner volume, along with a suitable counter-pressure fill of deionized water, and heated with two pairs of band heaters to 465°C and 565°C in the upper and lower regions. The system remained at temperature for nine days, at the end of which power was removed and the system allowed to cool uncontrolled. The reaction products were crystals of $\text{Li}_2\text{B}_4\text{O}_7$ as confirmed by XRD, smaller than those formed in the first SN reaction. This is not surprising: the conditions would have favored the formation of a larger number of competing nucleation points. This result does corroborate that the system achieved a kinetic growth condition. Furthermore, given the apparently exclusive presence of $\text{Li}_2\text{B}_4\text{O}_7$ in this reaction, its creation appears to be favored under kinetic growth conditions.

4.8 Lithium Metaborate Growth

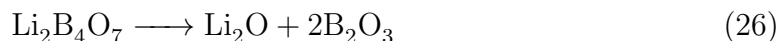
As $\gamma\text{-LiBO}_2$ showed great potential for hydrothermal growth, the author also attempted a transport growth reaction in this system. After conducting a spontaneous nucleation reaction to convert $\text{Li}_2\text{B}_4\text{O}_7$ powder to $\gamma\text{-LiBO}_2$ crystal feedstock, the author mounted two seed crystals on a silver ladder. One came from the first transport growth reaction, and weighed 0.8027 g; the other was a small but sufficient crystal from the immediately preceding SN reaction, weighing 0.0502 g. These, with 7.728 g of $\gamma\text{-LiBO}_2$ feedstock crystals were added to a silver tube 3/4" in diameter and 9" long. Then, after the preliminary welding, 29 mL of 10^{-6} M LiOH. The upper (cooler) band-heater was 505°C and the lower 535°C, which were brought to temperature over the course of 24 and 12 hours, respectively, in order to partially protect the seed crystals from premature dissolution.

The reaction was allowed to persist for ten days, during which the autoclave developed a slow leak and dropped from a peak of 20 kpsi to 10 kpsi, but which is not supposed to have had profound consequences on the reaction, as the tube showed neither compression nor expansion. After the reaction period had elapsed, the author cut the power and allowed the system to cool uncontrolled. The day after deactivation, the ampule was removed from the autoclave and opened.

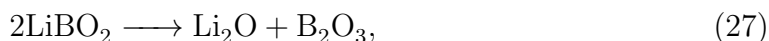
The seed crystals dissolved entirely. All the feedstock material became a fine powder of γ -LiBO₂, of smaller size than the original feedstock. Little to no spontaneous nucleation appeared to have occurred on the upper surfaces of the ladder.

Recall that in all other reactions the feedstock was Li₂B₄O₇ and not γ -LiBO₂. The phase and solubility studies indicate that γ -LiBO₂ is thermodynamically preferable to Li₂B₄O₇ under the hydrothermal conditions of this study, and that Li₂B₄O₇ can supersaturate a 10⁻⁶ M LiOH solution with respect to γ -LiBO₂ before it has completely dissolved itself. That is to say, Li₂B₄O₇ appears to dissolve more rapidly than γ -LiBO₂.

There are a number of arguments beyond these experimental results to show that Li₂B₄O₇ dissolves more quickly than γ -LiBO₂. In [85], Velez *et al.* showed that in 30°C water the outward flux of material was dependent upon the B₂O₃—Li₂O ratio within lithium borate glasses, with dissolution rate increasing with the proportion of boron. Figure 24 shows how sensitive this dependence can be at high B₂O₃ proportions. Decomposing both the Li₂B₄O₇ and γ -LiBO₂ formulae, one finds



and



respectively. Admittedly, a glass has no long-range order; the dissolution cannot be associated with a specific arrangement of the material. Therefore, though the γ -LiBO₂ and Li₂B₄O₇ samples in this study were crystalline and not glasses, the material composition still supports a notion that the greater the proportion of boron within the crystal, the faster it would dissolve. The tetraborate has the greater proportion of B₂O₃, and is thus predicted to dissolve faster.

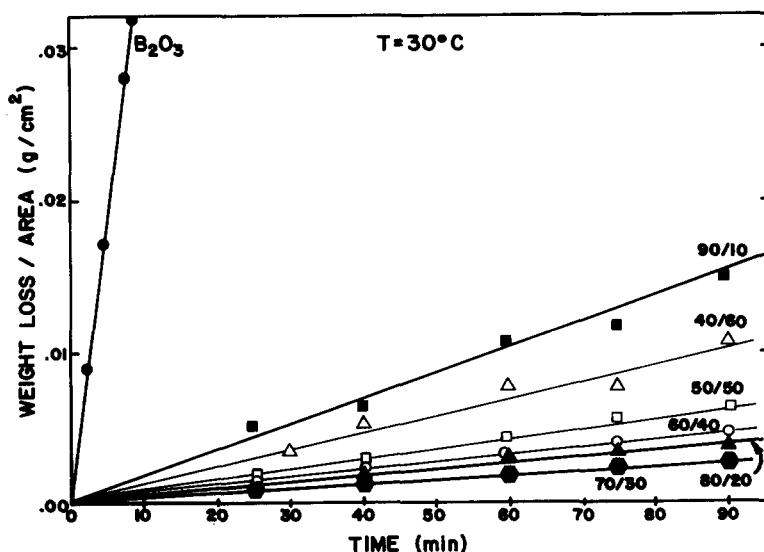


Figure 24. This plot shows the time-dependent weight-loss of various B₂O₃-Li₂O glasses, from [85]. It follows that the slopes of the fitted lines are the average rates of dissolution, and that those glasses with more B₂O₃ dissolve faster than those with less. Pure B₂O₃, in particular, dissolves tremendously quickly.

Lithium tetraborate dissolving faster than lithium γ -metaborate is also favorable from a geometric standpoint. Consider their respective crystal structures, shown in Figures 25, 26, and 27. In the tetraborate, the unit cells are linked together by trigonal planar BO₃ formations, shown as the triangles with spheres at their center. Contrast this to the metaborate, in which the structure is formed of interlocking BO₄ tetrahedrons, forming continuous columns through the volume of the material. In either case the boron-oxygen bonding is likely very important to the structure itself; purely geometric considerations would coordinate three oxygens to one boron

(c.f. [29]), but tetrahedrons form. This suggests that covalent bonding and sp^3 hybridization dominate the formation of the lattice and prevent a tighter structure from forming. Taken one step further, assuming all B–O bonds are of equal length, the minimum distance (that is to say, edge length) between two oxygens in a tetrahedron will be closer together than two oxygens in a plane. Both tetraborate and metaborate have tetrahedrally coordinated boron; trigonal planar coordination occurs only in $\text{Li}_2\text{B}_4\text{O}_7$. It thus appears that the γ -metaborate is more tightly held together than the tetraborate, and so dissolves less readily. This may be corroborated by examining the particular arrangement of the units within the crystal, as in Figure 28 for $\text{Li}_2\text{B}_4\text{O}_7$ and Figure 29 for $\gamma\text{-LiBO}_2$.

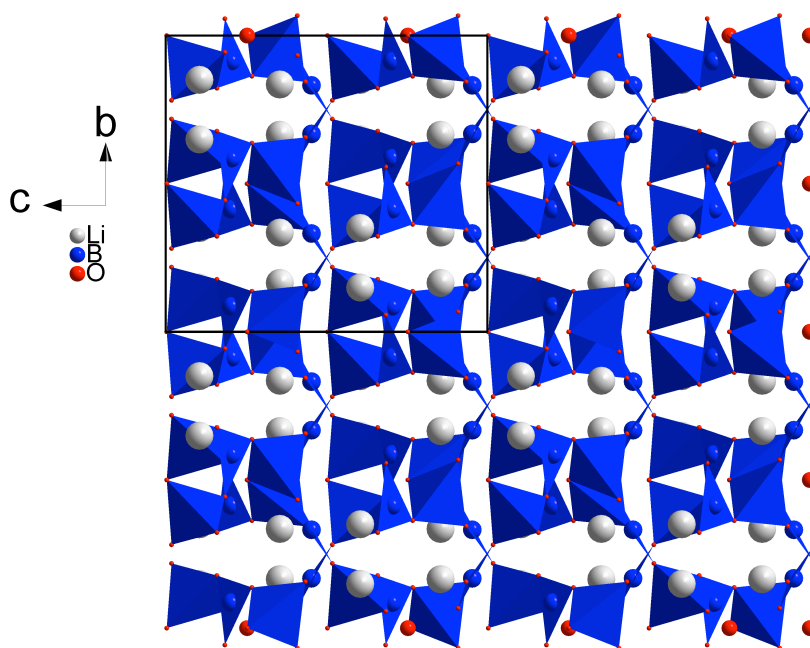


Figure 25. This shows a segment of crystal lattice as found within $\text{Li}_2\text{B}_4\text{O}_7$, comprised of eight unit cells, in parallel plane projection along the a -axis. A single unit cell is delimited by the black box in the upper left hand corner. Each tetrahedron has a boron atom at its center; they are introduced to show the orientation of the tetrahedrally coordinated BO_4 structures within the cell. Likewise, the blue triangles show how trigonal planar structures, BO_3 participate in tying the lattice together.

In the tetraborate, pairs of tetrahedrally coordinated borons are linked via the

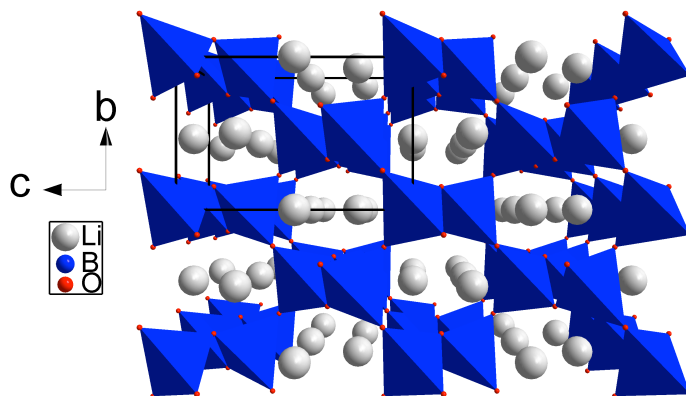


Figure 26. In contrast to $\text{Li}_2\text{B}_4\text{O}_7$, $\gamma\text{-LiBO}_2$ has only tetrahedrally coordinated boron atoms. The figure shows their arrangement in an eight unit-cell crystal, with an individual unit cell delimited by the black box in the upper left.

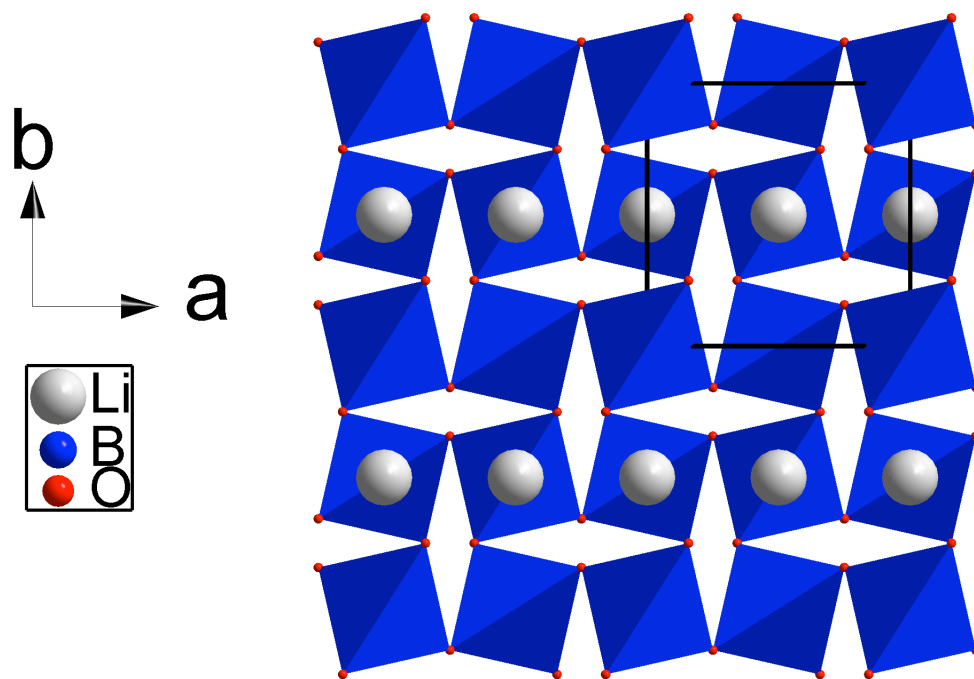


Figure 27. The columnar structure of metaborate may be found in all directions.

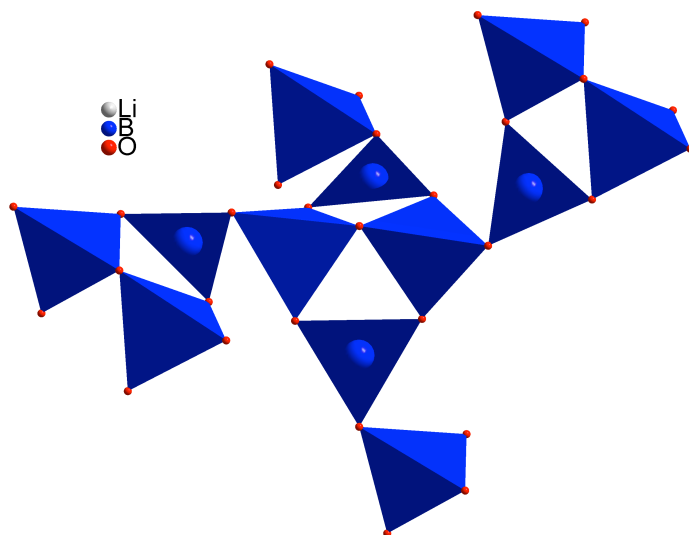


Figure 28. This segment of $\text{Li}_2\text{B}_4\text{O}_7$ shows how the boron complexes interlink with each other. Tetrahedrons are paired off and held at their particular angle by the triply-coordinated boron, which link each pair of tetrahedral units. This corresponds well to what was shown in Figure 25, where the connections in the plane normal to the c-axis were effected by these trigonal planar bridges.

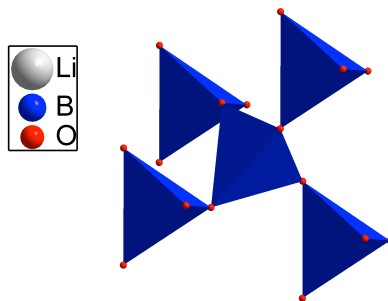


Figure 29. Every tetrahedron is closely linked to four others by means of an oxygen, limiting the space and freedom for a boron complex to be attacked by the surrounding fluid.

trigonal planar boron complexes. If these groups were to break off into solution, then only the tetrahedrons—building-blocks of the metaborate—would remain. Enter the notion of steric hinderance: the arrangement of atoms about a particular group or component of a molecule changes its ability to interact with its surroundings [65]. Inspection of the crystal structures in the figures suggests that there is simply more area for water to insinuate itself around the trigonal planar structures in lithium tetraborate and pull them into solution, than around the tetrahedrons in lithium metaborate. Using the atomic radius data found in Table 2.4 of [29] and the lattice parameters calculated while solving the crystal structures, it can be shown that $APF_{\text{LiBO}_2} = 0.798$ and $APF_{\text{Li}_2\text{B}_4\text{O}_7} = 0.682$. The tetraborate structure really is more open than that of the metaborate. This further supports the notion of more rapid dissolution of $\text{Li}_2\text{B}_4\text{O}_7$ than $\gamma\text{-LiBO}_2$.

A last consideration: BO_3 , the conjugate base of HBO_3 , is more soluble in water than B_2O_4 —0.276 g/mL versus 0.157 g/mL at 100°C [66]. BO_4 is not mentioned in the literature. It follows that the BO_3 groups that can dissociate from the lithium borate crystals are suited to remain in solution, while the tetrahedral boron groups are not. One may reasonably hypothesize that even if a tetrahedral group is broken off from the crystal lattice, it may simply reattach to the crystal surface without noticeable participation in the solution, manifesting as a lower dissolution rate for the tetrahedrons.

It also appears that the metaborate reforms faster than it dissolves. In the reaction, larger metaborate feedstock crystals dissolved and stabilized as a smaller crystals. This indicates that in order to provide an equilibrium between dissolution and precipitation, the surface area of the material had to increase, implying that the rate of reformation is greater than the rate of dissolution.

Let the majuscule \mathfrak{R}_x be the rate of dissolution indicated by x , and likewise \mathfrak{r}_x

the rate of formation. x takes becomes t for the tetraborate, and m for the metaborate. Thus far it appears $\mathfrak{R}_t > \mathfrak{r}_m$, $\mathfrak{r}_m > \mathfrak{R}_m$, and $\mathfrak{R}_t > \mathfrak{R}_m$. Though the last relation follows from transitivity, it also corresponds to the transformation of tetraborate into metaborate during the solubility studies.

The reverse of equations (27) and (27) translate to the rate equations are [65,86]:

$$\mathfrak{r}_t = \frac{d[\text{Li}_2\text{B}_4\text{O}_7]}{dt} = -\frac{d[\text{Li}_2\text{O}]}{dt} = -\frac{1}{2} \frac{d[\text{B}_2\text{O}_3]}{dt}, \quad (28)$$

$$\mathfrak{r}_m = \frac{1}{2} \frac{d[\text{LiBO}_2]}{dt} = -\frac{d[\text{Li}_2\text{O}]}{dt} = -\frac{d[\text{B}_2\text{O}_3]}{dt}. \quad (29)$$

There is no obvious relationship between \mathfrak{r}_t and \mathfrak{r}_m from the experimental evidence. That said, $\text{Li}_2\text{B}_4\text{O}_7$ formed under kinetic conditions, designed to force material out of the system at a great rate. Therefore it is likely that

$$|(\frac{d[\text{B}_2\text{O}_3]}{dt})_t| > |(\frac{d[\text{B}_2\text{O}_3]}{dt})_m| \quad (30)$$

$$-(\frac{d[\text{B}_2\text{O}_3]}{dt})_t < -(\frac{d[\text{B}_2\text{O}_3]}{dt})_m = \mathfrak{r}_m, \quad (31)$$

$$2\mathfrak{r}_t = -(\frac{d[\text{B}_2\text{O}_3]}{dt})_t < -(\frac{d[\text{B}_2\text{O}_3]}{dt})_m = \mathfrak{r}_m \quad (32)$$

$$\mathfrak{r}_t < \frac{1}{2}\mathfrak{r}_m. \quad (33)$$

Which is to say, the thermodynamically favored species has a higher rate of formation than the other. This is not altogether surprising; minimum potential energy offers the greatest driving “force” to the system, by analogy to $F = -\nabla U$.

One other point that is very helpful in understanding the results: recall that in the first transport growth reaction, a large spontaneously nucleated γ - LiBO_2 crystal formed below the baffle. This corresponded to a temperature gradient of about 10°C . Recalling McMillen’s LiBO_2 solubility data (Figure 22), the solubility difference between 535°C and 505°C is approximately 1%—a modest growth rate,

below the 2-5% requirement of [61]. From the discussion above, posit that a material that is structurally disinclined to break apart is likewise structurally inclined to re-form, so that the amount of time taken to transition through the baffle was larger than that require to form nucleated products. That is to say, even though the supersaturation was not exceptional, the kinetic favorability of precipitation was such as to prevent the dissolved feedstock from getting to the upper region.

Thus, the sequence events that took place in the second transport reaction might read as follows. First, the bottom band-heater started coming to temperature while the upper heater remained cool, creating a substantial temperature difference between the bottom of the tube and the region just below the baffle. This would have created a micro-transport growth zone, in which the large feed-stock could begin to spontaneously nucleate a smaller crystal size. Without the tetraborate supersaturating the solution, all the metaborate dissolved at the bottom precipitated out as it was formed, and so did not make it up to the seed crystal region. The seed crystal, absent the saturated solution, itself dissolved and its feed material sank to the bottom, becoming generally incorporated in the lower section's convection. Then, after some time, the solution reached an equilibrium, where the surface area of the powder and corresponding rate of dissolution was equivalent to the rate of precipitation in the region just below the baffle—a much smaller powder than the beginning, all in the bottom of the tube.

5. Conclusions

This work attempted to identify the optimal hydrothermal growth conditions for $\text{Li}_2\text{B}_4\text{O}_7$ with a weak LiOH mineralizer solution. The data, however, indicate that such conditions do not exist. Though true solubility data for $\text{Li}_2\text{B}_4\text{O}_7$ in this 10^{-6} M LiOH does not exist, the secondary evidence indicates that it is extremely soluble, and moreover unstable with respect to $\gamma\text{-LiBO}_2$. The phase study further indicates that $\gamma\text{-LiBO}_2$ is the favored species of growth for high-temperature LiOH solvent solutions, with a transition to hydrated phases at lower temperatures.

$\text{Li}_2\text{B}_4\text{O}_7$ occurred only when the chemical potential to form a crystal was sufficient to place the system in a state of kinetic, rather than thermodynamic, growth. From this, it appears that $\gamma\text{-LiBO}_2$ forms from weak LiOH solution under thermodynamic conditions, and $\text{Li}_2\text{B}_4\text{O}_7$ grows only when the growth mechanism is kinetic.

Therefore, $\text{Li}_2\text{B}_4\text{O}_7$ is not a suitable material for large, high-quality hydrothermal growth when using weak LiOH solutions. It is possible that adding boric acid (H_3BO_3) to the solution would make the formation of $\gamma\text{-LiBO}_2$ sufficiently unfavorable, in accordance with equation 23, that $\text{Li}_2\text{B}_4\text{O}_7$ would form, but the possibility has not been explored to date.

The prospect of quickly and efficiently growing $\gamma\text{-LiBO}_2$ compelled a transport growth experiment. Unfortunately, the seed crystals dissolved completely and the feedstock recrystallized as smaller material. Foremost, its results suggest that $\gamma\text{-LiBO}_2$ is kinetically more favorable to form than to dissolve, as it appears to have achieved dissolution–precipitation equilibrium with a very large surface area—very small crystals. This interpretation also suggests that a more open baffle—or no baffle at all—may be optimal for $\gamma\text{-LiBO}_2$ growth in 10^{-6} M LiOH solution, as small temperature gradients and large flow rates appear to be necessary. Over-all, the general relations between the reaction rates of formation and dissolution appear to

be: $\mathfrak{R}_t > \mathfrak{r}_m$, $\mathfrak{r}_m > \mathfrak{R}_m$, $\mathfrak{R}_t > \mathfrak{R}_m$, and $\mathfrak{r}_t < \frac{1}{2}\mathfrak{r}_m$, though a thorough quantitative study is in order to confirm these ideas.

5.1 Future Work

In a the more minor concerns, there is polishing that might be done to fill in some of the lacunae imposed by the closed nature of the technique. For instance, should it prove valuable, some work might be done to validate the proposition of the reaction converting tetraborate into metaborate, (22). Such evidence could be found by measuring the pH of the working fluid after the completion of the reaction; during the original experiments, its retention was not thought to be particularly important. It does indicate, however, that a more thorough exploration of the thermodynamics of the system are necessary. In particular, are there temperature regimes within the starting chemistry wherein γ -LiBO₂ is stable, and others where Li₂B₄O₇ is preferable? What are the relative solubilities of Li₂B₄O₇ and γ -LiBO₂ at various temperatures within the system? Answering these questions will, in turn, allow the assessment of this hypothesis.

Focusing on the big picture, however, the target remains the growth of crystals for neutron detection. Though Li₂B₄O₇ is no-longer considered viable for hydrothermal growth, it does appear that γ -LiBO₂ would be a viable replacement. Its density of the requisite chemical species is satisfactory to replace Li₂B₄O₇, and the evidence thus far indicates that it may grow rapidly enough to be economically viable under the hydrothermal growth technique. More research is necessary for the development of the material in this vein. Foremost in this would appear to be the satisfactory transport growth of γ -LiBO₂, which the author attempted. In this, steps should be taken to protect the seed to a greater degree than what was done in

this work. Once a mechanism for ensuring successful growth has been found, then it becomes a matter of optimizing the growth itself.

In conjunction, work must be done to create γ -LiBO₂ as a suitable neutron detector material, specifically by doping it. As envisioned by the author, γ -metaborate could be substitutionally doped with phosphate anions in place of the BO₄ tetrahedrons constituting the γ -LiBO₂ lattice. The practicality of this proposition depends in part on the degree of size mismatch between the phosphate and the borate tetrahedron it is intended to replace: the phosphate group, being larger than the borate, will have to squeeze in to the allowed space, creating local strain within the lattice. This strain also represents an increase in lattice energy, just as work is done to compress a spring. The difference is not excessive, however. Using the ionic radii for four-fold coordinated atoms from [29], and considering the oxygen nuclei to be vertices, the circumsphere radii for BO₄ and PO₄ are 1.5 Å and 1.71 Å, respectively, or a 14% size mismatch—c.f. Figure 30. For comparison, the Cu-Be system has a 10.9% difference and 16.4% solid solubility [28], and [29] notes that less than 15% mismatch is regarded as favorable for forming solid solutions. Therefore reasonable incorporation of phosphorus into γ -LiBO₂ may be expected on size grounds.

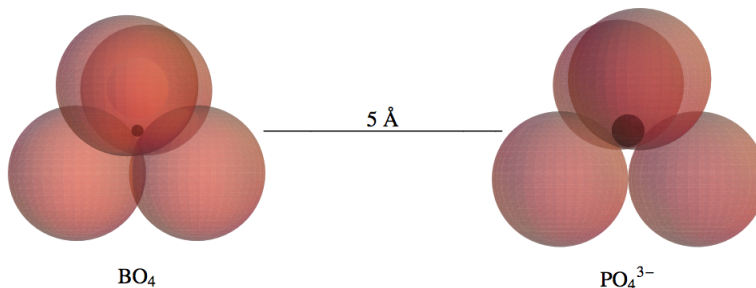


Figure 30. This is a scale drawing of PO_4^{3-} and a BO_4 tetrahedron found in γ -LiBO₂, as approximated using the hard sphere model. The translucent red spheres represent the oxygen atoms, while the dark interior spheres are boron and phosphorous, respectively. To the eye, at least, the difference in size is minimal.

Electronegativity is also a quantity of importance in creating solid solutions [28]. Boron is valued at 2.04 on the Pauling scale, and phosphorous 2.19, a difference of 7.4% [65]. Of course, [29] also remarks that “for oxides this restriction is usually implicit in factors of ion valency and size.” Size has been dispensed with; the valences are the same (sp^3). The last concern would be that of equivalent structure type, but this is irrelevant when the goal is only to dope a crystal: therefore, there is no indication against the use of phosphate as a dopant in γ -LiBO₂.

Such work cannot be done without considering the effect on the over-all growth process; the dopant must be incorporated into the feedstock at the beginning of the reaction, and its effect on the chemistry of the reaction taken into account. In this regard, it might be useful to create, kinetically, phosphate-doped lithium tetraborate for use as feed material for growing lithium γ -metaborate, in order to provide equivalent dissolution of feed and dopant into the solution. It is also possible that tetraborate will incorporate phosphate more easily, as illustrated in the following figures.

Figure 31 is a schematized diagram of the metaborate lattice, insofar as every tetrahedron in its lattice is linked at four points to another tetrahedron, hence the diamonds. The larger phosphate would require the compression and torsion of various of these bonds, leading to a higher energy state in that region of the crystal, much like compressed springs. As the radius expands, the effect is damped out. Figure 32 is a cartoon of Figure 28, to provide a point of comparison for 33, which shows how a phosphate might incorporate to the system. In particular, the one and two point bondings of the BO₃ groups are conjectured to act like hinges, as depicted in 33. This does neglect the space-filling nature of the electron clouds, and the resistance they may provide toward bending; nonetheless, this geometrically-based heuristic suggests that Li₂B₄O₇ will accept the dopant more easily than γ -LiBO₂.

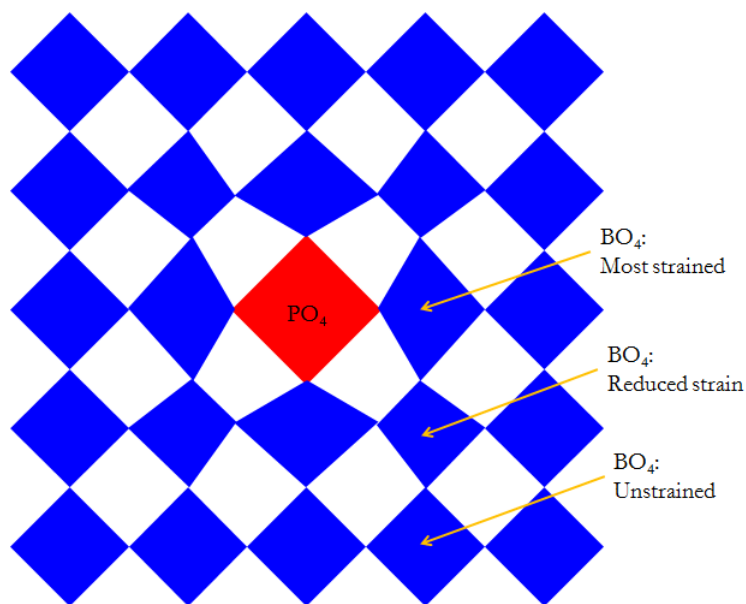


Figure 31. This is a cartoon of the effect phosphate inclusion would be expected to impart on the local boron-oxygen lattice in lithium γ -metaborate. Each blue square represents a BO_4 tetrahedron, with each corner standing in for a vertex, and each locked to four other squares, as the tetrahedrons are in $\gamma\text{-LiBO}_2$. Incorporation of the phosphate structure necessarily requires the deformation of the lattice, the strain of which constitutes a potential which would prefer to be released.

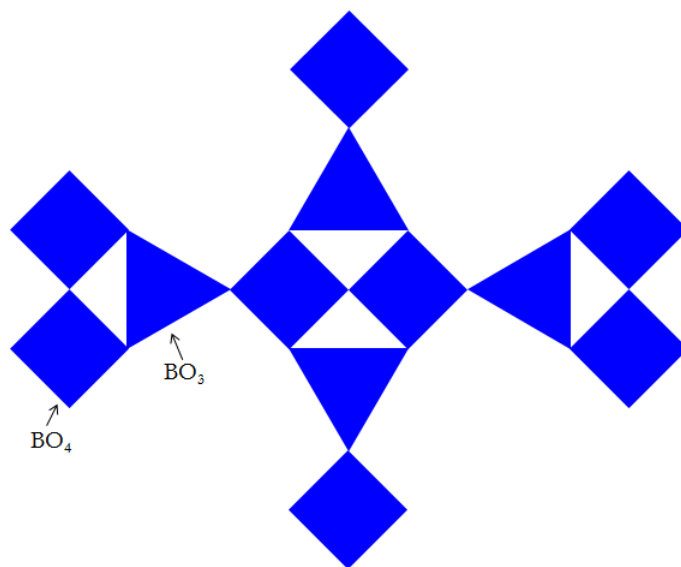


Figure 32. This is a two-dimensional schematic of the boron-oxygen lattice found in lithium tetraborate, c.f. Figure 28

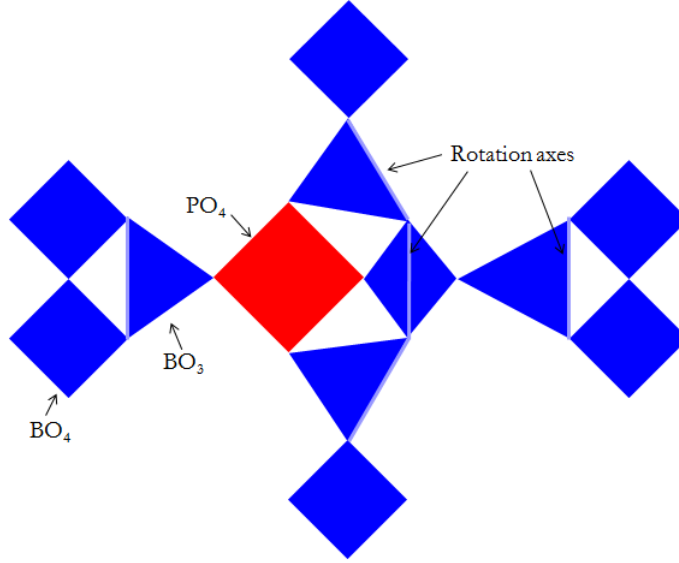
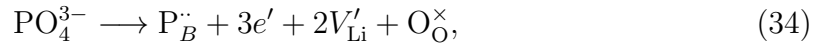


Figure 33. This cartoon continues what was shown in Figure 32 by incorporating a phosphate group—not to scale, but larger. Owing to the lack of close interconnection within the lattice, as was depicted within the metaborate, the author conjectures that the lattice may be more able to bend and accommodate the PO_4 dopant.

Beyond straining the lattice, incorporation of the P^{5+} where there had previously been B^{3+} will affect the local charge balance of the crystal. Phosphate also carries three extra electrons that must be incorporated into the lattice—rather the point as a dopant—and which must be accounted for electrically. The oxygens end up on oxygen sites, with the same oxidation state, but are included for completeness. Then the reaction may go as



showing that each phosphate incorporated may be expected to drive two lithium ions from the lattice. This is not likely to be a problem from either a structural or neutron detection standpoint: in the former, the covalent lattice of oxygen and boron should maintain solidity; in the latter, electrical dopant concentrations are frequently less than one part in ten thousand [28]. Even with a factor of two for the

generation of flaws, the number of lithium vacancies generated will be negligible. More to the point, the macroscopic cross-section of the material will remain large.

Of course, if phosphorus does not play out as a dopant for the lattice, there are still other elements that may work. Hafnium has been suggested [7], and has been used as a component for other solid-state neutron detector explorations [87]. This is, regarding lithium-borate-oxides, speculative, but possibly worth exploring.

So much for the effects of doping. Assuming success in that endeavor, the crystals must then be characterized to determine the degree of dopant incorporation and the extent to which they increase the conductivity of the material. If these steps can be made to work in tandem with an optimized bulk growth process, then a conductive form of γ -LiBO₂ may be economically viable.

Finally, it remains to test them under neutron exposure and prepare their utility for incorporation into a practical device. In the former, simply measuring their current and voltage response while subjected to a neutron flux may be sufficient—but it may also prove necessary to isolate a particular level of doping for peak performance, resulting in a concurrent operation with some of the chemical steps discussed above. Suitable mounts for the crystal must be found so that they can be incorporated into circuitry without need for impractical jigs, clamps, or other apparatus. Deposition of contact patches may be the most viable course of action, and yet a large amount of work in its own right. Once done, however, and assuming success in all other matters, γ -LiBO₂ may yet be a cheap and effective neutron detector.

6. Appendix A

Herein follows some early work on the subject of modeling flows within the autoclave and ampule.

6.1 The Problem

The fundamental objective of this problem is to gain insight into the particular behavior of a fluid within an opaque chamber. Though we are greatly aided in this by knowledge of general chemical principles, it remains, generally, a volume whose behavior we can otherwise only deduce from by the comparison of the final state to the initial and stable conditions that were set up at the beginning of the experiment. That is to say, we are confronted with a high-pressure autoclave which must, in order to contain its charge, remain quite impenetrable, and quite sealed against interference. The cut-away geometry, then, in cartoon, is found in figure one. The large, grey, component is representative of the Inconel autoclave in which the reaction is contained; the thin yellow line indicates the sample ampoule (either silver or platinum) that contains the caustic mineralizer solution, and the thin blue band between the grey and the yellow is the water with which the autoclave chamber is filled to counterbalance the pressure built up within the ampoule. Furthermore, there are though not shown band heaters that wrap around the outside of the autoclave, and which are controlled to provide a fixed temperature at the surface of the autoclave.

Four different regions of computational solving; two sets of fundamental physics to be concerned with. In the Inconel and the precious metal tube, the problem is described in by the heat equation, which takes the form

$$\frac{\partial u}{\partial t} = k \frac{\partial^2 u}{\partial x^2} + Q(x, t) \quad (35)$$

for a non-homogenous problem with steady source and sink terms. Indeed, for convenient boundary conditions and geometry, this is an entirely analytic equation but this problem is not so felicitous [64]. More on that later.

Within the fluid chambers, begin with the Navier-Stokes equation

$$\frac{\partial \vec{v}}{\partial t} + \vec{v} \cdot \nabla \vec{v} = -\nabla p + \nabla \cdot \overleftrightarrow{T} + \vec{f}. \quad (36)$$

The Navier-Stokes equation, being strongly non-linear, is not generally solvable, but can be approached with numerical methods with reasonable success. A further complication arises in the specter of turbulence. This will occur if the Reynolds number, $\frac{vL}{\nu}$, is large, where v is the characteristic velocity of the system, L is the characteristic length of the system, and ν is the kinematic viscosity. In the case of the fluid inside the capsule, $L \approx 0.01$ m and $v \approx 9 \times 10^{-7}$ m²/s, the latter having been taken from pure water. The velocity is as yet unknown; the other terms, evaluated leave $Re = 11236 \frac{\text{s}}{\text{m}} \times v$. To have the viscous terms dominate, then, would require a fluid velocity on the order of 0.09 mm/s, which strains credulity. Granted, the Reynolds number is not dogmatic about the onset of turbulence, but the presence of crystal materials, support structures, and imperfections within the ampoule make it likely that turbulence will arise quickly. Furthermore, no qualitative theory of strong turbulence yet exists. For weak turbulence that is to say, turbulence under conditions where \overleftrightarrow{T} can be approximated as a coupling term between modes of flow there is some hope for analysis and modeling, but largely turbulence remains in the realm of empirical codes and order of magnitude approximations [88].

To fully define the problem, one must have complete and consistent boundary and initial conditions for the simulation. The initial conditions are that all the materials should start at room temperature (298.15 K) and at rest, with the pressure

within the system set to 1 Atm. The materials were set using the COMSOL library provided for the purpose, and which included Inconel and liquid water.

The boundary conditions are more difficult. The regions of the autoclave surface are, fortunately, easy: being in direct contact with the temperature-controlled band heaters, two regions on the surface of the Inconel block can be fixed at whatever temperatures are desired for the course of the simulation. At the bottom, top, and un-heated sides, however, the system becomes slightly more problematic from a modeling, though not mathematical, perspective. Though surrounded by insulation, heat is still lost, and so the assumption of a strongly-insulating boundary is not entirely correct. Nonetheless, with a correct set-up, the effect is largely negligible.

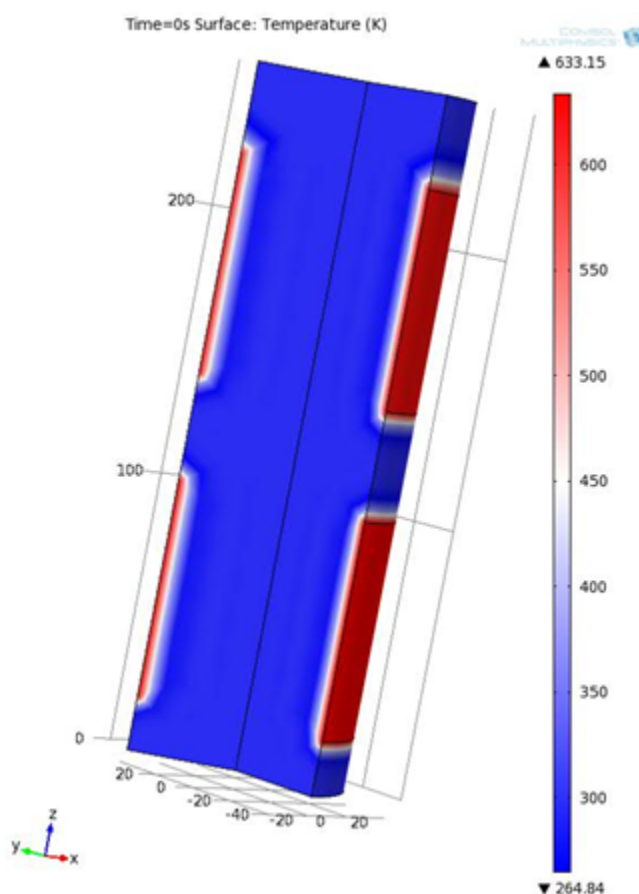


Figure 34. The temperature, in kelvin, of an initial model at $t=0h$.

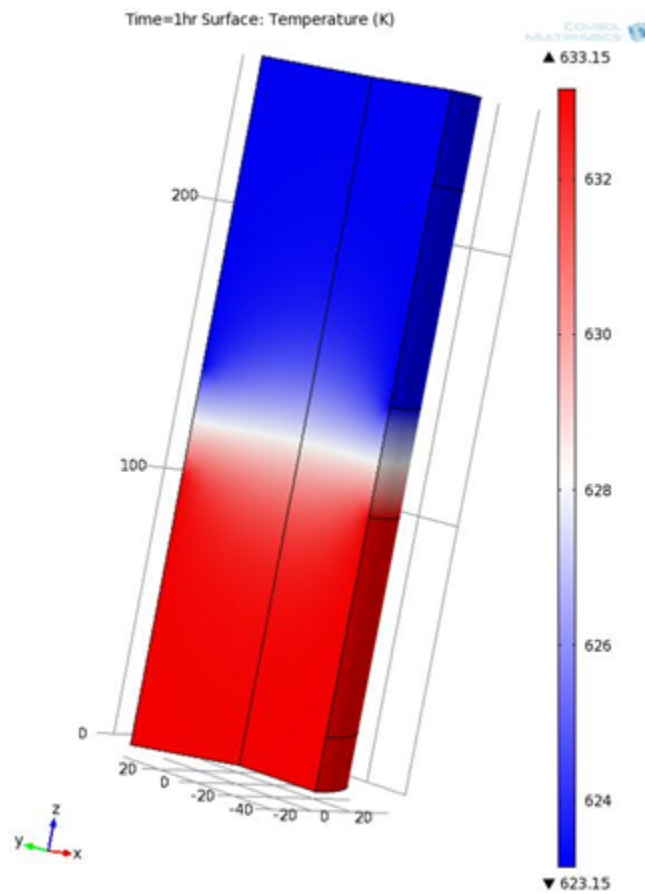


Figure 35. The temperature, in kelvin, of an initial model at $t=1h$.

Finally, there are the boundary conditions between the fluids and the metals that the software must take into account. The heat at the internal surface of the autoclave will warm the fluid, which will convect upward, deposit its heat in the cooler region of the material, flow back down, and continue the process, introducing a time and space dependent boundary within the system, at three interfaces. This represents the crux of the entire problem coupling a second-order time-varying differential equation into a strongly non-linear second-order differential equation. This will require a great deal of finesse within the numerical methods in order to even approach a reasonable solution. In the interim, approximations to a steady-state will likely be very helpful.

6.2 Computational Approximation

Regardless of the details of the final model, it is certain that, at some point, the geometry and time will be broken up into discrete regions that can have at least some average value of the physical quantities were interested in assigned to them. Then the appropriate topic is that of finite difference methods within partial differential equations. (In what follows the author is heavily indebted to [89].)

After establishing a quantization of space and time whatever means, and seeding with initial values, the actual solution becomes a matter of propagating these values forward in accordance with the differential equations governing their behavior. This necessitates quantizing the differential equations. By Taylors theorem, for any sufficiently smooth function, a series exists which approximates a solution about a point x_0 . This series,

$$u(x_0 + \Delta x, t) = u(x_0, t) + \Delta x \frac{\partial u(x_0, t)}{\partial x} + \frac{1}{2!} (\Delta x)^2 \frac{\partial^2 u(x_0, t)}{\partial x^2} + O((\Delta x)^3), \quad (37)$$

indicates the proper way forward for the solution of a differential equation. By rearrangement, one reaches an approximation for any given position based on the points around it:

$$\frac{\partial u(x_0, t)}{\partial x} = \frac{u(x_0 + \Delta x, t) - u(x_0, t)}{\Delta x} + O(\Delta x). \quad (38)$$

This is a forward difference equation; a similar form known as a backward difference equation replaces the Δx with $-\Delta x$, but is otherwise unchanged. It is also important that the space coordinate is not privileged, and the same general form can be applied to generate difference approximations to derivatives for time as well. One further point: though this derivation treats derivatives only in one variable, the formalism is easily extended to partial differential equations, and particularly separable operators, such as the Laplacian in Cartesian or cylindrical coordinates, by simple addition of the individual parts. The grid yielding these, incidentally, forms a simple cross [64].

Regarding the accuracy of these terms, notice that 38 has first-order error in order to get reasonable precision, the steps must be very small with respect to the scale of the problem. This can be improved by taking a two-time-step approximation, effectively assuming that the derivative at a point is approximated by the difference on either side. This is both intuitively pleasing and a significant improvement in accuracy, but can pose a greater difficulty in terms of stability. Both are, however, consistent, which is to say that as the size of the intervals shrinks, the returned values converge to a solution.

The major difficulty with the method of finite differences is that it favors simple geometries with consistent dimensionality. It is easy to conceptualize, of course, but not necessarily practicable when dealing with complicated geometries of physical systems. For these the Finite Element Method is a more suitable approach [64]. In

this case, the region in question is broken up into a suitable number of individual regions—usually triangles—and then attempt to fit a solution using a large number of test functions, e.g. $U(x, t) = \sum c_i T_i(x, t)$. These test functions have no relationship to the PDE, the boundary conditions, or any eigenfunctions an analytic solution might present; the chief virtue of any set of test functions that one might employ is that they should converge rapidly. Naturally, the diversity of these functions leads to a certain amount of judgment following the initial equations; at the least, these should be consistent with what is known as the weak form of the partial differential equation. This can, in turn be re-arranged using the test-function series approximation as an ansatz, generating a second-rank matrix that, upon inversion, gives the coefficients for the series, and thus solves the local problem. And then one repeats until the entire grid has been solved.

All this is well and good, but it is most important to bear in mind both the advantages and pitfalls of any given approach. Computational simulation is no different in this respect. Certainly there are a great many advantages to be gained by simulation; the ease of modifying variables and conducting new test runs is generally to be lauded, and the relatively high return on capital investment are a couple of the advantages to be had in this field. It is precisely for this reason that this section begins with a warning at the outset, due to the success and apparently limitless power of modern computing, it is all the more important to bear in mind the specific capabilities that modeling and simulation can bring to the table, so that one does not fall into the trap of treating the models as flawless reality.

As an illustration of this, Figure 36 presents a very simplified geometry with fixed temperature boundary conditions, created within a physical simulation tool known as COMSOL Multiphysics. It represents the interior volume, reduced to a 2D cross-section to simplify the original model, and rather than having a

time-varying surface temperature, the upper and lower halves, minus a small gap of boundary treated as insulating. The simulation treats this volume as being filled with water, and its only objective is to demonstrate the establishment of convective flow within a very simple system. Now consider Figure 38, the convergence plot produced by the software when asked to calculate this system. Notice that the error achieves a relatively high value early in the process, and remains focused around a single value through the entire run. In fact, the author finds that the computations never actually converge to a solution when this behavior arises.

The point of this digression, then, is simply to demonstrate some of the difficulties of computer modeling as experienced by the practitioner. The causes of such behaviors, and whether or not a given simulation will ultimately work, are at the time of this writing broadly opaque, though this work offers a few general observations:

- Finer meshes, though longer-running, are more likely to converge, but this is by no means guaranteed.
- A set of boundary conditions that collapses at a given time-step for a time-evolved solution will consistently collapse at the same time. This likely indicates some behavior in the model that reaches a critical value and breaks the model; smaller and larger time-steps do not appear to have a mitigating effect on the system.
- Boundary conditions that seem particularly appropriate to the physical system under consideration are often ill-conditioned for the solving system and lead to errors involving inconsistent starting values. One can easily get the impression that the creation of physically relevant, solvable, tractable models is as much an art as it is a science, requiring either a great deal of time or an experienced practitioner.

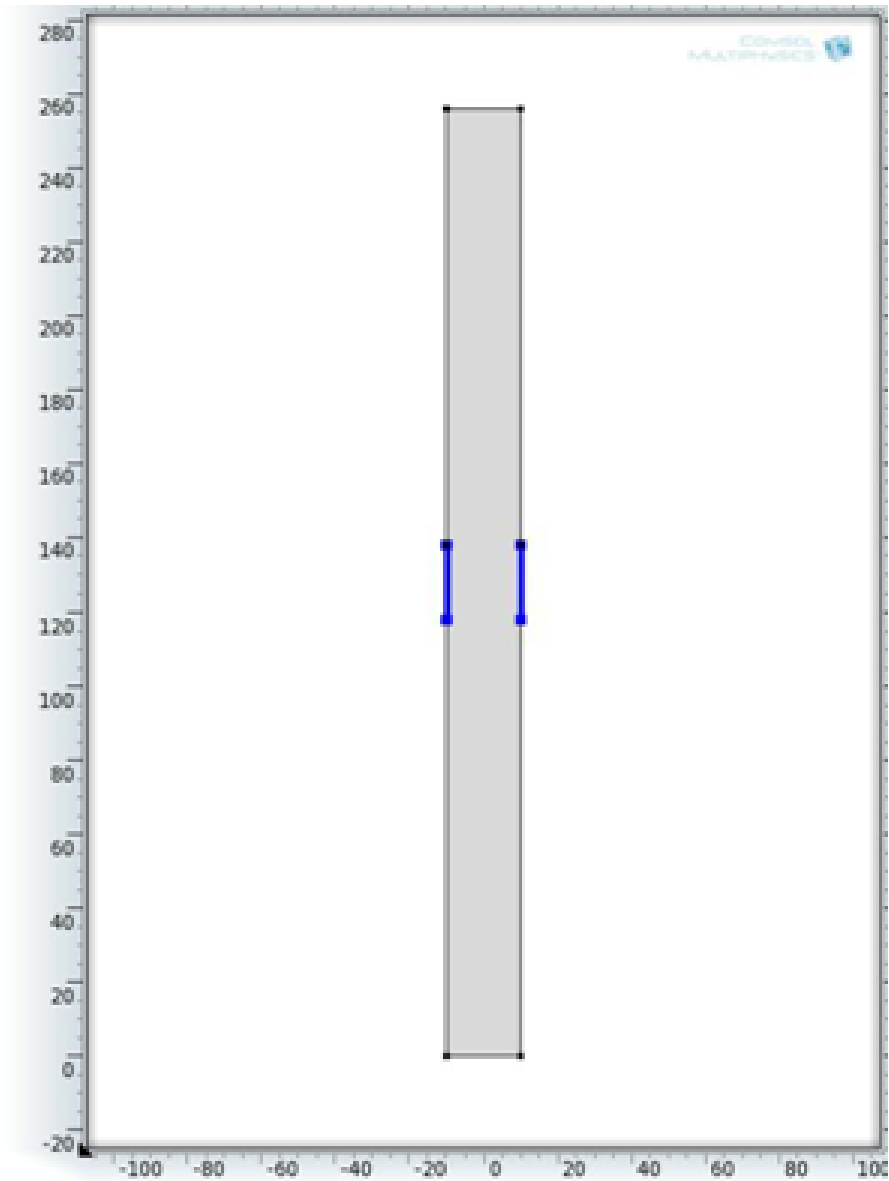


Figure 36. One of the simplest possible models. The upper and lower ends are fixed at cold and hot temperatures, respectively, while the highlighted parts are insulated.



Figure 37. Note that the error associated with solving the model remains high and, indeed, gives no indication that it would converge for any number of iterations.

One can easily get the impression that the creation of physically relevant, solvable, tractable models is as much an art as it is a science, requiring either a great deal of time or an experienced practitioner.

6.3 Initial Technical Approach

For the purposes of this study, the author was fortunate to have access to COMSOL Multiphysics, a comprehensive physical modeling suite designed for precisely this sort of inquiry. It is an extremely versatile set of software, with a commensurate learning curve in order to begin to grasp and modify any pre-existing code—let alone build a new one—with success.

After significant effort, however, the author successfully modified an existing model to produce meaningful, or at least intuitively satisfying results. Again, this is not the best of all possible models, and there are aspects of it that are not well tailored to the actual problem at hand. However, it represents an initial success in the field of modeling.

The geometry in question is 3D with a cylindrical symmetry that effectively reduces the degrees of freedom, and enables the geometry to be specified in a 2D plane with an appropriate axis of rotation specified. (Figure ??; the axis of rotation is indicated by the red dashed line.) The thermal bands are between the points on the right edge; numbering the regions, from the bottom to top, as 1-5, they constitute regions 2 and 4. All sides save for the base are assumed to have convectively cooled boundary conditions—specifically, cooled by air at a temperature of 298.15K. The top of the interior chamber has a slip boundary condition; at this point, we note that this is one of the aforementioned conditions retained from the original working simulation that were not changed in the first go-around. It will be helpful to change this to a no-slip condition for a later run, and to determine if that

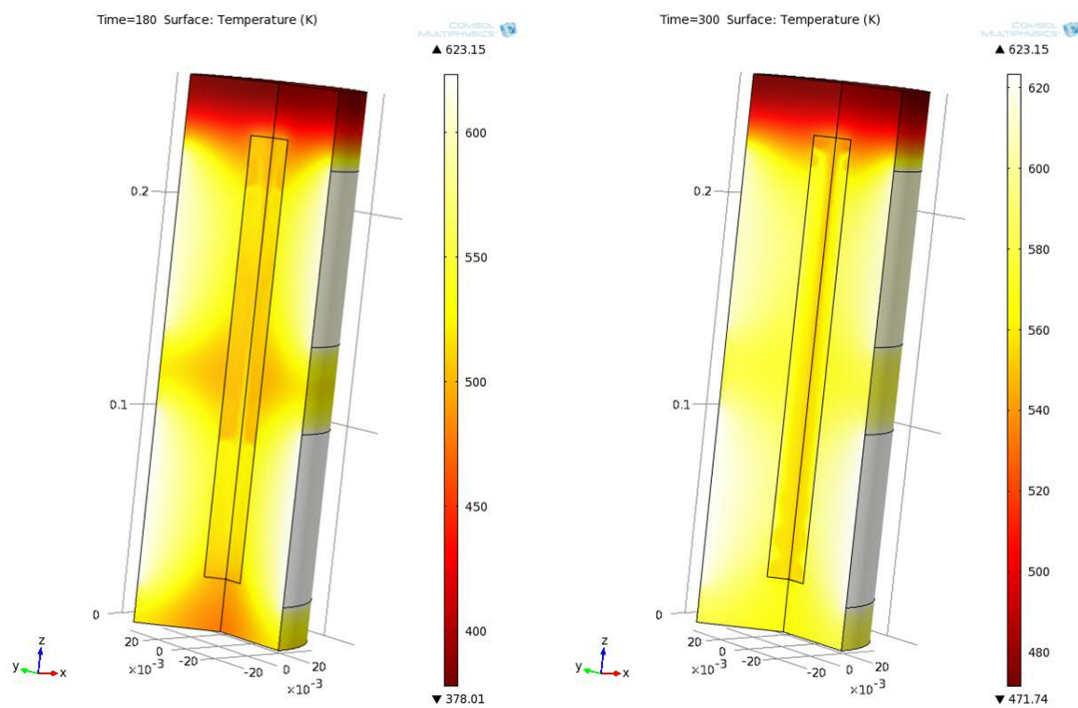
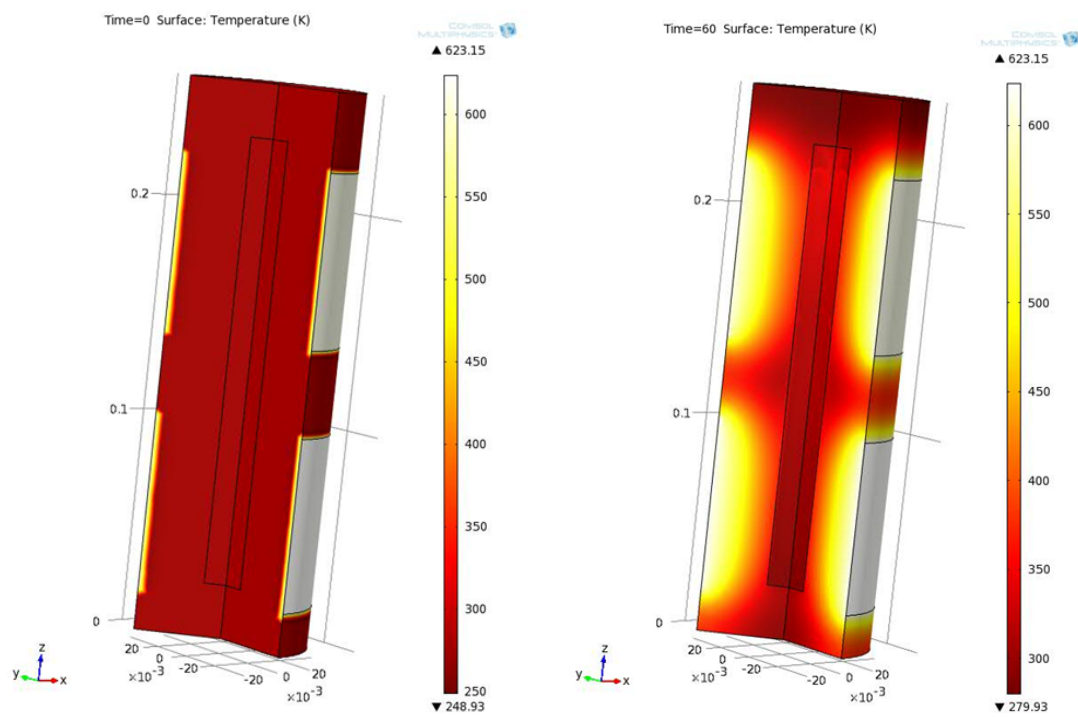
is having a significant effect on the tractability of the model, but again, small perturbations are necessary owing to lack of experience with the system in question. The absolute pressure of the system is defined at 1 Atmosphere, with the initial pressure given by gravity acting on the water in the channel. There is also a pressure fixed point at the upper right corner of the water-volume, restraining that pressure to 1 Atmosphere—again, a significant deviance from the physics of the system, but the goal for the first part of this numerical simulation is simply to achieve a workable flow model.

The results are illustrated in the following series of graphs, with time given in seconds:

From these charts, it is clear that thermal convective flow does start within the tube as a result of the temperature differential within the system, as expected. What is new and interesting is the apparent development of the flow, as particularly illustrated by the streamline and velocity charts. In this case, the simulation illustrates the formation of two separate velocity zones and which form what looks like turbulent interaction though this is not particularly apt, since a retrospective check indicates that the fluid model is based around laminar flow, and does not include a turbulence model. Still, it shows fluid mixing, and then the development of a high-velocity channel in the flow surrounded by a low-velocity return region. Intuitively, this matches what should happen since the side-walls represent a no-slip condition, but have a greater area in which to transmit fluid.

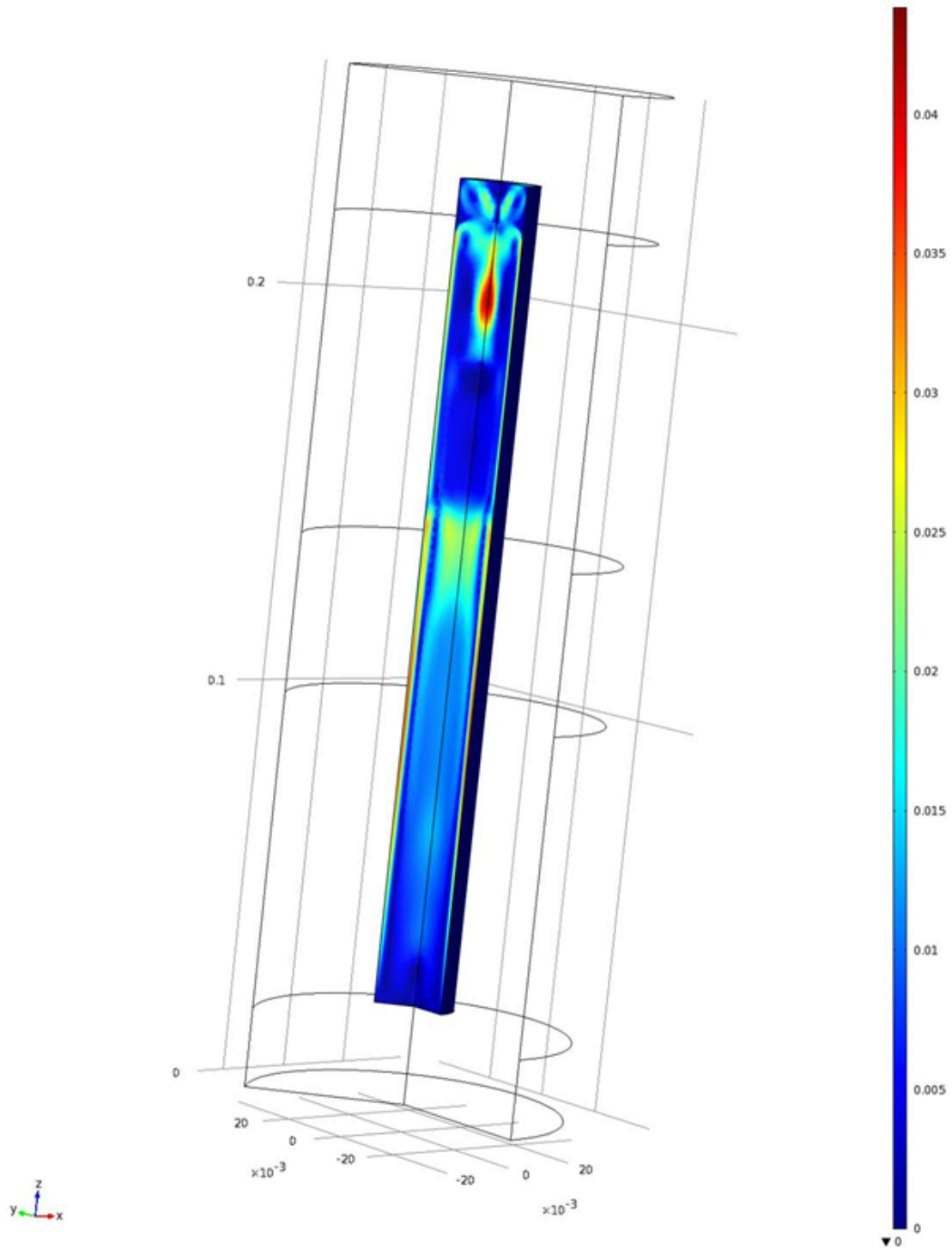
6.4 An Attempt at Refinement

Upon disabling the Pressure Point Constraint (1 Atm) and the no-slip condition at the top of the chamber, COMSOL simply refused to converge. Exploration revealed that the system would be convergent if the pressure constraint were



Time=60 Surface: Velocity magnitude (m/s)

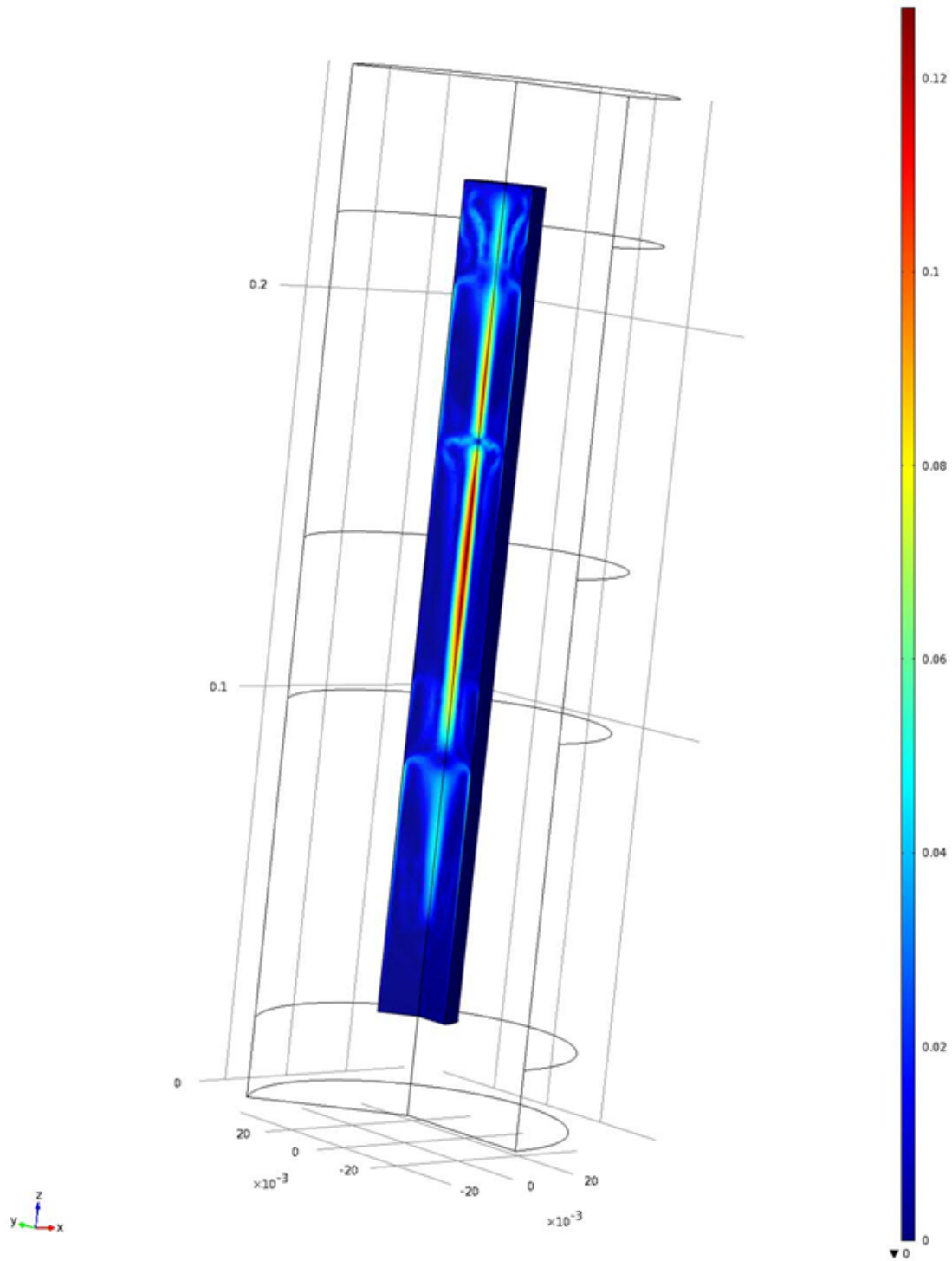
COMSOL MULTIPHYSICS
▲ 0.0438

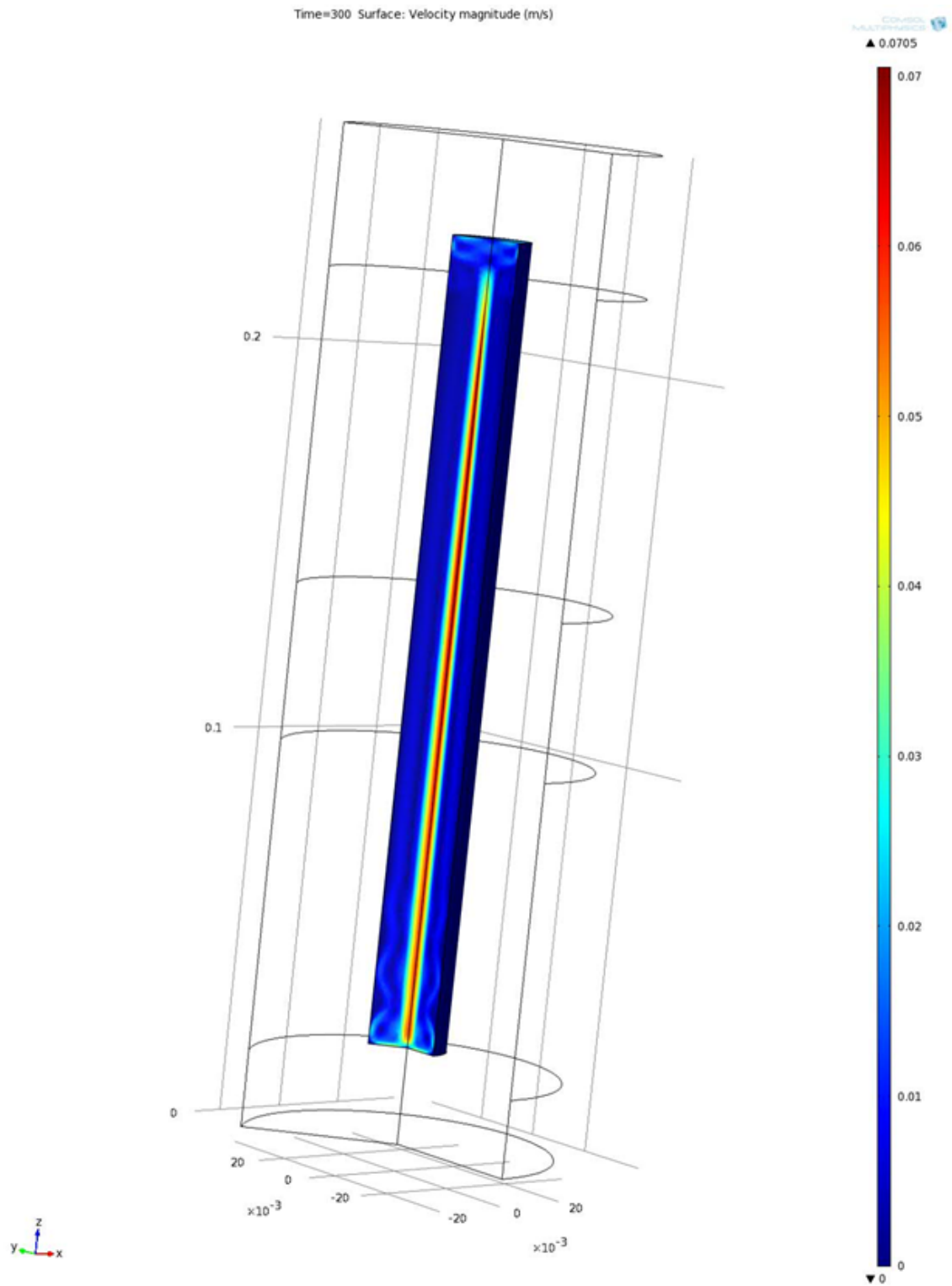


Time=180 Surface: Velocity magnitude (m/s)

COMSOL
MULTIPHYSICS

▲ 0.1272





re-asserted and the no-slip condition retained. Its convergence was not meaningful, however, because the velocity of the fluid in the tube was infinitesimal, more in line with noise in the lowest-order bits of the machine than reasoned calculation.

Despite further efforts, no further progress occurred.

That said, after significant reading and the consultation of the low-order documentation, the author believes that certain assumptions about the built-in capabilities of COMSOL were incorrect. Fundamentally, COMSOL knows about water—which was the working fluid—and it knows that it is indeed a fluid. It may also know some things about steam as well, but this is a retrospective consideration, never explored. Regardless, the fluid inside the autoclave when at temperature and pressure is not liquid water, nor is it actually steam—it is supercritical water, and the equations of state COMSOL has built-in are in no way suited to address its properties, or the phase transitions needed to get there. The author believes that the actual way forward from this point is to implement a specialized water model within the computational framework, but also asserts that it shall remain, for now, a project untried.

Bibliography

- [1] G. Knoll, *Radiation Detection and Measurement*. John Wiley & Sons, 2010.
- [2] “Sigma Evaluated Nuclear Data File (ENDF) Retrieval & Plotting.” [Online]. Available: <http://www.nndc.bnl.gov/sigma/>
- [3] *Airgas Material Safety Data Sheet Boron Trifluoride*, Airgas, 259 North Radnor-Chester Road, Suite 100, Radnor, PA 19087-5283, April 2010.
- [4] *Honeywell Boron Trifluoride Technical Information*, Honeywell Specialty Materials, 101 Columbia Road, Morristown, NJ 07962, April 2006.
- [5] S. Adee, “Physics Projects Deflate for Lack of Helium-3,” 2010. [Online]. Available: <http://spectrum.ieee.org/biomedical/diagnostics/physics-projects-deflate-for-lack-of-helium3>
- [6] A. Kouzes, “The ^3He Supply Problem,” Pacific Northwest National Laboratory, Tech. Rep., 2009. [Online]. Available: http://www.pnl.gov/main/publications/external/technical_reports/PNNL-18388.pdf
- [7] J. C. Petrosky, “Private communication.”
- [8] B. N. L. National Nuclear Data Center, “Chart of Nuclides.” [Online]. Available: <http://www.nndc.bnl.gov/chart/>
- [9] J. H. Hubbell and S. M. Seltzer, “Tables of X-Ray Mass Attenuation Coefficients and Mass Energy-Absorption Coefficients from 1 keV to 20 MeV for Elements Z=1 to 92 and 48 Additional Substances of Dosimetric Interest,” 1996. [Online]. Available: <http://www.nist.gov/pml/data/xraycoef/>
- [10] B. E. Kananen, “Characterization of Neutron-Induced Defects in Isotopically Enriched Lithium Tetraborate,” Master’s thesis, Air Force Institute of Technology, 2011.
- [11] O. Annalakshmi, M. Jose, and G. Amarendra, “Dosimetric characteristics of manganese doped lithium tetraborate — An improved {TL} phosphor,” *Radiation Measurements*, vol. 46, no. 8, pp. 669 – 675, 2011. [Online]. Available: <http://www.sciencedirect.com/science/article/pii/S1350448711002691>
- [12] M. Kayhan and A. Yilmaz, “Effects of synthesis, doping methods and metal content on thermoluminescence glow curves of lithium tetraborate,” *Journal of Alloys and Compounds*, vol. 509, no. 30, pp. 7819 – 7825, 2011. [Online]. Available: <http://www.sciencedirect.com/science/article/pii/S0925838811010188>

- [13] A. T. Brant, D. A. Buchanan, J. W. McClory, P. A. Dowben, V. T. Adamiv, Y. V. Burak, and L. E. Halliburton, “EPR identification of defects responsible for thermoluminescence in Cu-doped lithium tetraborate ($\text{Li}_2\text{B}_4\text{O}_7$) crystals,” *Journal of Luminescence*, vol. 139, pp. 125–131, 2013.
- [14] V. Nagirnyi, E. Aleksanyan, G. Corradi, M. Danilkin, E. Feldbach, M. Kerikmäe, A. Kotlov, A. Lust, K. Polgár, A. Ratas, I. Romet, and V. Seeman, “Recombination luminescence in $\text{Li}_2\text{B}_4\text{O}_7$ doped with manganese and copper,” *Radiation Measurements*, vol. 56, no. 0, pp. 192 – 195, 2013, <http://www.sciencedirect.com/science/article/pii/S1350448713001017>.
- [15] M. Kerikmäe, M. Danilkin, A. Lust, V. Nagirnyi, L. Pung, A. Ratas, I. Romet, and V. Seeman, “Hole traps and thermoluminescence in $\text{Li}_2\text{B}_4\text{O}_7\text{:Be}$,” *Radiation Measurements*, vol. 56, pp. 147–149, 2013.
- [16] V. Holovey, V. Sidey, V. Lyamayev, and P. Puga, “Influence of reducing annealing on the luminescent properties of $\text{Li}_2\text{B}_4\text{O}_7\text{:Cu}$ single crystals,” *Journal of Luminescence*, vol. 126, pp. 408 – 412, 2007.
- [17] Sangeeta, K. Chennakesavulu, D. Desai, S. Sabharwal, M. Alex, and M. Ghodgaonkar, “Neutron flux measurements with a $\text{Li}_2\text{B}_4\text{O}_7$ crystal,” *Nuclear Instruments and Methods in Physics Research Section A: Accelerators, Spectrometers, Detectors and Associated Equipment*, vol. 571, pp. 699 – 703, 2007.
- [18] M. Katagiri, K. Sakasai, M. Matsubayashi, and T. Kojima, “Neutron/ γ -ray discrimination characteristics of novel neutron scintillators,” *Nuclear Instruments and Methods in Physics Research Section A: Accelerators, Spectrometers, Detectors and Associated Equipment*, vol. 529, no. 1-3, pp. 317 – 320, 2004, proceedings of the Joint Meeting of the International Conference on Neutron Optics (NOP2004) and the Third International Workshop on Position-Sensitive Neutron Detectors (PSND2004). [Online]. Available: <http://www.sciencedirect.com/science/article/pii/S0168900204009167>
- [19] J. D. Garrett, M. N. Iyer, and J. E. Greedan, “The Czochralski growth of LiBO_2 and $\text{Li}_2\text{B}_4\text{O}_7$,” *Journal of Crystal Growth*, vol. 41, pp. 225 – 227, 1977.
- [20] T. Lukasiewicz and A. Majchrowski, “Czochralski growth of lithium tetraborate single crystals,” *Materials Letters*, vol. 11, pp. 281 – 283, 1991.
- [21] T. Sugawara, R. Komatsu, and S. Uda, “Growth and characterization of lithium tetraborate crystals grown in phase-matching directions,” *Journal of Crystal Growth*, vol. 193, pp. 364 – 369, 1998.

- [22] N. Tsutsui, Y. Ino, K. Imai, N. Senguttuvan, and M. Ishii, “Growth of large size LBO ($\text{Li}_2\text{B}_4\text{O}_7$) single crystals by modified Bridgman technique,” *Journal of Crystal Growth*, vol. 211, pp. 271 – 275, 2000.
- [23] F. Shi-ji, S. Guan-shun, W. Wen, L. Jin-long, and L. Xiu-hang, “Bridgman growth of $\text{Li}_2\text{B}_4\text{O}_7$ crystals,” *Journal of Crystal Growth*, vol. 99, pp. 811 – 814, 1990.
- [24] P. Becker, “Borate Materials in Nonlinear Optics,” *Advanced Materials*, vol. 10, pp. 979–992, 1998.
- [25] D. Nihtianova, D. Shumov, J. Macicek, and A. Nenov, “Inclusions in LiB_3O_5 crystals, obtained by the top-seeded solution growth method in the $\text{Li}_2\text{O}-\text{B}_2\text{O}_3$ system. Part 2,” *Journal of Crystal Growth*, vol. 169, pp. 527 – 533, 1996.
- [26] N. Senguttuvan, M. Ishii, M. Shimoyama, M. Kobayashi, N. Tsutsui, M. Nikl, M. Dusek, H. M. Shimizu, T. Oku, T. Adachi, K. Sakai, and J. Suzuki, “Crystal growth and luminescence properties of $\text{Li}_2\text{B}_4\text{O}_7$ single crystals doped with Ce, In, Ni, Cu and Ti ions,” *Nuclear Instruments and Methods in Physics Research Section A: Accelerators, Spectrometers, Detectors and Associated Equipment*, vol. 486, pp. 264 – 267, 2002.
- [27] M. W. Swinney, J. W. McClory, J. C. Petrosky, Y. Shan, A. T. Brant, V. T. Adamiv, Y. V. Burak, P. A. Dowben, and L. E. Halliburton, “Identification of electron and hole traps in lithium tetraborate ($\text{Li}_2\text{B}_4\text{O}_7$) crystals: Oxygen vacancies and lithium vacancies,” *Journal of Applied Physics*, vol. 107, p. 113715, 2010.
- [28] T. W. C. Zens, “Personal Communications and Coursework.”
- [29] W. Kingery, H. K. Bowen, and D. R. Uhlmann, *Introduction to ceramics*. Wiley, 1960.
- [30] J. W. Kolis, C. D. McMillen, and T. Franco, “Hydrothermal Synthesis of the Deep-UV NLO Material $\text{Sr}_2\text{Be}_2\text{B}_2\text{O}_7$,” *MRS Proceedings*, vol. 848, p. 3, 2004.
- [31] M. C. Gelabert, R. A. Laudise, and R. E. Riman, “Phase stability, solubility and hydrothermal crystal growth of PbTiO_3 ,” *Journal of Crystal Growth*, vol. 197, pp. 195–203, 1999.
- [32] C. D. McMillen, “Hydrothermal Crystal Growth of Oxides for Optical Applications,” Ph.D. dissertation, Clemson University, 2007.
- [33] A. Einstein, “On the Movement of Small Particles Suspended in Stationary Liquids Required by the Molecular-Kinetic Theory of Heat,” *Annalen der Physik*, vol. 17, pp. 549–560, 1905.

- [34] J. M. Mann, “Personal Communications.”
- [35] K. Byrappa, K. Shekar, and R. Rodriguez-Clemente, “Hydrothermal synthesis and morphology of lithium tetraborate crystals,” *Materials Research Bulletin*, vol. 28, pp. 709 – 718, 1993.
- [36] C. McMillen and J. Kolis, “Bulk single crystal growth from hydrothermal solutions,” *Philosophical Magazine*, vol. 92, pp. 37–41, 2012.
- [37] D. Sands, *Introduction to Crystallography*, ser. Dover Books on Chemistry Series. Dover, 1993. [Online]. Available: http://books.google.com/books?id=h_A5u5sczJoC
- [38] M. J. Buerger, *Elementary Crystallography*. New York: John Wiley & Sons, Inc., 1963.
- [39] J. Nye, *Physical Properties of Crystals: Their Representation by Tensors and Matrices*, ser. Oxford science publications. Clarendon Press, 1985. [Online]. Available: <http://books.google.com/books?id=ugwql-uVB44C>
- [40] Y. Leng, *Materials Characterization: Introduction to Microscopic and Spectroscopic Methods*. Wiley, 2009. [Online]. Available: <http://books.google.com/books?id=Oku4IBjiUKAC>
- [41] M. Ladd and R. Palmer, *Structure Determination by X-Ray Crystallography*. Kluwer Academic/Plenum Publishers, 2003. [Online]. Available: <http://books.google.com/books?id=1SiAFokRCuMC>
- [42] W. F. Smith, *Principles of Materials Science & Engineering, 2 ed.* McGraw-Hill, 1990.
- [43] G. Grosso and G. Parravicini, *Solid State Physics*. Elsevier Science, 2000. [Online]. Available: <http://books.google.com/books?id=L5RrQbbvWn8C>
- [44] R. Liboff, *Introductory Quantum Mechanics*. ADDISON WESLEY Publishing Company Incorporated, 2003. [Online]. Available: <http://books.google.com/books?id=oqZSQgAACAAJ>
- [45] L. Burggraf, “Material Science 620.”
- [46] C. Kittel and H. Kroemer, *Thermal Physics*. W. H. Freeman, 1980. [Online]. Available: <http://books.google.com/books?id=c0R79nyOoNMC>
- [47] S. Sze, *Modern semiconductor device physics*, ser. AWiley-Interscience publication. Wiley, 1998. [Online]. Available: <http://books.google.com/books?id=urfvAAAAMAAJ>

- [48] D. J. Wooten, “Electronic Structure of Lithium Tetraborate,” Ph.D. dissertation, Air Force Institute of Technology, 2010.
- [49] V. T. Adamiv, V. P. Savchyn, P. V. Savchyn, I. M. Teslyuk, and Y. V. Burak, “Influence of isovalent doping on the cathodoluminescence of $\text{Li}_2\text{B}_4\text{O}_7\cdot\text{A}$ ($\text{A}=\text{K}$, Cu , Ag) single crystals,” *Functional Materials*, vol. 16, pp. 247–251, 2009.
- [50] J. Xiao, N. Lozova, Y. Losovyj, D. Wooten, I. Ketsman, M. Swinney, J. Petrosky, J. McClory, Y. Burak, V. Adamiv, A. Brant, and P. Dowben, “Surface charging at the (100) surface of Cu doped and undoped $\text{Li}_2\text{B}_4\text{O}_7$,” *Applied Surface Science*, vol. 257, pp. 3399 – 3403, 2011.
- [51] E. Pekpak, A. Ylmaz, and G. zbayolu, “The effect of synthesis and doping procedures on thermoluminescent response of lithium tetraborate,” *Journal of Alloys and Compounds*, vol. 509, no. 5, pp. 2466 – 2472, 2011. [Online]. Available: <http://www.sciencedirect.com/science/article/pii/S0925838810028136>
- [52] I. Ketsman, D. Wooten, J. Xiao, Y. Losovyj, Y. Burak, V. Adamiv, A. Sokolov, J. Petrosky, J. McClory, and P. Dowben, “The off-axis pyroelectric effect observed for lithium tetraborate,” *Physics Letters A*, vol. 374, pp. 891 – 895, 2010.
- [53] G. Corradi, V. Nagirnyi, A. Kotlov, A. Watterich, M. Kirm, K. Polgr, A. Hofstaetter, and M. Meyer, “Investigation of Cu-doped $\text{Li}_2\text{B}_4\text{O}_7$ single crystals by electron paramagnetic resonance and time-resolved optical spectroscopy,” *Journal of Physics: Condensed Matter*, vol. 20, no. 2, p. 025216, 2008. [Online]. Available: <http://stacks.iop.org/0953-8984/20/i=2/a=025216>
- [54] C. L. Christ and J. R. Clark, “A Crystal-Chemical Classification of Borate Structures with Emphasis on Hydrated Borates,” *Physical Chemistry Minerals*, vol. 2, pp. 59–87, 1977.
- [55] F. Mandl, *Statistical Physics*, ser. Manchester Physics Series. Wiley, 1988.
- [56] A. Pabst, “The Metamict State,” *American Mineralogist*, vol. 37, pp. 137–157, 1952.
- [57] S. G. Popov, V. K. Ivanov, J. J. Carbajo, and G. L. Yoder, “Thermophysical Properties of MOX and UO_2 Including the Effects of Irradiation,” Oak Ridge National Laboratory, Tech. Rep., 2000.
- [58] J. M. Mann, “Hydrothermal Crystal Growth of Tetravalent and Pentavalent Metal Oxides,” Ph.D. dissertation, Clemson University, 2009.
- [59] A. Ballman and R. A. Laudise, “Hydrothermal Growth,” in *The Art and Science of Growing Crystals*, J. J. Gilman, Ed. New York, New York: Wiley, 1963, pp. 398–407.

- [60] K. Byrappa and M. Yoshimura, *Handbook of Hydrothermal Technology: A Technology for Crystal Growth and Materials Processing*. Norwich, NY: Noyes Publications William Andrew Publishing, LLC, 2001.
- [61] R. A. Laudise, *The Growth of Single Crystals*. Englewood Cliffs, N.J: Prentice Hall, 1970.
- [62] V. Esin, A. Krivonosova, and T. Fedorova, "Effect of growth rate on the dislocations structure of aluminium single crystals of various orientations," *Journal of Crystal Growth*, vol. 52, Part 1, no. 0, pp. 385 – 390, 1981. [Online]. Available: <http://www.sciencedirect.com/science/article/pii/0022024881902232>
- [63] M. Kuriyama, W. J. Boettinger, and H. E. Burdette, "Crystal perfection in Czochralski grown nickel single crystals," *Journal of Crystal Growth*, vol. 43, no. 3, pp. 287 – 300, 1978. [Online]. Available: <http://www.sciencedirect.com/science/article/pii/0022024878903858>
- [64] R. Haberman, *Applied Partial Differential Equations: With Fourier Series and Boundary Value Problems*. Pearson Prentice Hall, Pearson Education, Incorporated, 2004. [Online]. Available: <http://books.google.com/books?id=alp0QgAACAAJ>
- [65] D. W. Oxtoby, H. P. Gillis, and N. H. Nachtrieb, *Principles of Modern Chemistry*, 5th ed. Thomson Learning, Inc, 2002.
- [66] R. Weast, Ed., *CRC Handbook of Chemistry and Physics: A Ready-reference Book of Chemical and Physical Data*, 67th ed. CRC Press, 1987.
- [67] C. J. Bridgman, *Introduction to the Physics of Nuclear Weapons Effects*. Fort Belvoir, VA: Defense Threat Reduction Agency, 2001, vol. 8725.
- [68] K. S. Krane, *Introductory Nuclear Physics*. Wiley, 1987.
- [69] Y. Burak, B. Padlyak, and V. Shevel, "Radiation-induced centers in the Li₂B₄O₇ single crystals," *Nuclear Instruments and Methods in Physics Research Section B: Beam Interactions with Materials and Atoms*, vol. 191, no. 1-4, pp. 633 – 637, 2002. [Online]. Available: <http://www.sciencedirect.com/science/article/pii/S0168583X02006249>
- [70] J. Petrosky, "Radiation Effects in Materials."
- [71] B. Douglas, D. McDaniel, and J. Alexander, *Concepts and Models of Inorganic Chemistry, Solutions Manual*. Wiley, 1994. [Online]. Available: <http://books.google.com/books?id=g092QgAACAAJ>
- [72] D. Rutledge, A. Scherer, and G. DeRose, *A^{Ph} 9 Laboratory Manual: Introduction to Integrated Circuits*. Pasadena, CA: California Institute of Technology, 2003.

- [73] P. Horowitz and W. Hill, *The Art of Electronics*. Cambridge University Press, 2006. [Online]. Available: <http://books.google.com/books?id=6kfGkQEACAAJ>
- [74] Y. Burak, V. Adamiv, I. Teslyuk, and V. Shevel, “Optical absorption of isotopically enriched $\text{Li}_2\text{B}_4\text{O}_7$ single crystals irradiated by thermal neutrons,” *Radiation Measurements*, vol. 38, no. 46, pp. 681 – 684, 2004, <http://www.sciencedirect.com/science/article/pii/S1350448703003664>. [Online]. Available: <http://www.sciencedirect.com/science/article/pii/S1350448703003664>
- [75] V. Adamiv, Y. Burak, D. J. Wooten, J. McClory, J. Petrosky, I. Ketsman, J. Xiao, Y. B. Losovyj, and P. A. Dowben, “The Electronic Structure and Secondary Pyroelectric Properties of Lithium Tetraborate,” *Materials*, vol. 3, no. 9, pp. 4550–4579, 2010. [Online]. Available: <http://www.mdpi.com/1996-1944/3/9/4550>
- [76] D. Robertson and I. Young, “The growth and growth mechanism of lithium tetraborate,” *Journal of Materials Science*, vol. 17, pp. 1729–1738, 1982.
- [77] K. Byrappa, V. Rajeev, V. Hanumesh, A. Kulkarni, and A. Kulikarni, “Crystal growth and electrical properties of $\text{Li}_2\text{B}_4\text{O}_7$,” *Journal of Materials Research*, vol. 11, pp. 2519–2525, 1996.
- [78] C. D. McMillen, H. G. Giesber, and J. W. Kolis, “The hydrothermal synthesis, growth, and optical properties of $\gamma\text{-LiBO}_2$,” *Journal of Crystal Growth*, vol. 310, pp. 299 – 305, 2008.
- [79] P. Li and Z.-H. Liu, “Hydrothermal Synthesis, Characterization, and Thermodynamic Properties of a New Lithium Borate, $\text{Li}_3\text{B}_5\text{O}_8(\text{OH})_2$,” *Journal of Chemical & Engineering Data*, vol. 55, pp. 2682–2686, 2010.
- [80] W. Zhu, L. Zhang, X. Cui, and Q. Zhang, “Efficient synthesis of orthorhombic lithium borate hydroxide micro-rods and their thermal conversion to lithium borate,” *Powder Technology*, vol. 210, no. 1, pp. 67 – 72, 2011. [Online]. Available: <http://www.sciencedirect.com/science/article/pii/S0032591011000891>
- [81] P. W. Bridgman, “The Technique of High Pressure Experimenting,” *Proceedings of the American Academy of Arts and Sciences*, vol. XLIX, no. 1, pp. 625 – 646, 1914.
- [82] A. Engineers, “AE Closure Pressure Vessels,” Parker Autoclave Engineers, Tech. Rep., 2012. [Online]. Available: http://www.autoclaveengineers.com/ae_pdfs/PV_Closure.pdf

- [83] Y. Wang, S. Pan, X. Tian, Z. Zhou, G. Liu, J. Wang, and D. Jia, “Synthesis, Structure, and Properties of the Noncentrosymmetric Hydrated Borate $\text{Na}_2\text{B}_5\text{O}_8(\text{OH})_2\text{H}_2\text{O}$,” *Inorganic Chemistry*, vol. 48, pp. 7800–7804, 2009.
- [84] C. Giacobazzo, S. Menchetti, and F. Scordari, “The Structure of Tincalconite,” *American Mineralogist*, vol. 58, pp. 523–530, 1973.
- [85] M. Veléz, H. Tuller, and D. Uhlmann, “Chemical durability of lithium borate glasses,” *Journal of Non-Crystalline Solids*, vol. 49, no. 13, pp. 351 – 362, 1982, proceedings of the Sixth University Conference on Glass Science. [Online]. Available: <http://www.sciencedirect.com/science/article/pii/0022309382901314>
- [86] R. Weston and H. Schwarz, *Chemical kinetics*, ser. Fundamental topics in physical chemistry. Prentice-Hall, 1972. [Online]. Available: <http://books.google.com/books?id=6T1RAAAAMAAJ>
- [87] D. Schultz, B. Blasy, J. C. Santana, C. Young, J. C. Petrosky, J. W. McClory, D. LaGrafte, J. I. Brand, J. Tang, W. Wang, N. Schemm, S. Balkir, M. Bauer, I. Ketsman, R. W. Fairchild, Y. B. Losovyj, and P. A. Dowben, “The K-shell Auger electron spectrum of gadolinium obtained using neutron capture in a solid state device,” *Journal of Physics D: Applied Physics*, vol. 43, p. 075502, 2010.
- [88] K. Thorne and R. Blandford, *Modern Classical Physics: Optics, Fluids, Plasmas, Elasticity, Relativity, and Statistical Physics*. Princeton University Press, 2014. [Online]. Available: <http://books.google.com/books?id=bEVHmwEACAAJ>
- [89] N. Gershenfeld, *The Nature of Mathematical Modeling*. Cambridge University Press, 1999. [Online]. Available: <http://books.google.com/books?id=lSTOh8U7NkkC>

REPORT DOCUMENTATION PAGE					Form Approved OMB No. 0704-0188	
<p>The public reporting burden for this collection of information is estimated to average 1 hour per response, including the time for reviewing instructions, searching existing data sources, gathering and maintaining the data needed, and completing and reviewing the collection of information. Send comments regarding this burden estimate or any other aspect of this collection of information, including suggestions for reducing the burden, to Department of Defense, Washington Headquarters Services, Directorate for Information Operations and Reports (0704-0188), 1215 Jefferson Davis Highway, Suite 1204, Arlington, VA 22202-4302. Respondents should be aware that notwithstanding any other provision of law, no person shall be subject to any penalty for failing to comply with a collection of information if it does not display a currently valid OMB control number.</p> <p>PLEASE DO NOT RETURN YOUR FORM TO THE ABOVE ADDRESS.</p>						
1. REPORT DATE (DD-MM-YYYY) 27-03-2014		2. REPORT TYPE Master's Thesis		3. DATES COVERED (From - To) Aug 2012 - Mar 2014		
4. TITLE AND SUBTITLE Hydrothermal Crystal Growth of Lithium Tetraborate and Lithium γ -Metaborate				5a. CONTRACT NUMBER		
				5b. GRANT NUMBER		
				5c. PROGRAM ELEMENT NUMBER		
6. AUTHOR(S) Graham, Jeffrey, J, Capt				5d. PROJECT NUMBER		
				5e. TASK NUMBER		
				5f. WORK UNIT NUMBER		
7. PERFORMING ORGANIZATION NAME(S) AND ADDRESS(ES) Air Force Institute of Technology Graduate School of Engineering and Management (AFIT/EN) 2950 Hobson Way Wright-Patterson AFB OH 45433-7765				8. PERFORMING ORGANIZATION REPORT NUMBER AFIT-ENP-14-M-12		
9. SPONSORING/MONITORING AGENCY NAME(S) AND ADDRESS(ES) Air Force Research Laboratory Sensors Directorate Dr. J. Matthew Mann 2241 Avionic Circle Wright-Patterson AFB, OH 45433 james.mann.11@us.af.mil				10. SPONSOR/MONITOR'S ACRONYM(S) AFRL/Ry		
				11. SPONSOR/MONITOR'S REPORT NUMBER(S)		
12. DISTRIBUTION/AVAILABILITY STATEMENT Distribution Statement A. Approved for Public Release; Distribution Unlimited.						
13. SUPPLEMENTARY NOTES This material is declared a work of the U.S. Government and is not subject to copyright protection in the United States.						
14. ABSTRACT Growth of lithium tetraborate by the hydrothermal method was attempted in 10^{-6} M LiOH, both by spontaneous nucleation and transport growth. Tetraborate grew out of the first spontaneous nucleation reaction, while the seed dissolved and lithium γ -metaborate formed during the transport growth reactions. A species thermodynamic stability study showed γ -metaborate formed exclusively from 350°C to 550°C, and $\text{Li}_3\text{B}_5\text{O}_8(\text{OH})_2$ was observed at 250°C; tetraborate was not observed. A solubility study on lithium tetraborate did not achieve equilibrium conditions, but did demonstrate that γ -metaborate is significantly more thermodynamically stable than tetraborate under the tested conditions. Formation of lithium tetraborate hydrothermally was shown to result from kinetic growth.						
15. SUBJECT TERMS Hydrothermal growth; lithium tetraborate; lithium metaborate; metastable phase						
16. SECURITY CLASSIFICATION OF:			17. LIMITATION OF ABSTRACT	18. NUMBER OF PAGES	19a. NAME OF RESPONSIBLE PERSON	
a. REPORT	b. ABSTRACT	c. THIS PAGE			Dr. Timothy W. C. Zens, AFIT/ENP	
U	U	U	UU	122	19b. TELEPHONE NUMBER (Include area code) (937) 255-3636 x 4695 timothy.zens@afit.edu	